Noise in Marine Seismic Data

Thomas Elboth

May 11, 2010

Thesis submitted for the partial fulfillment for the degree of PhD

Series of dissertations submitted to the
Faculty of Mathematics and Natural Sciences, University of Oslo
No. 968

ISSN 1501-7710

Cover: Inger Sandved Anfinsen.
Printed in Norway: AiT e-dit AS.

Produced in co-operation with Unipub.
The thesis is produced by Unipub merely in connection with the
thesis defence. Kindly direct all inquiries regarding the thesis to the copyright
holder or the unit which grants the doctorate.

Acknowledgments

The work presented in this thesis has been carried out under the supervision of Prof. Øyvind Andreassen and Prof. Bjørn Anders Reif Pettersson at FFI (Norwegian Defense Research Establishment), and Prof. John Grue at Mechanics Division, Department of Mathematics, University of Oslo, Norway.
In addition to my supervisors, a large number of people deserve to be acknowledged for the help, support and aide they have provided. Hoping to remember all colleagues in Fugro Geoteam and Fugro Seismic Imaging, I list; Peder Berentzen, John Ege, Jakub Warszawski, Terje Stensbø, Nils Åtland, Roar Valentinsen, Camilla Brock Pedersen, Ottar Sandvin, Arve Gudmundset, Emma Scala, Dr. Xiao-Ping Li, Andre Janke, Declan Prichard, Prof. Alfred Hanssen, Wei-Yeong Yang, Dr. Thomas Hertweck Charlotte Sanchis, Tim Miles and Richard Dyer. Among the vessel crews I want to thank, Hans Jørgen Åkre, Daniel Walker, Bob Sheridan and Andrey Ushakov for their help in providing data, and carrying out tests and measurements. I thank the marketing department in Fugro Geoteam for providing some of the pictures and illustrations used in this work. Colleagues at FFI have also made valuable contributions. Prof. Murat Tutkun, Emma Wingstedt, Dr. Bernt Johnsen, Thomas Frømyr and Dr. Tor Knudsen need to be mentioned in this context. I am also grateful to M. B. Martell and Prof. J. B. Perot at Univ. of Massachusetts, Amherst for providing one of the DNS channel flow simulation that has been used in this work. I want to thank the co-authors of the articles that make up this thesis. Finally, thanks to friends and family, who never stopped asking when I would finish my work - and hopefully rejoin the world outside.
The sponsors of this work has been The Norwegian Research Council through grant PETROMAKS 175921/S30, FFI and Fugro.

Abstract

Marine seismic is a well established method to search for subsurface hydrocarbon deposits. However, the method is often limited by various sources of noise, of which flow and swell noise are the dominating types. This study takes advantage of 3-D direct numerical simulations of fluid flow combined with real life, and full scale measurements of flow and swell noise acquired on purpose built seismic streamer cables in the ocean, to study the mechanisms responsible for flow noise generation. The combined knowledge obtained by the simulations and the measurements are then put to use in order to come up with practical methods to reduce noise in seismic data. Two different paths are followed:

The first is in the form of a software de-noising algorithm developed and implemented as a module in a commercial seismic processing software package. It works in the frequency domain by statistically comparing neighboring traces, and attenuates amplitudes that are found to be abnormal. The module is in daily use, and has successfully been applied to attenuate various types of noise found in both land, and marine seismic data.

The second path followed to reduce the amount of noise in seismic data is to use so-called superhydrophobic surfaces. This is in the form of a coating material that can be applied to seismic streamers to reduce both drag and flow noise. The flow noise reduction capabilities of superhydrophobic surfaces is a new discovery, which holds great promise.

Keywords:

Marine seismic acquisition, seismic processing, seismic streamer, flow noise, swell noise, hydrodynamic noise, seismic interference, noise attenuation, turbulent boundary layer, acoustics, direct numerical simulations, superhydrophobic surfaces, drag reduction.

Contents

Chapter 1

Introduction

1.1 Outline of this thesis

This thesis deals with fluid mechanics, signal processing and geophysics in order to reduce the noise-level in subsurface reflection data acquired by seismic vessels searching for hydrocarbon deposits. It contains two introductory chapters, a collection of scientific articles and a short summary. In total, this provides a fairly broad coverage of noise generation, noise avoidance and noise attenuation in marine seismic data.

This first chapter introduces marine seismic acquisition and processing. The goal is not to cover all aspects of this field, but rather to provide enough information that someone not familiar with this topic should understand the basic concepts. Chapter 2 provides more background information to the specific work in this thesis, and contains several examples of seismic noise removal where a program written as part of this thesis work is used. Chapter 3 and 4 are the two journal articles Elboth et al. (2009b) and Elboth et al. (2010a). They present results from both theoretical studies and full scale measurements of the flow that surrounds seismic streamer cables in an ocean environment. Together with chapter 5 (Elboth et al., 2009c) which is based upon a computer simulation of flow noise, they provide physical explanations of how flow and swell noise are created, and give examples of how such noise appear in a seismic recording.

The topic covered in chapters 6, 7 and 8 is how to remove seismic noise trough signal processing. These chapters are based upon the journal article (Elboth et al., 2010b), and two conference abstracts (Elboth et al., 2008) and (Elboth and Herrmansen, 2009). The presented results were obtained by using a software de-noising algorithm that was written as part of this thesis work.

The last journal article (Elboth et al., 2010c) is found in chapter 9. There we show, through both simulations and measurements, that it is possible to reduce the amount of drag and noise generated on towed seismic cables through the use of a superhydrophobic coating material. This represents a new observation, which has a great industrial potential.

The last chapter sums up the main results. It also looks at the economic implications of noise reduction and points towards some ongoing and future research that have been initiated based upon the work presented here.

1.2 Background and motivation

Marine seismic is an industry that consists of four large, and a number of smaller contractors. World wide, these companies operate around 100 seismic vessels and a similar number of processing centers. The annual turnover (2009) of the marine seismic industry is several billion US$.

In 2005 I was employed as a R&D geophysicist/programmer in the geoscience company Fugro Geoteam AS. My main task was to develop software to aide the processing staff in removing noise from marine seismic data. This is important in order to obtain accurate images of the subsurface. However, after about 8 months, it became apparent that a number of issues related to noise removal were really challenging, and that our lack of knowledge limited further process. At the same time my Msc supervisor, Øyvind Andreassen, suggested that we could seek founding from the Research Council of Norway to set up a project to investigate problems related to flow noise. Professor Andreassen work at the Norwegian Defense Research Establishment. They had previously briefly investigated towed sensor arrays for the Norwegian Navy, and found that such arrays were troubled by flow noise. Now, we saw an opportunity to both serve the seismic industry, and the Navy by working on these problems, and come up with practical solutions. To make a long story short, we applied for founding from the Research Council. The application was successful, and starting in September 06, I became one of three PhD candidates involved in research on noise in seismic data.

Naturally, the work was divided among the candidates, and their supervisors. The first one was to look at signal processing to remove noise. The second candidate was to study theoretical aspects of turbulent flow, and try to understand how this worked to create flow noise. My work description was more loosely formulated. The aim was to perform both computer simulations and practical measurements in order to better understand how flow and swell noise was generated and recorded in seismic data. Based upon any findings, I was to look at possible hardware and software modifications to reduce the noise level. This loose formulation turned out to be a good idea. It enabled me to opportunistically follow a number of leads and ideas that appeared during our work.

To have a research program tightly connected to industry had some benefits. Every time we came up with new software ideas these could quickly be placed into production for testing, and commercial usage. The software algorithms presented in this thesis are therefore not only academic. They are proven concepts, used daily in a commercial setting. The same thing is also partly true for some of hardware modifications that we have suggested. Practical reasons make it more time-consuming to change existing hardware. However, during the summer 2010, the first commercial test of a seismic streamer designed based upon ideas from chapter 4 is planned. By 2010 or 2011 we also hope to have superhydrophobic drag reducing and anti-fouling coating, presented in chapter 9, ready for commercial usage.

There is also an economical side to working in an industrial R&D project. The costs connected with one of the hardware experiments reported in this thesis is around $1\,\mathrm{Mill}\,US\$$. Computing time, for software de-noising - and simulations exceed $100\mathrm{K}\,US\$$. This is probably significantly more money than an average PhD project. The positive side to this is that few compromises were done during testing. It was often done 'full scale', with long streamer cables and Giga or Tera-bytes of data.

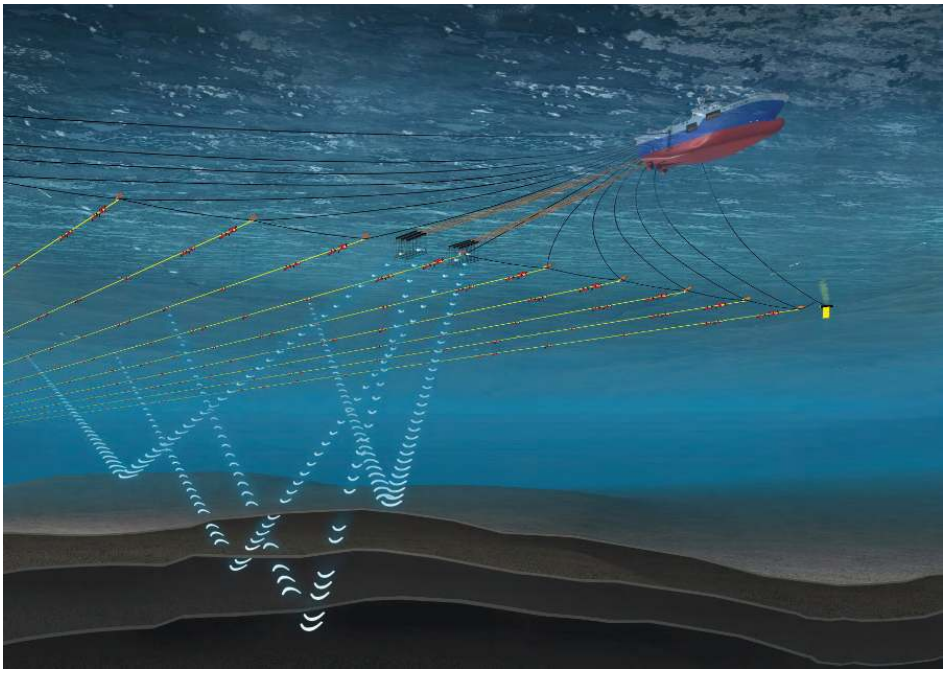

Figure 1.1: Artist's impression of a modern seismic survey, drawn almost in the correct scale.

1.3 Marine seismic surveying

The content presented in the rest of this chapter would be well known to a geophysicist. However, for anyone not working within the geo-sciences, these next sections provide background material to understand the papers presented later in this thesis.

The main objective of marine seismic surveying is to search for subsurface hydrocarbons. This is normally done by employing a cable towing configuration, whereby a surface vessel tows an acoustic source (air gun array) and long streamer arrays through the water a few meters below the surface. With a certain time interval, an acoustic source emits a pulse which propagate into the subsurface. Here, the acoustic energy is partially reflected at the interfaces between different rock types. Parts of this reflected energy is received by sensors inside the streamer cables. These signals provide the arrival time, amplitude and character of the reflections. By post-processing this data, images of the subsurface can be produced. It is based upon such images that decisions about the development of an oilfield are taken.
Figure 1.1 is an artistic image illustrating the scale and some of the equipment involved in modern marine seismic acquisition. The towing vessel, moving at 4 to $5\,\mathrm{kn}$, is typically around $100\,\mathrm{m}$ long and between 25 and $30\,\mathrm{m}$ wide. A few hundred meters behind the vessel, the source-array, see Figure 1.2(a), is towed. This is made up of a number of air-guns. Even further back is the streamer array where the hydrophone sensors are placed. This consists normally up to

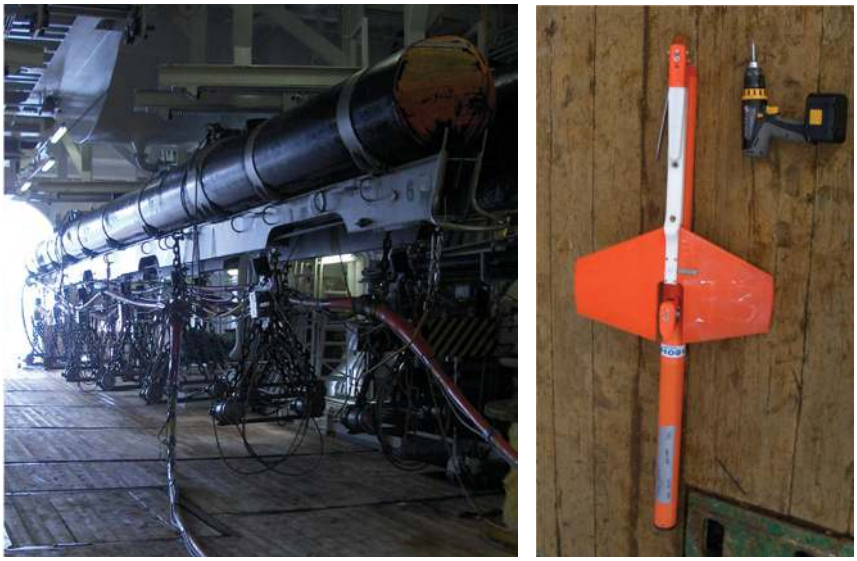

(a) (b)

Figure 1.2: Image a): A gun array inside the vessel before being deployed. Image b): A steering bird placed on the deck of a vessel.

20 parallel cables with 50-150 m separation. Each cable can be up to 10 km long. The head of each streamer cable is attached to a tow cable, called lead-in, which connect the streamer to the tow vessel. Steering devices, called birds, see Figure 1.2(b), are spread out along the streamer cables to ensure that they maintain a correct depth and heading. This is also supported by a network of acoustic pods which provide positioning information. At the tail of each cable there is tail-buoy that also serves as a positioning reference. The doors, seen in Figure 1.3 provide a side-way lift to maintain streamer cable separation.

In total, marine seismic acquisition requires large amounts of highly specialized equipment. Once the acquisition in an area starts, it can continue for months in nearly all kinds of weather. Seismic operations are also costly, with day rates up to several hundred thousand US$.

1.4 Types of marine surveying

Two types of seismic surveys are available to the geophysicist: Two-dimensional (2-D) surveys, and three-dimensional (3-D) surveys. 2-D seismic data are normally acquired by towing one streamer cable behind a vessel. The processed data from this single streamer cable is displayed as a single vertical plane or cross-section into the earth beneath the seismic line's location. 3-D seismic data is acquired by towing a large number of cables in parallel. It is displayed as a three-dimensional cube that may be sliced into numerous planes or cross-sections. Two or more 3-D seismic surveys, acquired at different times, can be compared in order to search for changes in the fluids within the rock formations. This type of survey is known as 4-D, where elapsed time is the fourth dimension. Figure 1.4 shows an example 3-D data cube displayed through

Figure 1.3: Image of a seismic vessel in operation. The float seen in the picture are holding the 'door', which provide a sideways lift to maintain streamer separation. The door is shown as an insert in the lower left corner, with some humans standing next to it.

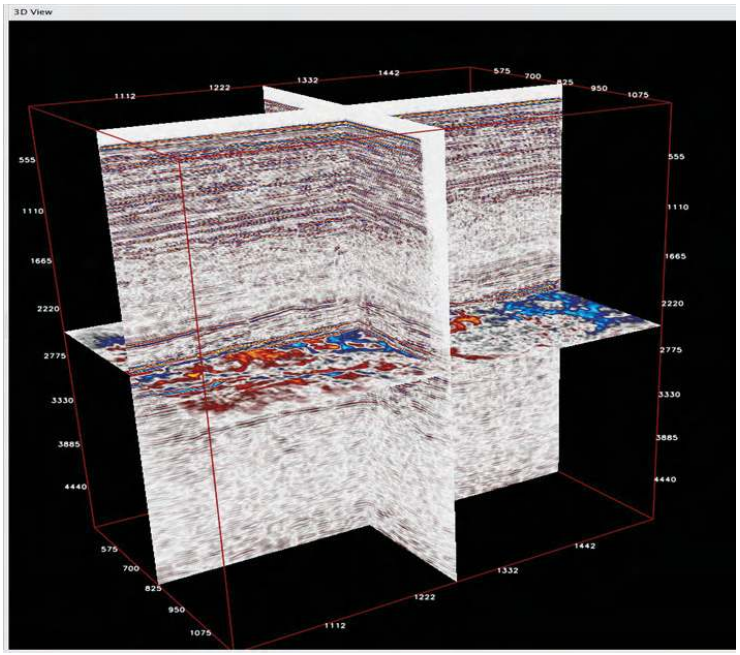

Figure 1.4: A seismic 3-D cube displayed through a number of 2-D planes. Time/depth increase downwards in this image, and the colors represent the magnitude of the reflection from geological features in the subsurface.

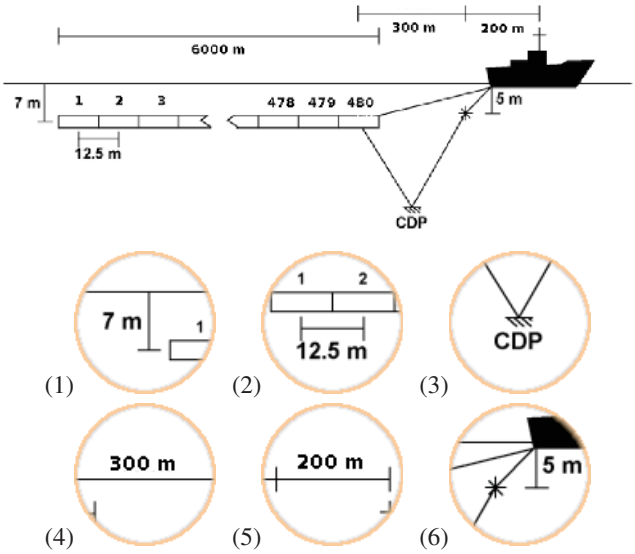

Figure 1.5: A simple but typical 2-D acquisition geometry adapted from a Fugro training program.

several 2-D slices.

1.5 Details on acquisition

We'll start with a simple geometry, as seen in Figure 1.5, to explain some details related to seismic acquisition. The top image shows a marine vessel with one source and one streamer shooting a conventional (2-D) seismic line. The inserts (1-6) in the same figure highlights some details;

1. At which depth (z) a streamer cable is towed is a trade-off between two factors. The deeper the tow, the more quiet is the environment. However, the depth (z) also controls at which frequency the destructive interference of the sea-surface reflection will cause a notch in the spectrum of the recorded data. To first order, this notch is found by

$$f_{notch} = c_o/2z, \tag{1.1}$$

   where c_o is the speed of sound. In most cases, almost all seismic reflection energy is found from zero to around $100\,\mathrm{Hz}$. Consequently, it is not normal to tow a cable deeper than 7-$8\,\mathrm{m}$ below the surface.

2. The group interval (the distance between hydrophone group centers) defines together with the number of channels the basic cable geometry. On most modern cables this is $12.5\,\mathrm{m}$,

i.e., all hydrophones within each $12.5\,\mathrm{m}$ section are summed together to form one time-series (trace/channel). Typically 480 channels correspond to $6000\,\mathrm{m}$ of streamer cable.

3. The "common-depth-point" CDP position refers to the position of the mid-point between the shot and the center of a recording group. This is the physical position of the reflector that represent the geology we try to depict.

4. The offset is the distance from the center of the air gun array to the center of the first recording group. For 2-D surveys we assume that the streamer is in a straight line behind the vessel. In 3-D there is also a lateral offset that needs to be considered.

5. The distance from the navigation recording antenna to the center of the air gun array.

6. The depth of the gun array is as important as the depth of the streamer, and may effect the signature of the source array. The notch frequency, computed from Equation 3.12, will at a depth of $5\,m$ be about $150\,Hz$.

Every time the air gun array fires, each hydrophone group on the streamer cable records the reflected data. One such recording, on one channel, is referred to as a trace, of which an example is shown in Figure 1.6(a).

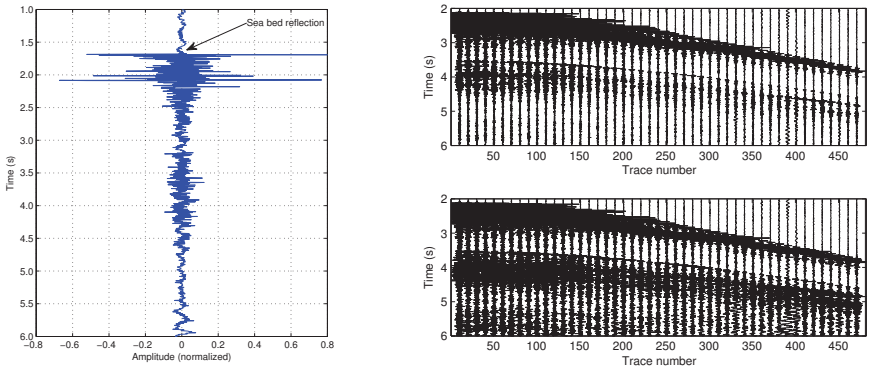

(a) (b)

Figure 1.6: a): Example of seismic trace. Time is increasing downwards. Notice the high amplitude reflections from the seabed, and that amplitudes decrease with time. b): Top: original shot gather where a $4\,\mathrm{Hz}$ low cut filter has been applied. Bottom: The same gather with a gain function. Only a few traces are shown to avoid cluttering the image.

A shot gather, see Figure 1.6(b), is the name of a collection of all traces recorded on the streamer cable after the gun array is fired. A line is a collection of gathers that a vessel has acquired over a period of time, and will typically contain a few hundred or thousand shot gathers. Seismic data is normally stored on disk as lines made up of a number of shot-gathers.
Shot gathers can be sorted by collecting traces that depict the same physical position of the subsurface. Such gathers are normally referred to as "common-depth-point" CDP or "common-mid-point" CMP-gathers. An example of a CMP-gather is given in Figure 1.9. Another way to

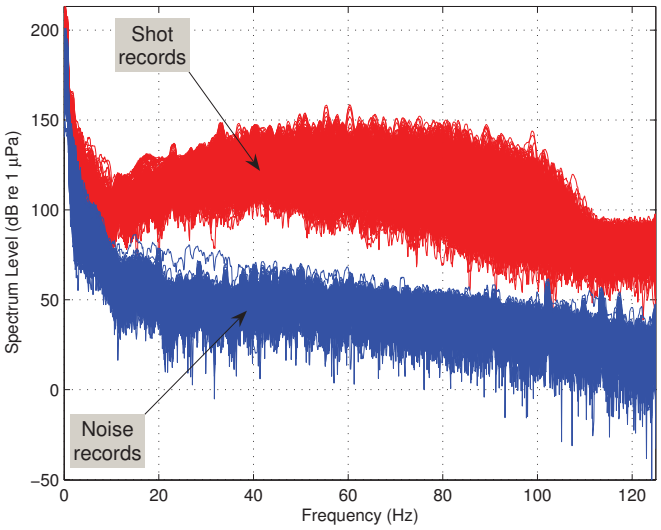

Figure 1.7: Estimates of frequency content of marine seismic reflection data (after the gun-array has been fired) and noise data (no firing of the gun-array). The spectral estimates were computed by a multi-taper method (Thomson, 1982).

sort recorded data is to make common-offset sections. A common-offset section is a collection of all traces recorded by a single channel/group during a line.

Seismic gathers, like the ones presented in Figures 1.6(b) and 1.9, have time or depth increasing downwards and spatial distance x increasing along the horizontal axis, i.e., they are in the t-x domain. Such displays provide a natural view of the subsurface. It is normal to apply some kind of gain-function along the time axis to ensure that weak reflections deep down in the subsurface become visible. Figure 1.6(b) illustrates this, on a typical shot gather.

A number of transforms can be applied to seismic data during processing. The most common is to transform the data into the frequency domain f-x domain). Figure 1.7 shows estimates of the power spectrum from 480 traces in both a typical seismic shot gather, and a typical seismic noise gather (no air gun was fired). Both of these gathers were acquired with a sampling interval of $4\,\mathrm{ms}$, which limits the maximum (Nyquist) frequency to $125\,\mathrm{Hz}$.
For the shot data, high amplitudes are found up to around $80\,\mathrm{Hz}$. The steep tapering off after $100\,\mathrm{Hz}$ is partly caused by a recording filter, but generally most seismic information is found below $100\,\mathrm{Hz}$. The noise data is dominated by low frequencies ($< 10\,\mathrm{Hz}$). However, a problem is that amount of low frequencies noise often degrade the quality of the data.
The frequency content of seismic data will vary depending factors like on the nature of the reflective geology, the size of the source, the depth of the source and the cable, the amount of ambient noise present, and the sensitivity of the equipment used. Various types of noise can

Name	Description
Read data	Read data from tape or disk. (For a typical 3-D survey the amount of data can be around 100Tb.)
QC	Quality control: By studying the noise level and coverage, decide if any special measures are needed.
De-noise	Remove or attenuate noise from the data.
NMO	Normal move-out correction based upon picked sound velocities of the in the subsurface.
Multiple removal	Remove signals that are the result of multiple reflections in the subsurface or between the sea surface and the sea bottom.
Migration	Use some kind of wave equation to geometrically reposition the returned signal to show an event where it is being hit by a seismic wave, rather than where it is being picked up.
Binning and Stacking	Summing up all migrated and NMO-corrected CDP-gathers that correspond to each position in a grid, to improve the signal-noise ratio, and depict the subsurface accurately.
Output	Write the final product to file - to be read and interpreted with 3-D visualization software.

Table 1.1: A simplified processing sequence.

also affect the shape of the spectral estimates.

1.6 Details on processing

Full processing of seismic data, from acquisition to a stage where interpretation can take place, is a long and sometimes complicated process. It is iterative, and it is often based upon trial and error. Furthermore, seismic processing is time-consuming, both in terms of man and CPU-hours, and it is not uncommon that a processing sequence can require months of CPU time on clusters with thousands of processing-cores. The standard reference for seismic processing is Öz Yilmaz (2001). Table 1.1 shows a simplified processing sequence, emphasizing some key processing steps relevant for the work presented later in this work.

1.6.1 Reading data

Seismic data are normally stored on tapes, or on disks. In a typical 3-D survey, the data volumes are large, and often be in the tens or hundreds of Tera-bytes. The shear amount of data puts very high demands on computer systems that need to read in and process such data.

1.6.2 Quality control

Quality control (QC), is a term used to describe an inspection of the data after each stage of processing. A key part of the QC-work is to monitor the root-mean-squared (rms) noise level in the seismic data. This is computed as:

$$x_{rms} = \sqrt{x_1^2 + x_2^2 + .. + x_n^2/n}, \tag{1.2}$$

where x_i are the individual samples in a time-series (trace) with length n. The rms-level is normally computed from data taken from the water column, or towards the end of a record, where little of no reflection data are present. Figure 1.8 shows two examples of rms-plots from acquisition. The increase in noise level towards the front of the cables seen in the top image in this figure and the small peaks that appear with regular intervals in the bottom image are

discussed in chapter 3.

1.6.3 De-noising data

Raw seismic data normally contain lots of noise. This needs to be removed at an early stage of processing in order to obtain accurate images of the subsurface. De-noising seismic data is the main topics covered in chapters 6, 7 and 8.

1.6.4 Normal move-out correction - picking velocities

Normal move-out (NMO) correction is performed on CMP-gathers to compensate for variations in offsets and the speed of sound in the subsurface. The speed of sound c in the subsurface vary from around $1500\,\mathrm{m/s}$ in the water column to above $4000\,\mathrm{m/s}$ in the deep subsurface. A number of other processing steps can also benefit from having NMO-corrected data. The process is computer aided, but it normally requires a great deal of human input. Figure 1.9 illustrates the effects of applying a NMO correction to a synthetic CMP gather.

1.6.5 Multiple removal

The energy that is released from the air-guns is reflected by the geological layers in the subsurface. Unfortunately, one single pulse can be reflected back and forth several times. Some of the signals that are picked up by the hydrophones are therefore not the directly arriving reflections, but what is known as multiples.
The reflective event that can be observes after around $3.5\,\mathrm{s}$ in Figure 1.6(b) is probably a multiple caused the bouncing of the signal between the sea surface and the ocean bottom.

It is beyond the scope of this work to describe all the methods employed during processing to remove or attenuate multiples. However, a common and relevant method is the radon transform. Geophysical usage refers to the particular case where the input data is decomposed into parabolas or sometimes hyperbolas. The τ-p transform is a special case of the radon transform where the decomposition is done along straight lines. Such gathers are commonly also referred to as slowness gathers. In chapters 6 and 8 we will utilize the τ-p transform in a new de-noising approach to remove seismic interference noise. The τ-p transform itself is explained below in a multiple-removal setting:
The top image in Figure 1.10 shows a synthetic shot gather with three dipping events. The traces are $25\,\mathrm{m}$ apart and the timing lines are $0.5\,\mathrm{s}$ apart. The reflection events can be described as follows:
The 'horizontal velocity', shown in Table 1.2, is the velocity at which events moves across the recording spread. This is given by the trace interval divided by the dip. Slowness is the reciprocal of this velocity, measured in seconds per kilometer. In the middle image in Figure 1.10 the linear τ-p transform is applied to the synthetic shot gather. Colors correspond to the dips of the three events. This τ-p gather displays time (vertically) against dip (horizontally). Each of

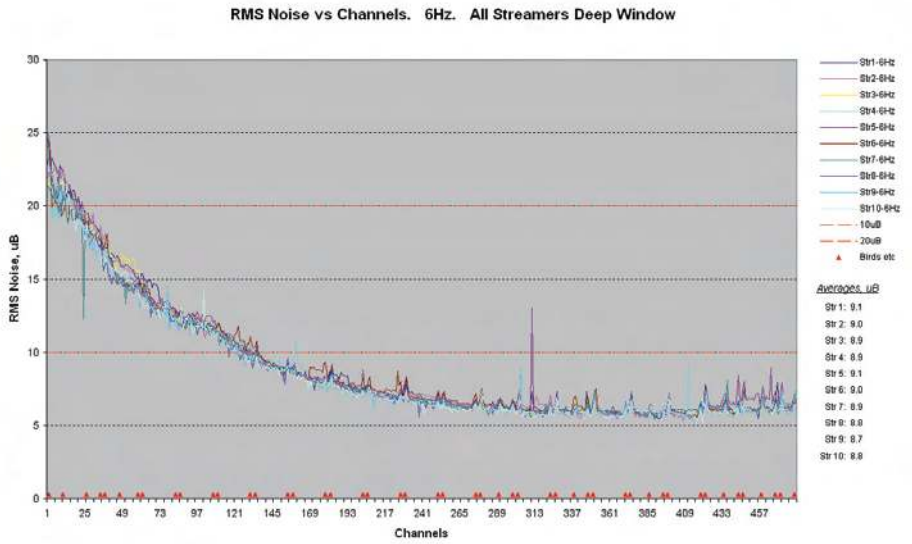

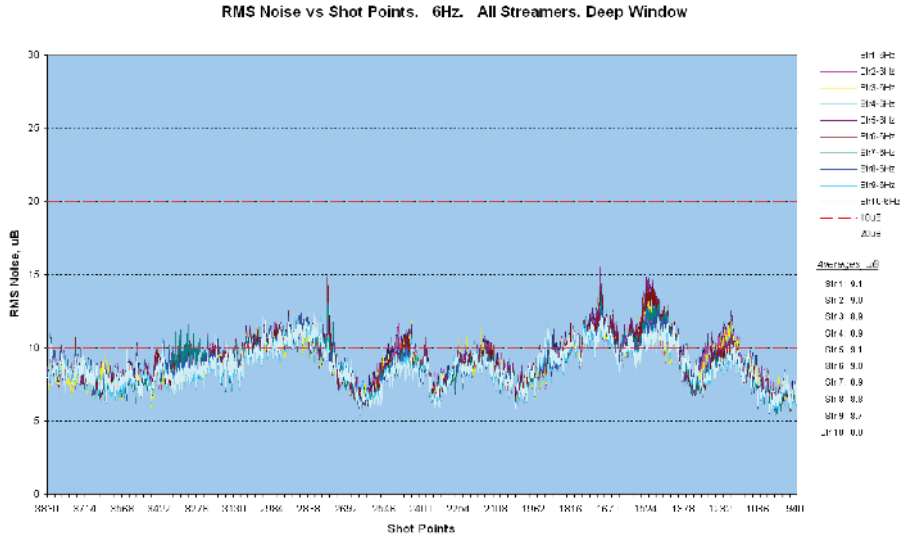

Figure 1.8: Top image: Shows the average rms-noise level on all 480 channels for 10 streamer cables. Bottom image: The average rms-level pr shot pr streamer during a line.

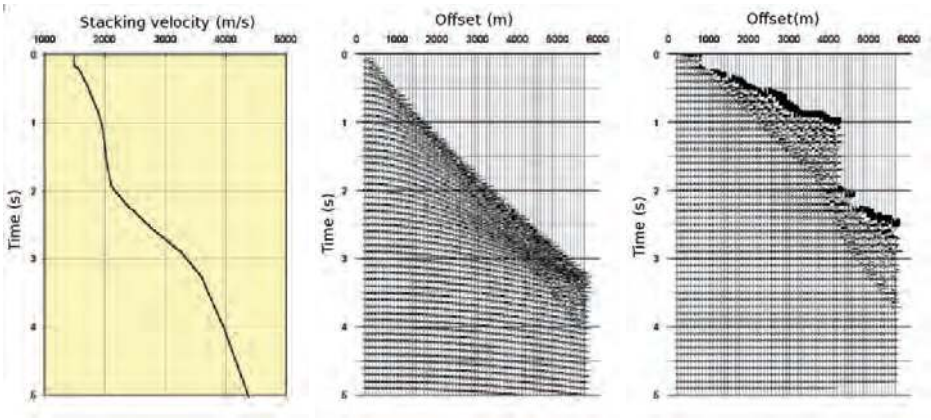

Figure 1.9: From left to right: The velocity function, a synthetic CMP gather and the same gather with NMO correction applied. (Illustrations from the FSI training manual.)

-	Dip	Horizontal Velocity	-
Event	ms/trace	Trace Int. = 25m	Slowness (s/km)
A	-10	-25/0.010 = -2500	-1000/2500= -0.4
B	-4	-25/0.004 = -6250	-1000/6250= -0.16
C	2	25/0.002 = 12500	1000/12500= 0.08

Table 1.2: Table presenting some relevant data for the τ-p transform illustrated in Figure 1.10.

the events from the top image has collapsed (more or less) into a spot, and are easily separable in this domain. The bottom image in Figure 1.10 shows the result of the inverse τ-p transform using only the negative dips in the above transform. Except from a few edge-effects the τ-p transform has cleanly removed the blue event.

1.6.6 Migration

Seismic migration is the process of placing seismic reflection energy in its proper subsurface position. It is a geometric reposition of the return signal to show an event where it is being hit by the seismic wave, rather than where it is picked up. Migration is normally done by employing some type of wave equation on the reflection data, and can be computationally demanding. Migration will not be covered in this work, it will often smear out noisy data to produce blurred and suboptimal images.

1.6.7 Binning and stacking

Binning and/or stacking means that all records of the same CMP position are added together to improve the signal-to-noise ratio and reduce the amount of data. If the signal is assumed to be correlated, while the noise is uncorrelated between individual records, the signal-to-noise ratio of a stack improves like $\sqrt{n} \cdot S/N$. Here, n is the number of records (traces), and S/N

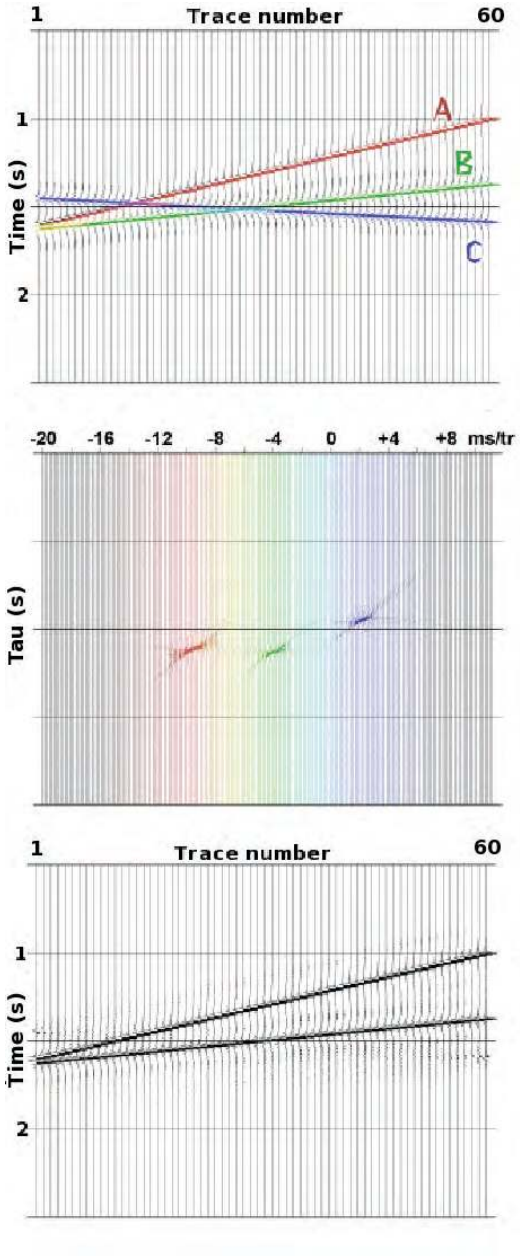

Figure 1.10: Illustration of how the τ-p transform can be used to discriminate between different dipping events. Top image: a synthetic gather with three reflections. Middle image: The same gather transformed into the τ-p (slowness) domain. Bottom image: the result of transforming the τ-p gather back to the time domain after the blue event has been muted. (The illustrations are adapted from the FSI training manual.)

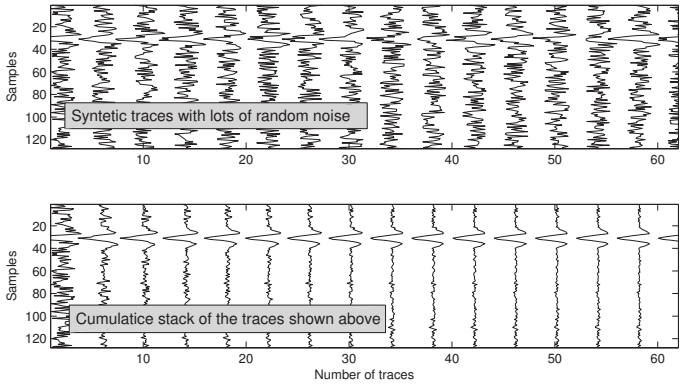

Figure 1.11: Top image: Synthetic seismic data with one reflection event around sample number 40, and random noise. Bottom image: The cumulative stack of the data above. Notice that the uncorrelated noise is attenuated, while the correlated seismic event gradually stand out more clearly.

is the signal-to-noise ration of a single trace. With hundreds of records from each CMP, this represent a powerful de-noising method, as illustrated in Figure 1.11. However, occasionally high amplitude noise survives this stacking process. Additional de-noising tools are therefore sometimes required. In modern processing binning and stacking is often done quite late in the processing sequence.

1.6.8 Output

Output means the data now is ready for interpretation. After this stage it is normal that oil-company geologists try to merge the seismic data with geological knowledge in order to identify possible oil-bearing geological structures. If the likelihood of oil and gas are sufficient, then drilling exploration wells is the next step. Finally, if also these test wells show promise, decisions about weather to start production are taken. Typically, it will take a decade from a potential oil-bearing structure is identified in the seismic data, until the first oil is pumped from an offshore oilfield.

Chapter 2

The work done in this thesis

This chapter gives an overview of the topics in this thesis. It also provides background material, intending to show how the topics covered in this work fit together within a larger framework. The chapter ends by showing a number of examples of software de-noising, utilizing a program written as part of this thesis work.

2.1 Background

During the last decades, advances in seismic exploration technologies have made it possible to search for hydrocarbon deep down in the surface and in areas with complex geology. Improvements in accuracy have also made 4-D surveys increasingly common, as oil companies want to observe the small changes in the geological layers as a field is depleted. These advances have come with a cost. Operations today are increasingly complex, and often require several vessels. Currently, marine seismic operations are also close to practical limits in terms of streamer length ($10\,\mathrm{km}$) and source size (4000 cubic inches). Nevertheless, system improvements are still possible in a number of fields to aid the exploration in deep and complex geological areas (e.g., below salt).
One of the main factors that obscure deep targets, and lowers the resolution of subsurface depictions is noise, of which

- swell/flow noise from the interaction between the streamer cable and the surrounding flow
- interference noise - caused by other seismic vessels, or oceanic traffic

are the two most common types. Figures 2.1(a) and 2.1(b) show typical examples of both of these noise types. Other types of noise like instrument noise, propeller/cavitation noise, noise from marine life (biological noise), and general background noise (Wenz, 1962) can occasionally also be significant. However, in most cases, they are marginal, and they will not receive any in-depth treatment here.
Bad weather (big waves) is the main reason for excessive swell noise. When the noise level exceeds a predetermined limit, vessels go on weather standby. Recent numbers, provided by vessel manages in Fugro Geoteam AS, indicate that on average, modern seismic vessels spend

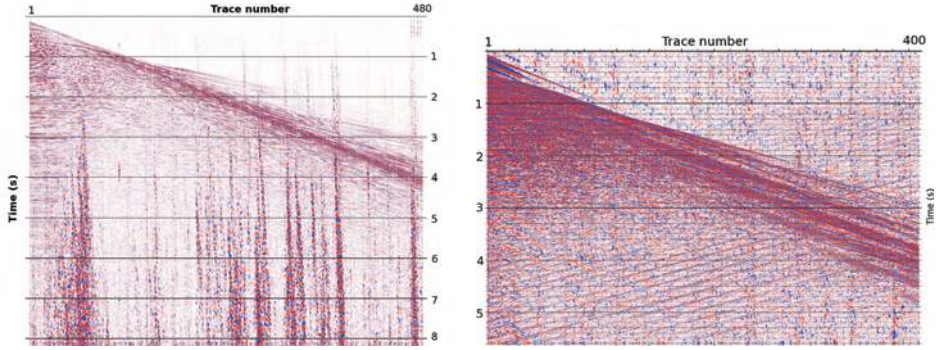

Figure 2.1: Image a): Example of a 2-D shot gather (480 traces times $8\,\mathrm{s}$) containing lots of seismic (swell) noise. The noise can be observed as vertical stripes in the data containing high amplitude low frequency disturbances. Image b): Example of 2-D shot gather (400 traces times $5.5\,\mathrm{s}$) containing seismic interference noise. The noise is in the form of straight lines going from lower left to upper right in the image.)

about 20% of their time on weather standby. This number varies with both geographical position and seasons. However, weather standby does have significant financial implication, in that it normally imply reduced rates.

When wave-heights exceed 3 to $4\,\mathrm{m}$ noise is not the only limiting factor. There is also the issue of safety, both for the equipment and for the crew on the back deck. Nevertheless, surveys are more often halted because of excessive (swell-) noise than they are due to dangerous weather, and even in fairly calm conditions there are often significant amounts of noise in seismic recordings.

To avoid or reduce all kinds of noise contamination there are two approaches that we can follow. The first is to make sure that we record as little noise as possible, i.e., have optimally engineered acquisition equipment, and operate this equipment correctly. The second approach is to remove the recorded noise through software processing. This thesis presents work done in both of these fields.

Avoiding noise during acquisition, and de-noising the data once it is acquired, are important first steps in the process of accurately depicting the subsurface geology. If these first steps are suboptimal, then one can not expect to get good results from subsequent multiple removal, migration and stacking operations. That is, the quality of the final product depends directly on our ability to acquire and process data with a good signal-to-noise ratio.

2.2 Physics of noise generation

Flow and swell noise generation on streamer cables is a topic that is treated in chapters 3 and 4. The physical background for the work presented there are the Navier Stokes equations, which, accurately describe the motion of fluids. These equations arise from applying Newtons second law to fluid motion and express the conservation of mass and momentum on a fluid element that is subjected to both pressure and viscous forces. In tensor notation, and assuming

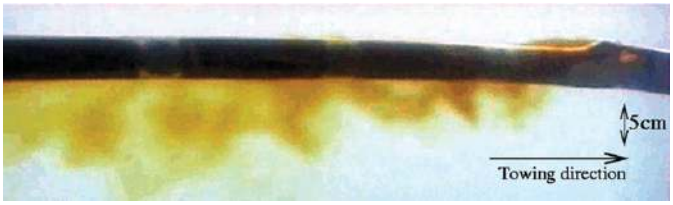

Figure 2.2: Image of a seismic streamer towed at 4 knots. An environmentally friendly dye is released to reveal structures in the turbulent boundary layer. (A movie of this flow can be seen at http://ecommons.cornell.edu/handle/1813/11456.)

incompressibility the Navier Stokes momentum and continuity equations read:

$$\frac{\partial u_i}{\partial t} + u_j \frac{\partial u_i}{\partial x_j} = -\frac{1}{\rho}\frac{\partial p}{\partial x_i} + \nu \nabla^2 u_i \tag{2.1}$$

$$\frac{\partial u_i}{\partial x_i} = 0. \tag{2.2}$$

Here, u_i denote velocity in the i'th direction, $i \in \{1, 2, 3\}$, p denotes pressure and ρ is density. Repeated indices imply summation. Almost all 'real life' fluid flows are turbulent. In the Figure 2.2 we observe turbulent structures (eddies) with a diameter of typically 5-20 cm surrounding a towed seismic streamer array in the ocean. When these eddies pass along the hydrophones inside the streamer they induce pressure fluctuations that we indirectly observe as flow noise.

In the 1950ś, Lighthill, who worked on problems related to airplane jet noise, manipulated the Navier-Stokes equations to obtain a so-called acoustic analogy. The left hand side of this equation then becomes a wave operator, while the right hand side becomes an expression for the acoustic sources in the fluid flow. In mathematical language, followings Landau and Lifshitz (1987), this can be written as:

$$\frac{\partial^2 p}{\partial t^2} - c_0^2 \frac{\partial^2 p}{\partial x_i^2} = \rho_0 \frac{\partial u_i u_j}{\partial x_i \partial x_j}. \tag{2.3}$$

Here p is pressure, ρ_0 denotes the assumed constant fluid density and c is the speed of sound in the media. For water, $c \approx 1500\,\mathrm{m/s}$. The source term (the right hand side of this equation) has a number of interesting properties. Since it generally comes from turbulent fluctuations, it is a quadrupole source. This implies that its intensity drops off like $1/r^4$ with distance from the point at which it was created. However, flow noise may still be strong on sensors mounted just below the surface of an array (or a hull), like the one seen in Figures 2.2 and 2.5. This also means that as a towing vessel increase speed, the flow noise level will increase rapidly. For instance, twice the speed implies eight times more intensity. These topics will be covered in more detail in chapters 4 and 5.

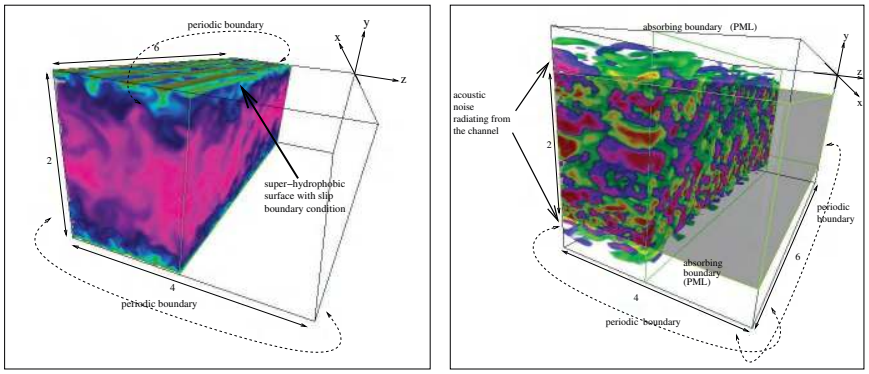

(a) (b)

Figure 2.3: Image a): Snapshot from a direct numerical simulation of channel flow (Martell et al., 2009). Colors indicate the instantaneous flow velocity, while a cut-plane is used to better look inside the flow. Image b): Snapshot of the acoustic noise produced by the same flow.

2.3 Simulating flow noise

For all real life flows, Eqs 2.2 and 2.3 are impossible to solve exactly. However, they can be simulated or modeled. The simulation of Equation 2.3 is the topic of chapter 5, and again in chapter 9.

A direct numerical simulation (DNS) is the most accurate tool available to simulate fluid flow. In a DNS all scales of fluid motion are resolved. However, as the Reynolds number (ratio of inertial to viscous forces) of the flow increases, so does also the cost of the computations. Even on large supercomputers, only low to medium Reynolds number flows can be resolved. The combination low Reynolds number DNS and correct (large) Reynolds number measurements, is never the less useful in order to gain a physical understanding of flow and swell noise generation. Figures 2.3(a) and 2.3(b) show a 3-D visualization of a DNS channel flow and the corresponding flow noise, respectfully. Flow noise inside a streamer cable is visualized in Figure 2.4, where the noise is produced by a turbulent flow that surrounds the cable.

The software programs used to simulate the flow noise propagation is one of the things that was specially written for this thesis. These simulations enable us to investigate features that often are difficult or impossible to measure in real life flows.

2.4 Measurements of noise from seismic streamer cables

During this project we have had access to large amounts of commercial seismic data which are collected on streamer cables with group-length of around $12.5\,\mathrm{m}$. That means that a recorded signal (trace) represents the average signal picked up by all sensors (hydrophones) within these $12.5\,\mathrm{m}$. Analysis of such streamer data is the topic of chapter 3. In practice, group-forming reduces both the noise level and the amount of data that needs to be recorded. Unfortunately it also removes important information about the nature of the noise seen by each individual

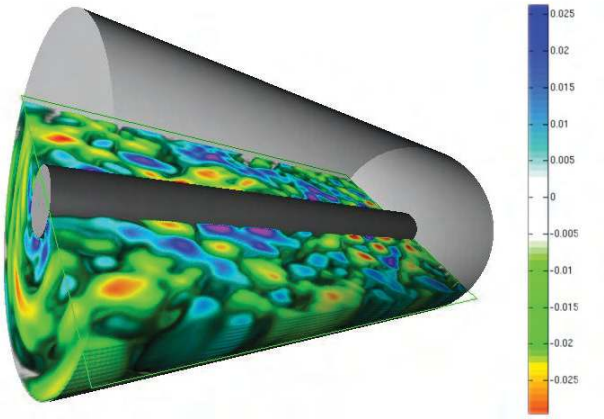

Figure 2.4: Flow noise propagating inside a streamer array. The outer circle in this image represents the streamer hose, while the inner cylinder represents the wiring that pass through the center of a streamer cable. A cut plane is applied for better visualization. The numbers in the color-bar are used to indicate areas of high and low pressure. An animation from this simulation can be found at http://folk.uio.no/thomae/MEKIT09/cylinder.avi.)

Figure 2.5: Parts of a hydrophone array during manufacturing.

hydrophone. To obtain single sensor data we had a seismic sensor cable specially designed and built. The analysis of the data from this array is presented in chapter 4.

Figure 2.5 shows parts of the hydrophone array that we designed to in investigate flow noise. The sensor elements (hydrophones) in this picture are separated by only a few cm. In Figures 2.6(a) and 2.6(b), the purpose built cable is deployed from a vessel to obtain noise records. The motivation for building and measuring noise on such a specially designed cable was twofold. First it enabled us to measure how flow noise behaved on a cable in the ocean. Based on these measurements we could then describe some features of the noise statistically, e.g., what is the average spatial correlation distance of the flow noise? The second motivation was that it provided real data, which we could use to tune our simulation programs.

(a) (b)

Figure 2.6: Image a): From a test where a purpose built hydrophone array is deployed behind the research vessel H.U. Sverdrup. Image b): The same streamer on a winch before deployment

2.5 Superhydrophobic surfaces

The topic of chapter 9 is how turbulent flow noise (and drag) can be reduced on existing equipment. To achieve this we have looked at superhydrophobic surface (SHS) coating materials that support a non-zero (slip) velocity at the surface. Rothstein (2010) cite a large number of publications where SHS are used to reduce drag, both for laminar and turbulent flows. We show that SHS coatings also can be used to reduce flow noise. This is a new observation, that we presently work to exploit in an industrial setting. Having experimentally proved that it works, we now cooperate with chemists to develop coatings that aren't washed off. The coat also needs to be acoustically transparent, and we want to combine it with 'anti fouling'. That means that is should repel barnacles, see image in Figure 2.7(a), and other marine life forms that often attach to and grow on seismic equipment in tropical waters. Figure 2.7(a) is from one of our first experiments with superhydrophobic coating on seismic streamer cables, where we measured the reduction in drag.

2.6 Signal processing

Once seismic data has been acquired, the only remaining way of signal-to-noise ratio improvement is through software de-noising. The technology that has made this attractive to is the development in processing power of modern computers. A decade ago, only applying band pass filters in certain areas to attenuate noise might have satisfied us. Today complicated transformed performed in adapting windows are commonplace. Multiple iterations are also normal, and de-noising is an integrated part on nearly all processing flows. As part of this thesis work, a de-noising algorithm was developed and programmed in the seismic processing package UNISEIS. This package is used by the geo-science company Fugro at its offices and vessels worldwide. We called the de-noising module TFDN (time-frequency de-noise). Chapter 6 explains in

(a) (b)

Figure 2.7: Image a): From a towing test where we measured the drag reduction obtained by applying a superhydrophobic coat on a seismic streamer section. Image b): A barnacle infested seismic streamer.

detail how the module works, while chapters 7 and 8 present a number of processing examples where TFDN was applied to noisy seismic data.

TFDN works by using a sliding window, both in space and time. A spectral estimate of all traces within this window is first computed. The amplitudes at each frequency are then compared with the amplitude of a presumed good trace within the chosen window. If the amplitude is larger than a user-supplied threshold factor times the presumed good amplitude, the amplitude in question is attenuated to the level of the presumed correct trace. This process is repeated for all frequencies specified by the user. The modified spectrum is finally transformed back to the time domain, and so on for each sliding window. In this way, we do not simply remove the parts of the frequency spectrum that are affected by noise. We also try to predict what the actual amplitude of the affected frequency should have been, based upon a spectral estimate of a presumed good trace in its neighborhood.

Table 2.1 shows a typical parameter file for the TFDN module, while Figure 2.8 illustrates how the sliding window (the white rectangle) moves across a seismic gather and attenuates abnormal data. The good thing with having many users of a program is that it is easy to get feedback. The TFDN module has benefited very much from user feedback, and with regular intervals we have added new functionality to it. Today, it is the standard tool for de-noising within Fugro, and are being used daily by users at a number of locations. The TFDN algorithm is not unique, and several other companies have similar programs. However, we feel confident that the speed (tuned F77 code), and flexibility of the TFDN module outperforms most other codes.

Initially the TFDN module was developed to help attenuate swell-noise. This is also its primary usage. However, as we have gained more experience with it, the seismic processors have also started using the module to attenuate other types of noise. These new noise attenuation methods often involves sorting or transforming the data to randomize the noise, before the ac-

Parameters	Description
**TFDN	The calling of the module
TIMR,1000,8000	Start and end time of processing (in ms)
FREQ,0,12	Frequency range to process (0 to 12 Hz)
HWIN,40	Horizontal size of sliding window (in number of traces)
TWIN,500,4	Vertical size of sliding window and window move-up (in ms)
THRS,MED,4	Threshold (attenuate if it is more than 4 timed the median)

Table 2.1: A typical parameter file for the TFDN de-noising module. Here the median is used as a measure of a noise free amplitude. However, several other options are also available.

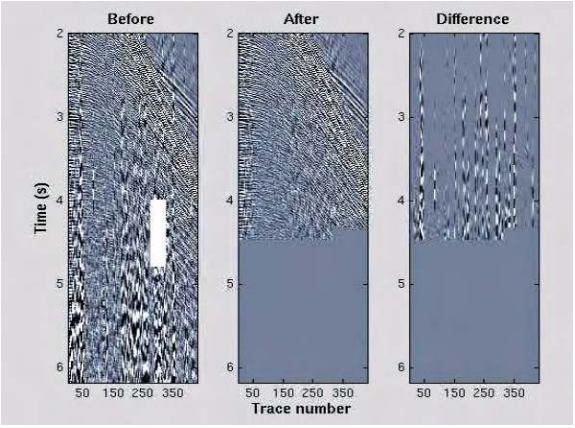

Figure 2.8: Before, after and difference plot illustrating how the sliding window (the white rectangle) move over a seismic gather in TFDN, and attenuates abnormal frequencies. A movie illustrating this can be found at http://folk.uio.no/thomae/animations/tfdn.mpg.

tual de-noising is performed. In most cases it is sufficient to sort shot gathers to the CDP or the common offset domain to make the noise random. Nevertheless, sometimes more drastic measures are needed. A processing sequence that involves sorting data in the radon and/or τ-p domains are explained in chapters 6 and 8. A recent approach, used in Figure 2.15, is to randomize traces within a given gather to break up the noise.

On the next pages we have added a number of before, after and difference plots of TFDN applied to various noisy data gathers. All of these examples are taken from recent commercial processing jobs by various Fugro Seismic Imaging offices. The thing to notice about these before-after and difference plots, is how little visible seismic information that can be seen in the difference plots. The ability to preserve good data is the main reason for the success of TFDN.

- Figure 2.9 shows a seismic shot gather, heavily affected by low frequency swell-noise (below 15 Hz).
- Figure 2.10, shows a seismic shot gather, heavily affected by broad banded interference noise from another seismic vessel.
- Figure 2.11, shows a stacked section, where the shot-gathers were heavily affected by swell noise.
- Figure 2.12, shows part of another stacked section, where the shot-gathers were heavily affected by low frequency swell noise.
- Figure 2.13, shows a CDP-gather acquired while the vessel was passing a drilling rig that emitted broad-banded noise.
- Figure 2.14, shows a stacked section acquired while the vessel was passing a drilling rig.
- Figure 2.15 shows a common offset section where the last traces are troubled by high frequency diffraction noise (multiples) caused by a very hard ocean bottom. The multiples could not be removed by traditional methods due to the short offset (1200 m streamer), so TFDN noise removal was used instead.
- Figure 2.16 shows a shot-gather (10 streamers) where a 'singing' whale passed under the spread.
- Figure 2.17 shows part of a shot-gather where both low frequency swell noise and high frequency noise probably caused by snapping shrimps from the Alpheidae family.
- Figure 2.18 shows the average rms-level for each shot in a 3-D survey before and after the application of TFDN for (swell-)noise attenuation.

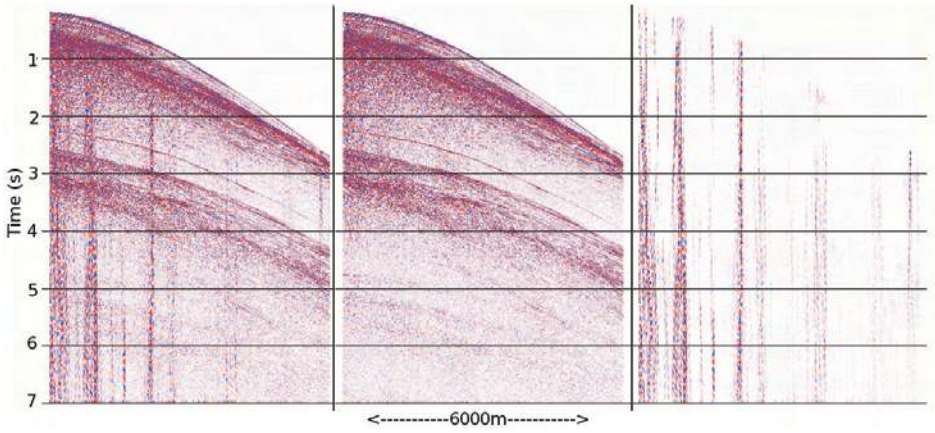

Figure 2.9: Before, after and difference plot of a 480 traces 7 s shot gather affected by swell noise, caused by large waves.

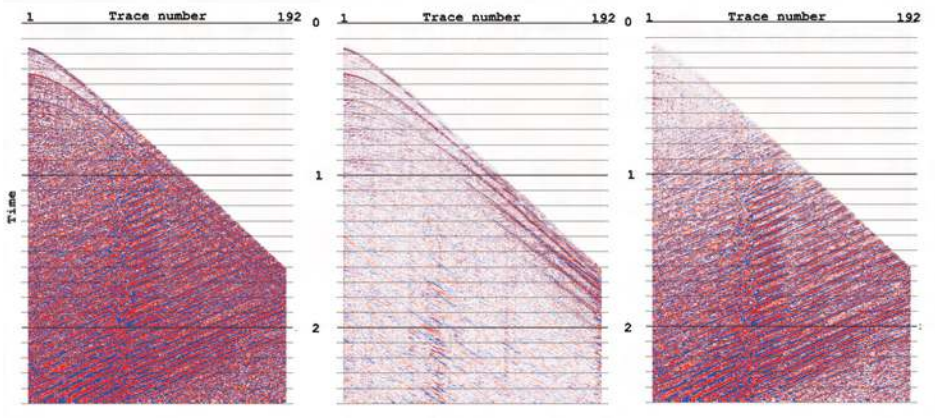

Figure 2.10: Before, after and difference plot of a 192 traces 2.5 s shot gather affected by broad banded seismic interference noise, coming from a nearby seismic vessel.

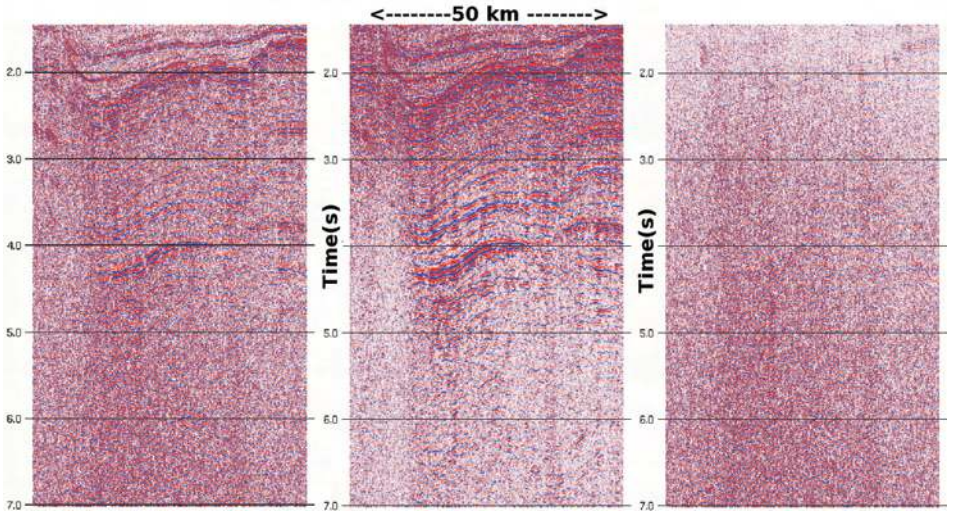

Figure 2.11: Before, after and difference plot of a seismic stack, where the input data was affected by low frequency swell-noise.

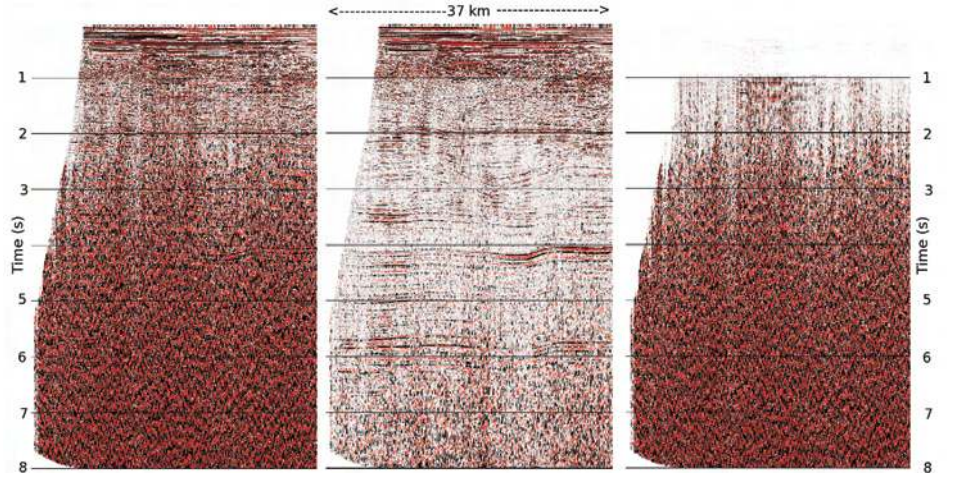

Figure 2.12: Before, after and difference plot of part of a seismic stack, where the input data was affected by low frequency swell-noise.

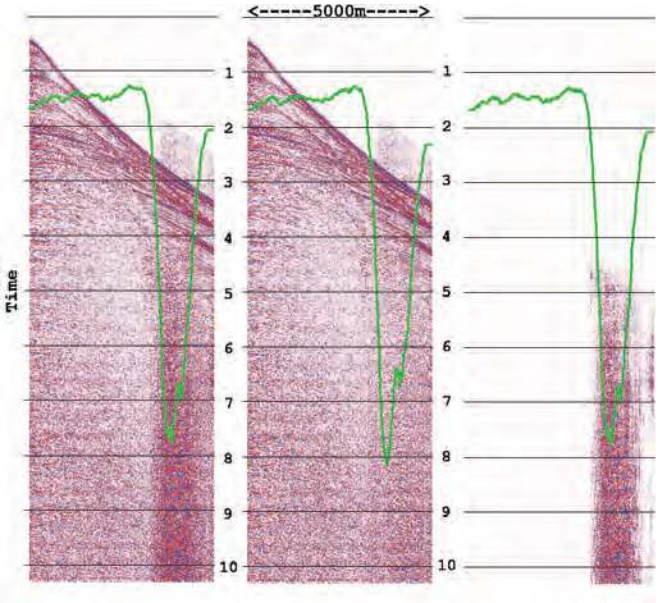

Figure 2.13: Before, after and difference plot of a seismic CDP-gather, where the input data was affected by high frequency noise from a drilling rig. The green line indicates the rms-noise level (inverse) in a short time-window towards the end of the gather.

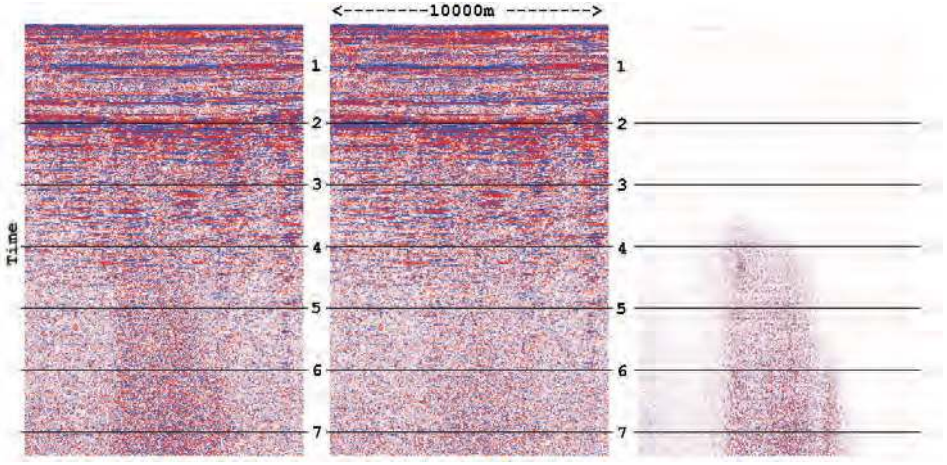

Figure 2.14: Before, after and difference plot of a seismic stack, where the input data was affected by high frequency noise from a drilling rig.

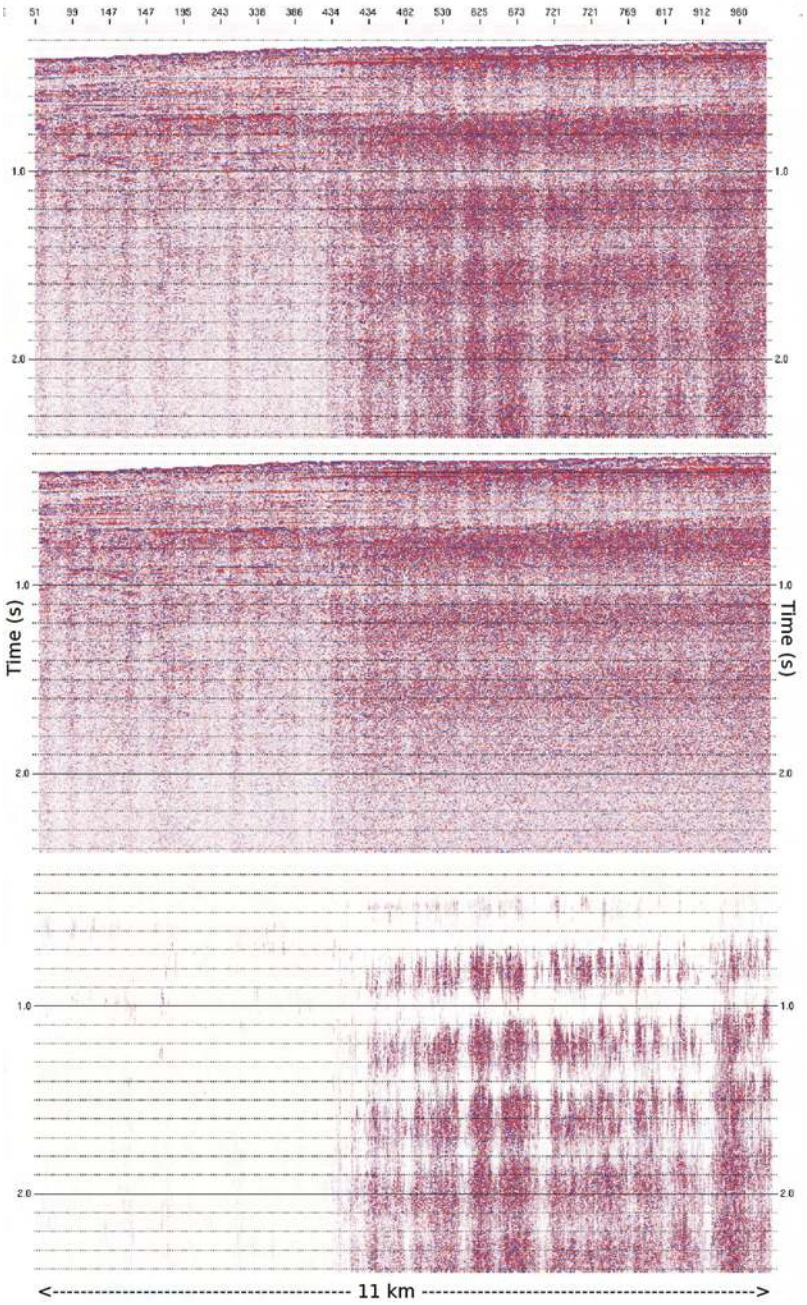

Figure 2.15: Before, after and difference plot of a common offset section with diffraction noise in the left part of the gather. The de-noising was done by first randomizing all traces. Then TFDN was applied, before the traces were put back in their right order.

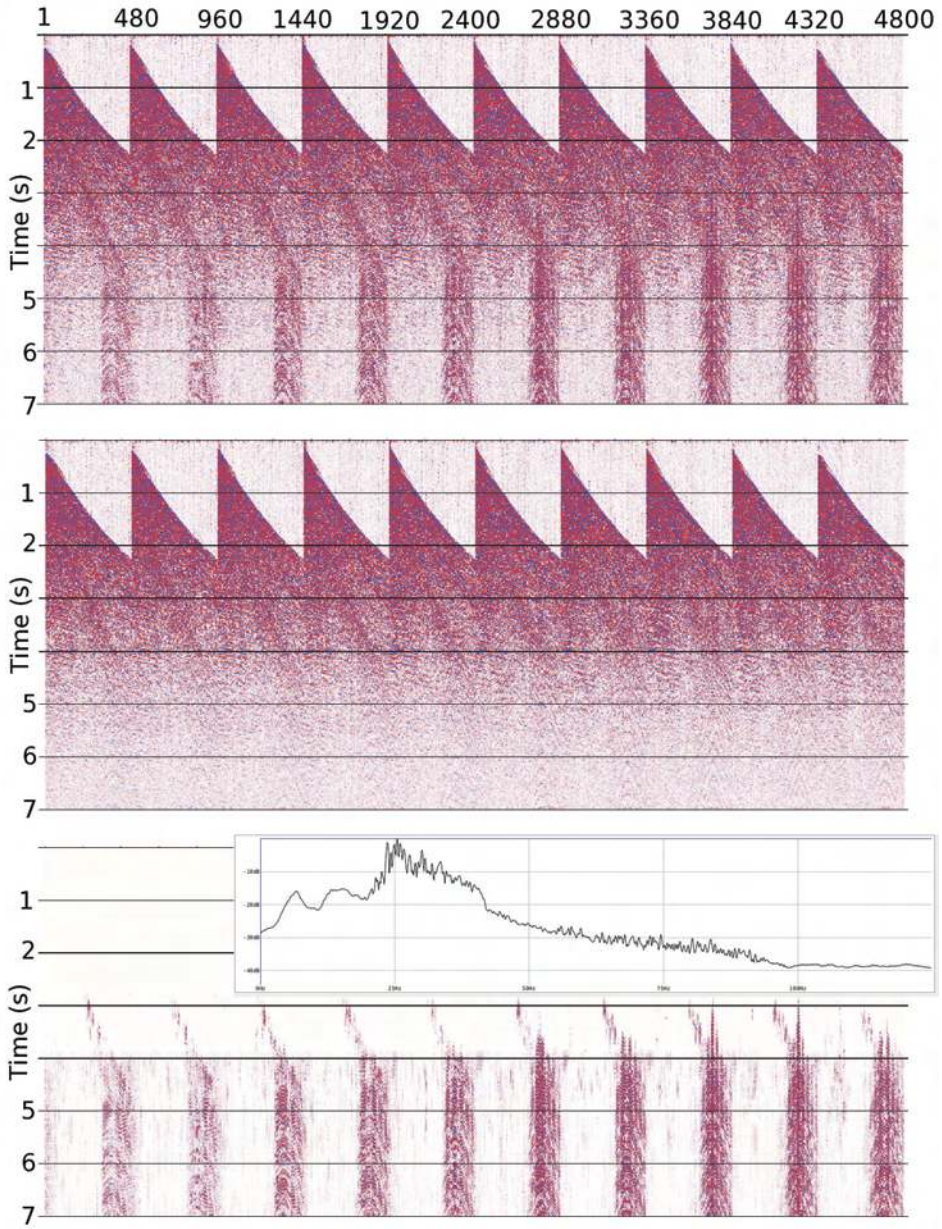

Figure 2.16: Before, after and difference plot from a shot-gather (ten streamers each with 480 channels), where a whale made sounds in the 25 to 35 Hz range around 5 km behind the vessel. The insert shows a frequency estimate of the difference plot, e.g, the noise made by the whale.

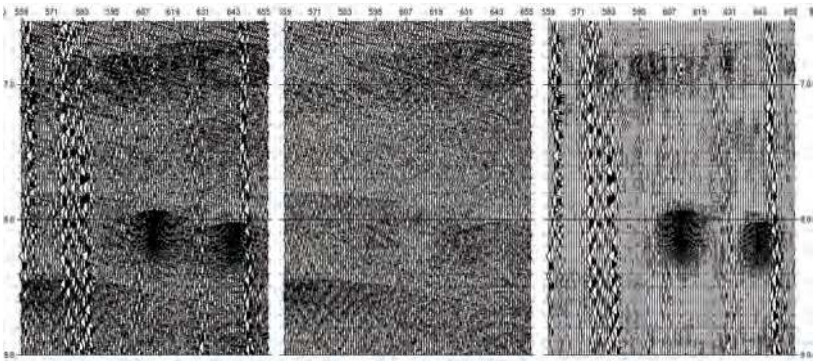

Figure 2.17: Before, after and difference plot of part of a shot gather with both low frequency swell noise and high frequency intermittent noise. The high frequency noise is probably caused by snapping shrimps in the Gulf of Mexico.

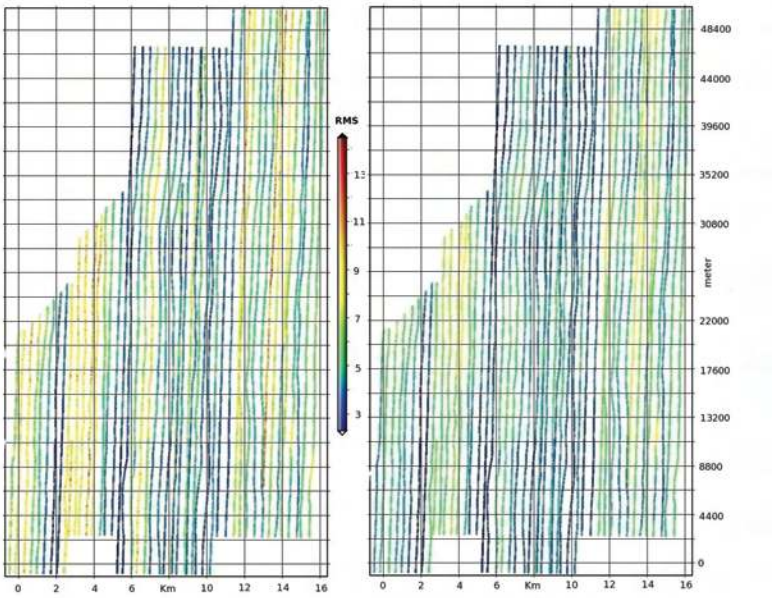

Figure 2.18: Average rms-noise level pr shot color-coded for an entire 3-D survey. Left and right: before and after applying time-frequency de-noising. Blue and green indicate low, while yellow and red indicate high noise levels.

Chapter 3

Flow and swell noise in marine seismic

Thomas Elboth <thomae@math.uio.no>
Fugro Geoteam AS, Hoffsveien 1c, P.O.Box 490 Skøyen N-0213 Oslo, Norway
Mechanics Division, Department of Mathematics, University of Oslo, Norway
Bjørn Anders Pettersson Reif <Bjorn.Reif@ffi.no>
Norwegian Defense Research Establishment (FFI), P.O.Box 25 2027 Kjeller, Norway
Mechanics Division, Department of Mathematics, University of Oslo, Norway
Øyvind Andreassen <Oyvind.Andreassen@ffi.no>
Norwegian Defense Research Establishment (FFI), P.O.Box 25 2027 Kjeller, Norway

Article originally published as:
T. Elboth, B. A. Pettersson Reif and Ø. Andreassen: Flow and swell noise in marine seismic data, Geophysics 74(2), Q17-Q25 (2009)

Abstract

Various weather related mechanisms for noise generation during marine seismic acquisition is addressed from a fluid dynamical perspective. This is done by analyzing a number of seismic lines recorded on modern streamers, during non-optimal weather conditions. In addition we provide a description of some of the complex fluid mechanical processes associated with flow that surrounds seismic streamers. The main findings are that noise in the 0-2 Hz range mostly is the result of direct hydrostatic pressure fluctuations on the streamer caused by wave motion. For normal 'swell-noise' above 2 Hz, and for 'cross-flow noise', a significant portion of the observed noise probably comes from dynamic fluctuations caused by the interaction between the streamer and fluid structures in its turbulent boundary layer. This explanation differs from most previous works which have focused on streamer oscillations, bulge waves inside old fluid filled seismic streamers or strumming/tugging as the main source for the generation of weather related noise. Even though modern streamers are known to be less sensitive to such sources of noise, their ability to tackle the influence on 'turbulent flow noise' has not improved. This implies that noise induced by turbulent flow has increased its relative importance on modern equipment, and that in order to improve the signal-to-noise (S/N)-ratio on seismic data, design issues related to flow noise need to be addressed.

3.1 Nomenclature

a	=	streamer radius (m)
α	=	streamer incidence angle (deg)
C_D	=	tangential drag coefficient
δ	=	boundary layer thickness (m)
δ_{ij}	=	Kronecker delta
ϵ	=	viscous dissipation rate (m^2/s^3)
F_D	=	drag force (N)
η_κ	=	Kolmogorov micro-scale (m)
l	=	integral length scale (m)
L	=	streamer length (m)
ν	=	kinematic viscosity (m^2/s)
Re	=	Reynolds number. $Re_L = UL/\nu$, $Re_\delta = U\delta/\nu$
ρ	=	fluid density (kg/m^3)
τ	=	shear stress (N/m^2)
τ_w	$\equiv$	$\mu(\partial U/\partial y)_{y=\delta}$, shear stress on surface (N/m^2)
θ	$\equiv$	$\int_{y=\delta}^{y=\infty} \frac{U}{U_0}\left(1-\frac{U}{U_0}\right)dy$, momentum thickness (m)
$\overline{u_i u_j}$	=	Reynolds stresses (m^2/s^2)
U_0	=	tow speed or free-stream velocity (m/s)
u_τ	$\equiv$	$\sqrt{\tau_w/\rho}$, friction velocity (m/s)
y	=	distance from the wall (m)
y^+	$\equiv$	yu_τ/ν, dimensionless wall distance

3.2 Introduction

Marine seismic data always contain components of noise originating from various sources. Weather is often the main source of much of the recorded noise and can according to Smith (1999), induce delays that account for up to 40% of the total cost of a marine survey. Important work to determine noise characteristics and identifying sources of noise on seismic streamers was done by Schoenberger and Mifsud (1974). Since then, the seismic industry has focused on improving streamer system technology to reduce the effects of many of the identified sources of noise. For instance, innovative engineering solutions and the introduction of new materials have greatly reduced noise from tugging and virtually eliminated electrical interference on modern equipment. Peacock et al. (1983), Bjelland (1993) and Dowling (1998) made significant contributions to the understanding of noise generation mechanisms on fluid filled seismic streamers. The primary mechanism under bad weather conditions, was identified to be longitudinal wave propagation inside the streamer that create low-frequency noise. These waves were caused by tugging and strumming from the vessel, paravanes, and tail-buoy together with lead ins, tow and cross cables. Brink and Spackman (2004) and Dowle (2006) showed that modern foam filled streamers are less sensitive to such internal bulge-waves as well as vibrations from external forces like tugging/strumming. A possible noise generation mechanism for flexible slender cylinders was identified by Paidoussis (1966) in the form of buckling and oscillatory instabilities. For seismic streamers, Parrish (2005) on the other hand, shows that such oscillations most

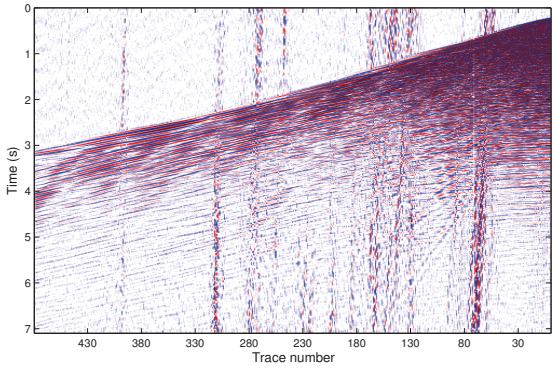

Figure 3.1: A shot gather where weather related noise show up as vertical stripes.

likely will only be found at frequencies well below one Hz.
In recent work presented by Landrø (2008) the signal remaining from the previous seismic shot is considered as a source of noise. For a seismic line acquired in the North Sea he shows that after 8 s, using a 5.3 Hz low-cut filter, the rms noise from the previous shot is $2.5\mu Bar$. After 15 s the noise is around $1\mu Bar$. This is a significant percentage of the overall noise in good weather. However, in a non optimal weather situation it makes up less than 5 percent of the rms noise level.
External sources of noise may also adversely affect the quality of the seismic data. These include for instance seismic interference, engine and propeller noise and wind and bubbles near the surface. While the latter probably is secondary, the two other can arguably be avoided by careful operational planning.
This work combines applied geophysics and fluid dynamics in an attempt to provide a description of some of the complex processes associated with towed streamer arrays used for marine seismic exploration. More precisely it deals with two distinctly different sources of noise. First low frequency hydrostatic pressure fluctuations originating from the wave-induced vertical motion of the ocean. Secondly, dynamical pressure fluctuations on the surface of the streamer generated within the surrounding turbulent boundary layer. It will be argued that on modern streamers operated during non-ideal weather conditions, these noise sources are significant, and will often dominate most other common types of noise. A typical example of noisy streamer data from a solid streamer recorded during 7s is shown in Figure 3.1. This weather related noise has large amplitudes at low frequencies, and it is spatially coherent over a number of hydrophones.

3.2.1 Literature and fluid mechanical background

The flow past a circular cylinder is a classical problem in fluid mechanics. Unfortunately, most of the work performed has been on steady flow normal to the cylinder axis ($\alpha = 90°$). For seismic streamers we typically have $\alpha = \pm 5°$, and the available literature is more limited.

Early work focusing mainly on the average flow on axially symmetric cylinders ($\alpha = 0°$) were carried out by Willmarth and Yang (1970), Denli and Landweber (1979) and Willmarth et al. (1975). They investigated wall pressure fluctuations in conjunction with the mean velocity profiles. Willmarth and Sharma (1984) and Snarski and Lueptow (1995), performed similar studies where also the turbulent flow properties were investigated. In the latter study two different groups of fluctuations in the turbulent boundary layer surrounding a cylinder were identified. First, low frequency high energy fluctuations originating from the outer parts of the boundary layer, possibly in the form of large scale coherent structures. Secondly, small scale, high frequency disturbances related to the so-called burst-sweep cycle. These disturbances probably make a significant contributions to the fluctuating rms-pressure near a cylinder surface.

Both Lueptow et al. (1985), and Heenan and Morrison (2002a), as well as a number of other researchers have shown that even small misalignments of the axis of the cylinder relative to the mean flow will cause asymmetry of the boundary layer and induce significant deviations in the fluctuating wall pressure levels around the circumference of the cylinder. Based on measurements, Lueptow et al. (1985), and Furey (2005) provide statistics on the distribution of the Reynolds stresses within the turbulent boundary layer at $\alpha = 0°$. The Reynolds stresses, $\overline{u_i u_j}$ are the ensemble average product of velocity fluctuations at the same spatial location, where over-bar indicated the ensemble average operator. Their physical significance is that $\overline{u_i u_j}$ represents the average effect of turbulent advection on the mean flow field. Turbulent kinetic energy, for instance, is defined as $k = (\overline{u^2} + \overline{v^2} + \overline{w^2})/2$.

In Cipolla and Keith (2003) and Keith et al. (2005) details on how boundary layer thickness scale with the cylinder length are presented. Reviews of much of the early work done on wall pressure fluctuations can be found in Bull (1996) and in Snarski (1993). Early numerical simulations of axial flow were conducted by Neves and Moin (1994b,a) where they also present detailed turbulence statistics for axially aligned flow. Based on wind-tunnel experiments, Bull and Dekkers (1993) found that vortex shedding can occur for a limited range of Reynolds number for long cylinders (L/(2a))≈ 3000) at inclination angles as low as $\alpha = 1°$. They also suggest that the vortex shedding may be relevant to turbulence-generation (and thus also to noise-generation) in thick axisymmetric turbulent boundary layers. Possible vortex shedding at small inclination angles was also reported by Atta (1968). These findings have recently been partly confirmed by Direct Numerical Simulation (DNS) of near axial flow performed by Woods (2006). On the other hand, in experiments performed by Heenan and Morrison (2002a,b), no vortex shedding for inclination between $0 - 6°$ was observed. Their hypothesis is that low frequency noise is caused by streamer oscillation or buckling. Furey (2005) also cites a number of experiments which indicate that vorticial structures are shed from cylinders only for inclination angles larger than $5°$. It should be noted, however, that cross flow induced vortices at small angles can remain attached to the surface and remain within the boundary layer as illustrated in Figure 3.2. This could explain the lack of observed shedding in the studies mentioned above. This phenomenon is sometimes referred to as 'trailing vortices', see Ramberg (1983) and Thomson and Morrison (1971). In a study performed by Snarski (2004), the spectral characteristics of flow over a cylinder $L/(2a) = 23$ at different inclination angles were investigated. It was found that for $\alpha \leq 15°$ the energy spectra becomes broad-banded, and the turbulent energy content decreases. He also reports significant Reynolds number effects for small inclinations angles, and suggests that the energy spectra for high Reynolds number

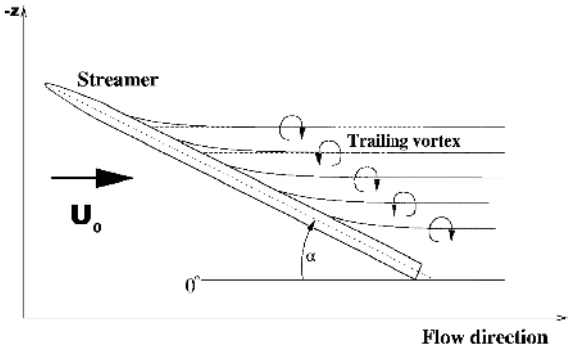

Figure 3.2: Sketch, in side view, of the flow past a yawed circular cylinder in a steady trailing vortex regime. (Positive z point downwards.) [After Thomson and Morrison (1971)].

flow might be a built up of contributions from both low frequency large scale shed vorticity and higher frequency small scale boundary layer turbulence.

3.3 Methods

The advancement in modern streamer design has almost eliminated bulge-wave interference which has been one of the most dominating sources of noise. In order to further improve streamer performance, noise sources that previously have been considered less important must now be investigated. In this section we start by describing weather and flow noise as observed in modern seismic recordings. We then look at some of the fluid mechanical properties of seismic streamers. This is used to quantify hydrostatic and some hydrodynamical sources of noise. This physical insight is valuable for any future work to improve the S/N-ratio on seismic recordings, as it provides a description of the underlying mechanisms that probably are responsible for a significant part of noise generation.

3.3.1 The distribution of noise

The distribution of noise along seismic streamers can be obtained by averaging root-mean-square (rms) noise from a number of statistically independent records. Figure 3.3 shows a typical rms-plot from a line recorded in 2.5 to 3 m waves with a modern solid streamer. The positions of the steering birds[1] are indicated by the channel-numbers. The acoustic birds[2] are not numbered but indicated by the solid vertical lines. From these plots we observe:

- For the unfiltered noise record, see top image in Figure 3.3, the average rms-noise level shows local minima near the position of each steering bird (the spiky notches that go

[1] A steering bird is a depth control device, used to keep the streamer at a predetermined depth.

[2] Acoustic birds are used to determine the position of the streamer. They are similar in size to steering birds, but do not have wings.

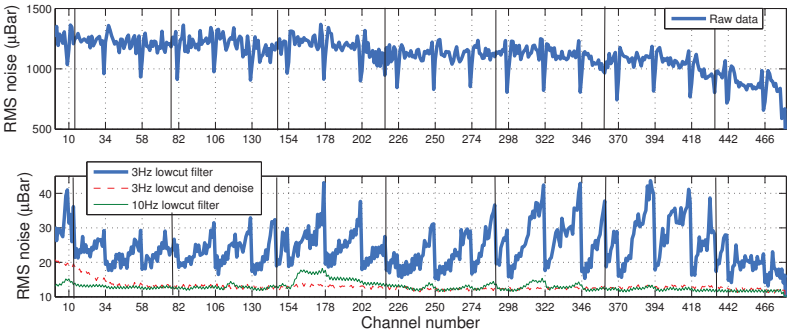

Figure 3.3: The rms-noise on a modern streamer (480 traces) recorded during a period of non-optimal conditions. Top: Raw data - using only a 3 Hz, 6 dB/Octave recording filter. Bottom: Data where low-cut filters and a time-frequency de-noising algorithm have been applied. All data are averaged over approximately 200 shot-records. The position of the channel numbers indicate bird positions, while the vertical solid lines show the position of the acoustic pods.

downwards). Note that there is a strong correlation between bird positions and the position of the spiky notches.

- When a 3 Hz low-cut filter is applied, see the lower image in Figure 3.3, the average rms-level gradually increases towards each bird, and then abruptly falls off downstream the bird. See the thick line The average rms noise level for surveys acquired during bad weather condition, and after applying a 3 Hz low cut filter, is typically above $20\ \mu Bar$. See lower image in Figure 3.3. In calm seas the same filter settings would typically give in a rms-noise level around $5\ \mu Bar$.

- Figure 3.3 shows that the energy content in near zero-Hz band is several orders of magnitude larger than all other frequency bands. These low frequencies (0-2 Hz) contain little useful seismic information and are normally removed by applying a low-cut filter.

- Above 10 Hz the averaged distribution of noise (solid thin line) seen in the lower image in Figure 3.3 is almost constant.

The top image in Figure 3.4 shows power spectrum estimates from two noise gathers acquired by the same vessel. The thick line shows the spectrum acquired offshore in 1.5m swells. The thin line shows data acquired inshore in a quiet fjord a few hours later. Notice the difference in amplitude in the 0-10(15)Hz range. This is typical of swell-noise. It has large amplitudes at relative low frequencies. The lower image in Figure 3.4 shows how the power spectrum estimate changes when the vessel is turning, and thus getting significant cross flow over the streamer. The turn was preformed during calm weather conditions inside a fjord. No abnormal tugging or movement of the streamer could be observed during this turn. However, the rms-noise level on the streamer increased significantly. Especially on the front channels, coinciding with the largest angle between the streamer and the towing direction. We also note that the frequency content of the noise acquired during the turn appears similar to swell noise. (Large

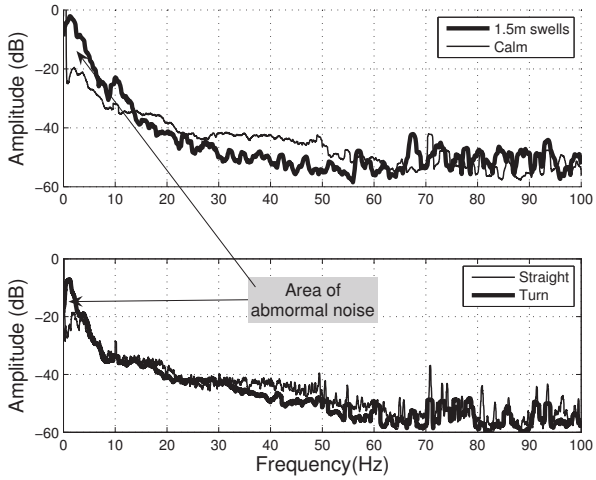

Figure 3.4: Upper panel: Power spectrum estimates from noise gathers acquired in a calm fjord, and in 1.5 m swells. Lower panel: Spectral estimates from noise gathers acquired in a calm fjord going straight and while turning. The spectral estimates were obtained by using a multi-taper method Thomson (1982).

amplitudes at low frequencies.) In all the data in Figure 3.4, the vessel speed was 4.5 kn, and the streamer depth was 5 meters.

Another interesting observation made during this test was that when the turning radius was widened enough, in this case $r \geq 900$m on a 300 m long test streamer, then no abnormal frequencies nor any increase in rms-level during the turn was observed.

The shape of the power spectra change little with increasing vessel velocity. The only observable difference is in the average rms level. Figure 3.5(a) shows how the average rms level develop on two different vessels as the velocity is increased, while Figure 3.5(b) shows average RMS over the 10 last noise records for one of the vessels. When we compare the near and the far offset traces, there is no trend in this data to indicate that the near traces are more affected by propeller or vessel noise. It is therefore reasonable to assume that the increase in noise level with vessel velocity is mainly caused by flow noise. By extrapolating from the same figure we also observe that the background noise level in good weather only seems to be $1 - 2\ \mu Bar$.

3.3.2 Fluid mechanical properties of streamers

The analysis presented in this section is to a some extent only valid for equilibrium boundary layers. In practice, this means that the streamer needs to be perfectly aligned with the mean flow, and that the conditions needs to remain constant for the results to be accurate. The analysis provides a quantitative picture that can be used as a rough guide to how real flows around seismic streamers will behave.

The cylindrical geometry of seismic streamers will influence the flow properties in the boundary

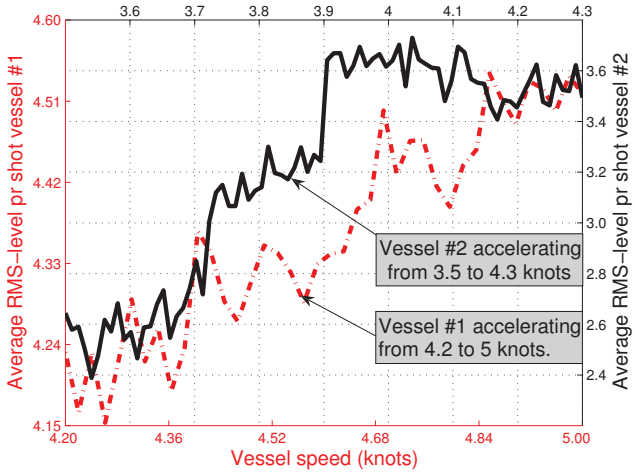

(a)

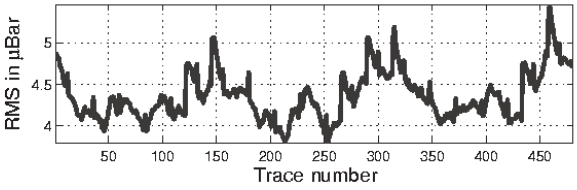

(b)

Figure 3.5: a): Average rms-noise level as a function of vessels speed. These recordings were done during fairly calm conditions. A 3 Hz low-cut filter was applied to the data before the noise levels were computed. b): Rms-noise level for each channel averaged from 10 records while the vessel speed was 5 kn.

layer. This can be understood by comparing the ratio of turbulent boundary layer flow volume to the bounding surface area. For a flat plate we have

$$\frac{\text{Volume}}{\text{Surface}} = \frac{LW\delta}{LW} = \delta, \tag{3.1}$$

where L and W denote the length and width of the turbulent boundary layer, respectively. For a cylindrical geometry

$$\frac{\text{Volume}}{\text{Surface}} = \frac{\pi L((\delta + a)^2 - a^2)}{2\pi aL} = \delta\big(1 + \frac{\delta}{2a}\big). \tag{3.2}$$

Assuming that the ability of the turbulence to extract energy from the mean flow is similar, the larger volume-to-surface-ratio for a cylinder might indicate why the boundary layer thickness will grow slower for a cylindrical geometry than for the flat plate equivalent. For a cylindrical geometry the turbulent structures are not bounded in the span-wise direction. The result of this has been summed up in Heenan and Morrison (2002a), where they found that for a cylindrical geometry, $\overline{u_i u_j}$ and τ_w will be larger close to the surface, and smaller further away from the surface compared to the flat plate case. This will be seen to be important for flow noise generation through Equations 3.14 and 3.15.

By following work done by Lueptow et al. (1985) it is possible to analytically quantify the magnitude of the Reynolds stresses. We start with an equation that is valid close to the wall for an axisymmetric boundary layer

$$(r + a)\tau = a\tau_w, \tag{3.3}$$

where τ_w is the shear stress at the wall, and τ is the total shear stress. Except right at the wall, $y = 0$, where viscous effects are important, the Reynolds shear stress $\overline{uv}$ dominates the total shear stress. We can thus rewrite Equation(3.3) as

$$-\rho\overline{uv} = \tau_w \frac{a}{r + a} \qquad \Rightarrow \qquad \overline{uv} = -u_\tau^2 \frac{a}{r + a}. \tag{3.4}$$

Lueptow et al. (1985) provide estimates of u_τ/U_0 for axisymmetric flow based on measurements. This factor is not constant but depends both on flow velocity and boundary layer thickness. By extrapolation from Lueptows data, we get $u_\tau/U_0 \approx 0.04$. This results in the expression

$$\overline{uv}(y) \approx 0.0016U_0^2\Big(\frac{a}{r + a}\Big). \tag{3.5}$$

According to Lueptow, the approximation $\overline{|uv|} \approx 0.45\overline{|uu||vv|}$, should be valid for much of the boundary layer. By taking advantage of the engineering estimate $|uu| : |vv| : |ww| \approx 4 : 2 : 3$, the relation

$$\overline{|uu|}(y) \approx 0.084U_0\sqrt{\frac{a}{a + y}} \tag{3.6}$$

is obtained. The $\overline{|uu|}$ component of the Reynolds stress tensor is also the largest contributor to the turbulent kinetic energy, $k = \rho(\overline{uu} + \overline{vv} + \overline{ww})/2$.

The kinematic viscosity of water at temperature $T = 20°\text{C}$ is $\nu = 1.01 \cdot 10^{-6} m^2/s$. From the literature it is known that the Reynolds stresses peak at $y^+ \approx 20$. The physical distance to the

Streamer(m)	θ(cm)	δ(cm)	V_θ(m^3)	V_δ(m^3)
10	1.4	14.9	0.013	0.33
50	4.8	49.1	0.36	17.99
100	7.5	76.8	1.46	87.8
200	11.4	117.1	5.86	409.7
300	14.4	148.2	13.2	990
600	21.3	218	52.7	4362
1800	38.5	396	474	43454
6000	72.3	744	5266	514551

Table 3.1: Theoretical boundary layer parameters in the case of a perfectly axisymmetric flow.

peak stress from the streamer surface can thus be estimated by

$$y = y^+ \nu / u_\tau. \tag{3.7}$$

For $y^+ = 20$ this corresponds to $0.2\,\mathrm{cm}$. For a seismic streamer with diameter $d = 5$ cm and free-stream velocity U_0=2.5 m/s $\approx$ 5 kn, the Reynolds number $Re_d = U_0 d/\nu$ is $\approx 10^5$. Re_L based on the length of the streamer, is in the range of 10^6 to 10^9, while a Reynolds number based on boundary layer thickness Re_δ, is around 10^5 to 10^6. Re_L can also be estimated based on the measured friction drag F_D.
It is typically observed that for a 6000 m seismic streamer the difference in tension front to tail is approximately 11000 N. The average drag coefficient is thus given as

$$C_D = F_D/(\rho U_0^2 \pi a L) \approx 3.73 \cdot 10^{-3}. \tag{3.8}$$

Based on an empirical formula flat plate turbulent flow given by Schlichting (1979), we can estimate
$Re_L = 1/\left(C_D/0.074\right)^5 \approx 3.05{\cdot}10^6$, which corresponds to an effective length of 1.2-1.5 m. This can be compared with Heenan and Morrison (2002b) who argue that typical drag coefficients for streamers indicate an effective length of 2-3 m.
An estimate of momentum thickness θ can be obtained by taking advantage of the work done by Cipolla and Keith (2003). For the relevant geometry θ can be obtained by solving

$$\theta^2 + 2a\theta - aLC_D = 0 \quad \Rightarrow \quad \theta = -a \pm \sqrt{a^2 + aLC_D}. \tag{3.9}$$

By using a flat plate engineering formula given by Schlichting (1979) we can estimate the boundary layer thickness based on the momentum thickness as $\delta \approx 10\theta$. Table 3.1, which is based on Equation (3.9), provides some estimates on how θ and δ evolve along the streamer when the flow is perfectly aligned with its axis. For this estimate to be valid C_D must remain constant along the streamer. This might seem strange, but Furey (2005) present measurements that partly justifies this assumption. She also found that the growth of an axisymmetric boundary layer was not uniform with streamer length, and that for some combinations of cylinder diameter and towing speed, the boundary layer seemed to stop growing when it had reached a certain size. No attempt has been made to account for the effect of cross-flow or the presence of birds

mounted on the streamer. Equation (3.9) can be integrated to find the total volume of water in the boundary layer. Estimates of the volume V_θ and V_δ along the streamer can be found in the last tow columns in Table 3.1.
The Kolmogorov micro-scales gives a lower limit on the length, time and velocity scales found in turbulent flows. These are given as

$$\eta_\kappa = \left(\frac{\nu^3}{\epsilon}\right)^{\frac{1}{4}} = \frac{\nu}{u_\tau}, \quad \tau_\kappa = \left(\frac{\nu}{\epsilon}\right)^{\frac{1}{2}}, \quad v_\kappa = (\nu\epsilon)^{\frac{1}{4}}, \tag{3.10}$$

respectively. Based on a measured average wall shear stress τ_w of 11.67 N/m^2, it can be estimated that $\eta_\kappa \approx 1.0 \cdot 10^{-5}$m for a typical seismic streamer. The same order of magnitude number is obtained by using the relation $u_\tau \approx 0.04U_0$ between the tow speed and the friction velocity, as given in Lueptow et al. (1985). The length scale l usually denotes a typical turbulent eddy size. Mathematically it can be identified by means of a two-point velocity correlation function that can not be obtained from normal seismic data. A rough estimate of l can nevertheless be made based upon experience from similar types of turbulent flows. Perpendicular to the cable we have $l \sim \mathcal{O}(\delta)$. However, for high Reynolds number flows, recent experimental studies by Hutchins and Marusic (2007) and Monty et al. (2007) have found very long, $l \sim 20\mathcal{O}(\delta)$ features in the logarithmic region of the turbulent boundary layers.
The principle of the existence of a turbulent energy-cascade where large eddies feed smaller eddies with energy who feed even smaller eddies and so on, down to viscous dissipation, tells us that within the turbulent boundary layer, turbulent structures with all sizes from l to η_κ are present. Most of the energy is found in the larger scales of motion. From a noise generation point of view it is therefore these larger scales turbulent structures, with a diameter $d \approx l$ that are of most interest.

3.3.3 Hydrostatic pressure variability

Hydrostatic pressure variations are due to differences in water depth over the seismic streamer. In order to quantify these fluctuations both the vertical movement of the streamer and the local velocity of the surrounding water must be determined. In 2-D, the circular movement due to surface waves w of a particle at depth z in deep water is approximately given by Kundu (1977), page 202 as

$$w(x, z) = A\omega e^{-kz} \sin(kx - \omega t). \tag{3.11}$$

Here A denotes the amplitude of the surface waves, and a positive z is pointing downwards. The wave-number is $k = 2\pi/\lambda$, where λ is the wave-length, and $\omega = \sqrt{gk}$ is the angular frequency, where g is the acceleration of gravity. From Figure 3.6, generated using Equation (3.11), we observe that with A=3 m the velocity at 8 m depth can exceed 0.7 m/s.

The main frequency of a 150 m wave is around 0.1 Hz, while a wavelength of 50 m will have a frequency of around 0.3 Hz. Note that a wave height of 3 meters is small, relative to typical wavelengths of ocean swells. Equation 3.11 should therefore constitute a fair approximation.
The actual streamer movement have been determined by two different approaches. First we ran a computer simulation[3] where we subjected a streamer at 8 m depth to a system of 3 m waves.

[3]The Orcaflex simulation program was used. It is developed by Orcina and is a software package for dynamic

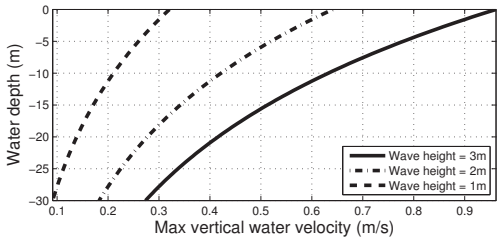

Figure 3.6: Variation of maximum water velocity with depth for three wave-heights. (From Equation 3.11.)

Realistic parameters were chosen for tension, streamer stiffness and friction, and the effect of the steering-birds was simulated by giving 1 m streamer sections a $C_{D_{cross}}$-coefficient four times larger than the rest of the cable. The result was that for a streamer towed at 4.5 kn the vertical movement of the cable was around $\pm$0.5 m. The maximum vertical streamer velocity was ± 70 cm/s, as predicted in Figure 3.6, while a more typical velocity would be around ± 20 cm/s. A 70 cm/s cross flow at 4.5 kn velocity would temporarily create a inclination angle of $\alpha \approx 17°$, while 20 cm/s results in $\alpha \approx 5°$.

A second attempt to determine the streamer motion was done by studying the receiver ghost notch in the power spectra. Consider a upward traveling seismic signal that has been reflected from the subsurface. A part of this signal will reach the sea-air interface where it is reflected with opposite polarity, and becomes a ghost. The time delay between the primary upward traveling and the downward traveling ghost in the time domain equates to a location in the power spectrum where the ghost pulse has become $180°$ out of phase with the primary pulse. At this point the two signals add destructively and produce a near zero amplitude. The frequency position of this notch is given by

$$f_{notch} = c_w/2z, \tag{3.12}$$

where c_w is the speed of sound in the water and z is the depth of the streamer. Typical values for streamer depth are 5-8 m, while the source depth is normally 3-5 m. Note that there will be a notch both at the receiver and at the source. By carefully studying power spectra it is possible to make estimates on the position of the receiver notch, and then apply Equation (3.12) to determine the streamer depth. This approach showed that the variability in depth increased front to back on a streamer, and the values were consistent with those found in the simulation. The above estimates of streamer movement also agreed well with those reported by Hite et al. (2003).

A vertical movement of the streamer in the ocean is connected to a pressure change Δp as:

$$\Delta p = \rho g \Delta h. \tag{3.13}$$

Here ρ is water density and g is gravity. A vertical movement $(\Delta h = 0.01)$m of the streamer in

analysis of offshore marine structures.

water with $\rho \approx 1000\text{kg/m}^3$ corresponds to approximately $1000\mu Bar$ in pressure change. This is a very large noise level compared to other sources of seismic noise. Ocean swells, which cause such vertical pressure change, has a frequency of, $\mathcal{O}(0.1\text{Hz})$. However, the large amplitudes can be expected to also carry significant higher order harmonics, probably up to 1-2Hz.
As a result of the vertical streamer movement it is also possible that some streamer buckling could take place. The fundamental frequency of such a string wave is, according to Parrish (2005), given by $f = v_p/2L$, where v_p is the propagation speed of the wave given by $v_p = \sqrt{F_D/\rho}$. For a typical 6000 m long streamer we have $F_{D_{front}} \approx 17000\ N$ while $F_{D_{tail}} \approx 6000\ N$. The vibration length is taken as the length between two steering-birds, typically 300 m. The fundamental frequency of a seismic streamer string wave is therefore between 0.004 Hz and 0.007 Hz. Higher order harmonics of these frequencies might also exist, but these would probably exhibit amplitudes well below those created by the direct effects from waves.

3.3.4 Dynamical pressure

When a viscous fluid flows adjacent to a solid surface, the no-slip condition at the wall and the viscous shear force between the fluid and the surface cause the relative speed of the fluid to vary from zero at the wall to the free-stream value U at some distance from the surface. At some distance downstream, this boundary layer region becomes unstable, and finally fully turbulent. The direct pressure fluctuations p at the streamer surface created by the surrounding turbulent boundary layer is mathematically governed by a Poisson equation, which can be obtained from the divergence of the Navier-Stokes equation, and assuming an infinite speed of sound. In Cartesian tensor notation, this equation reads

$$\nabla^2 p = -\rho\Big(2\frac{\partial U_i}{\partial x_j}\frac{\partial u_j}{\partial x_i} + \frac{\partial^2}{\partial x_i \partial x_j}(u_i u_j - \overline{u_i u_j})\Big). \tag{3.14}$$

Here, U denotes the mean flow velocity, while $\overline{u_i u_j}$ denotes the Reynolds stress tensor. Note that this equation depends both on the mean and the fluctuating velocities. Furthermore it is non-local, so the pressure depends on the entire flow field. In other words, a local change in the velocity field will affect not only its near-field, but may also influence the dynamics of the entire flow. Estimates of the size and distribution of the fluctuating velocities are provided by Equations 3.5 and 3.6.
Another way of describing the pressure effects from the interaction of turbulent structures with the streamer, is to use an acoustic analogy. Following Lighthill (1978), this is an effect where noise is produced by the turbulent motion within the boundary layer, and is given as a wave-equation plus an extra source term. In planar coordinates it reads

$$\Big(c^2\nabla^2 - \frac{\partial^2}{\partial t^2}\Big)\rho = -\frac{\partial^2 T_{ij}}{\partial x_i \partial x_j}, \tag{3.15}$$

where c is the speed of sound, ρ is the density perturbation. The source term $T_{ij} = \rho u_i u_j + [(p - p_0) - c^2(\rho - \rho_0]\delta_{ij}$ is responsible for the generation of acoustic pressure fluctuations (sound). According to Lighthill (1978), the noise generated by turbulence is quadrupole in nature and therefore drops off from the source as $1/r^4$, where r is the radial distance to the source. This

implies that flow noise can be difficult to detect from a remote observer, but it is not necessarily weak at the surface of an array where the Reynolds stresses peak (≈ 2 mm from the streamer surface). Another result that follows from Lighthill's theory is that the excited sound intensity varies with the speed of the free-stream velocity as U^6.

3.4 Results

Based on the observation of streamer movement and the use of Equation 3.13, it is reasonable to assume that the main source of high amplitude, low frequency (0-2 Hz) noise in recordings is hydrostatic pressure unsteadiness. Features of the noise patterns shown in Figure 3.3 can also be explained as follows:

- The large surface of the steering birds enables them to follow the slow movement in the sea that is created by the long ocean waves. This reduces the static pressure fluctuations on the streamer close to the birds. We observe this as the minimum values in the top image in Figure 3.3.
- For frequencies above 2-3 Hz we observe noise peaks at the birds, see Figure 3.3. This noise could be mechanical in the form of vibrations and movement transferred from the bird to the streamer when the bird is active. It is also possible that some bird noise is caused by interaction between the bird and the turbulent boundary layer surrounding the streamer. Bird noise can typically be observed as large amplitudes with frequencies around 5 Hz.
- The drop in average noise level towards the end of the streamer can be explained by the decrease in tension with downstream distance. Near the head of the streamer high tension will make the streamer able to resist the fluid dynamical force from swell-motion. This results in significant cross flow, and will thus cause pressure fluctuations that appears as very low frequency (≤ 2 Hz) noise. Towards the tail, the streamer tension is lower, and the streamer is more likely to follow the motion of the sea. This means less cross flow, less pressure change, and therefore also a reduced level of low frequency noise.

3.5 Discussion

It is indeed difficult to clearly separate the contribution from the various sources of noise under rough weather conditions. There are several viable candidates (for instance mechanical properties, engine/propeller noise, turbulence conditions, and free-surface effects) which contributes to the overall noise picture.

Figure 3.7 illustrates the improvements on modern streamers compared to older streamers. It was created by using a multi-taper method to obtain estimates of the power spectrum for all channels on a streamer from a single shot record. The top image from a modern streamer, shows noise data from a line obtained with around $15 - 20$ μBar rms-noise level after a 3 Hz low-cut filter. The bottom image was obtained on a fluid streamer where the rms-noise level was around 15 μBar with the same filter. We observe that the solid streamer has less variability in noise

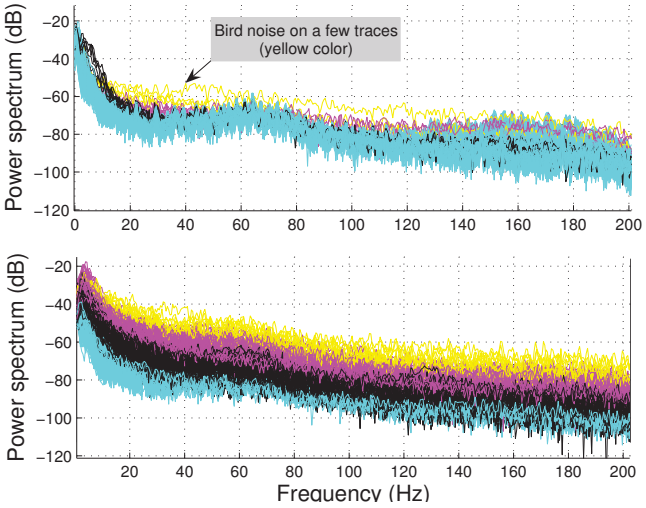

Figure 3.7: Power spectral estimates from 480 traces on: Top: a modern solid streamer. Bottom: an older fluid filled streamer. The spectra were obtained by use of Thomson's multi-taper method, Thomson (1982).

levels compared to the fluid streamer. On the solid streamer, a few traces stand out in yellow. They are all situated close to the position of a steering bird. It was not possible to observe any tugging noise in the solid streamer data. Both the front and the back channels have a similar noise-level as the rest of the cable. This indicates that mechanical or vessel/propeller noise only has a limited influence on such a cable. The noise recorded on fluid filled streamers is different. In this data we observe that some of the front channels stand out with a high noise level. In addition one can often observe a number of nearby traces that are affected by 'swell-noise'.
This general difference in noise characteristics must be due to differences in engineering design. The design changes have however not affected the fluid dynamical properties of the streamer. As the influence of mechanical, tugging/strumming and swell noise has decreased from fluid to solid streamers, it is clear that the fluid dynamical effects must account for relatively more of the remaining noise observed on modern streamers. There is also an added complexity in Figure 3.4. This figure shows that data acquired in waves or when there are cross flow over the cable, have energetic abnormal frequencies up to around 10 Hz. Such high frequencies cannot be explained by changes in the hydrostatic pressure created by swell-motion. Figure 3.8 gives us a clue as to what is going on in this case. It was produced by correlating unfiltered seismic noise from solid streamers, with itself after a 3 Hz low-cut filter was applied. Similar correlation plots have been made on a number of lines (not shown here) that were recorded in non-optimal weather. They consistently show a similar pattern as in Figure 3.8. It is clear that the noise beyond 3 Hz lags behind the noise from the DC component by around one trace, corresponding to 12.5 m. The correlation is also asymmetrical. This means that most of the noise observed in the above 1-2 Hz range can not be the result of internal waves in the streamers, streamer string

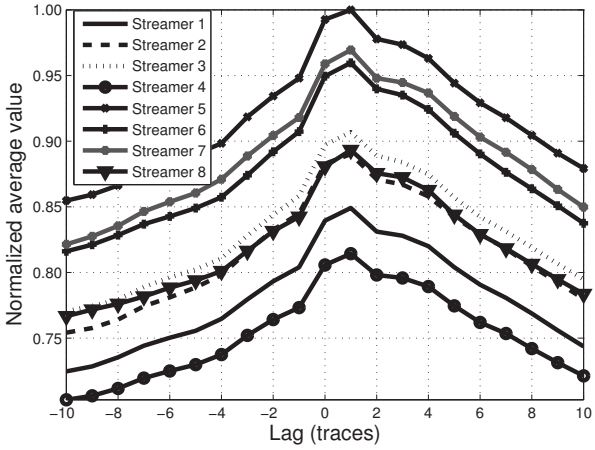

Figure 3.8: Estimated correlation function of raw seismic noise with a 3 Hz low cut version of itself. This data is averaged from around 200 gathers.

waves or streamer oscillations. Such mechanisms would on average produce a symmetric noise pattern. Based on this, and Figure 3.4, it is reasonable to argue that a significant part (maybe around 30-70 percent) of the elevated noise level we observe above 1-2 Hz on modern streamers during non-optimal weather, must be related to motion in the turbulent boundary layer. This also means that 'traditional' sources of noise, like tugging, bird-noise, background noise, noise from the previous shot, electrical noise, and other mechanical noise in total probably make up similar amount.

A saw-tooth pattern, like the one seen in Figure 3.3, becomes visible if we average over a large number of records during non-optimal weather conditions. Currently, we do not have any conclusive explanation for this behavior, but can only speculate that the boundary layer is growing in size and intensity along the streamer. On average this causes an increase in the noise level the further along the streamer we measure. The presence of steering birds interacts with the turbulent boundary layer, temporally resulting in a sharp drop in the average noise level. This is observed to result in a saw-tooth pattern of the average rms-noise-level. Although reasonable, this hypothesis does not provide a quantitative explanation of this phenomenon. It is also possible that vorticial structures shed from the wings of the steering birds might play a role in the turbulent boundary layer.

3.5.1 Cross-flow

Unlike vertical cross flow which oscillates with the wave motion, cross flow from tides or ocean currents tend to be fairly uniform in time and have significant velocities. From Heenan and Morrison (2002b) we have seen that small inclination angles can lead to a reduction in amplitudes for a large part of the spectra. For larger feathering angles we normally observe elevated energy over a broad frequency range. In a number of lines, not shown here, that were recorded with large

feathering angles due to cross flow, it was not possible to observe any lag comparable to the type observed Figure 3.8. A cross flow of 0.5 m/s on a streamer being towed at 4.5 kn, would generate a inclination angle of $12.5°$. Snarski (2004) reported that the flow noise level on a cylinder at $\alpha \geq 15°$ to be elevated over a broad frequency range compared to near axial flow. It is unclear why a small angle of inclination $\alpha \leq 6°$ results in a reduction in amplitudes, while a somewhat larger angle results in an increase in amplitudes for the same frequencies. A possible explanation is that a small cross flow will induce asymmetry in the turbulent boundary layer, effectively making it more difficult for turbulent structures to couple around the streamer, and thereby affecting the near wall Reynolds stresses. For large cross flow there might be another flow regime that takes over with trailing vortices, and possible even continuous vortex shedding.

3.6 Methodes to reduce seismic noise

From a physical point of view, and without changing the hardware, there are basically three ways of reducing the amount of noise in seismic recordings. The first is to reduce the towing velocity. As illustrated in Figure 3.5(a), by going from 5 to 3 kn, the amount of flow noise will probably be reduced by around $2\ \mu Bar$. The cost would however be prohibiting as it would almost double the amount of time used to acquire a survey. Besides, a $2\ \mu Bar$ reduction in flow noise is not significant when the general noise level in a situation with significant swells are $30 - 40\ \mu Bar$, and and the acceptable noise level is below $15\ \mu Bar$. There is also a practical lower limit on how slow streamers can be towed without loosing control. This lower limit depends on the weather conditions and streamer balancing, but in practice it is difficult to tow slower than 2.5 to 3 kn. The second option is to tow the streamers deeper to reduce the influence from waves and currents. Unfortunately one then has to tackle the implication of Equation 3.12, which describes at what frequency the destructive interference from the air-sea reflection will take place. A deeper tow will move this frequency notch into a frequency range where there also is a lot of seismic data. This represents a significant challenge.
The third and last solution is to apply signal processing to reduce the influence of noise. A large number of de-noising techniques exist and are in use within the seismic industry. We have found that a time-frequency de-noising approach is well suited to attenuate the effects of weather related noise in seismic data. Physically time-frequency de-noising is appealing because it specifically targets high-amplitude noise at specific frequencies. Such high amplitude band-limited noise is precisely the footprint left behind by swell-noise. A detailed descriptions of a time-frequency algorithm can be found in Elboth et al. (2008). Variants of the algorithm are also discussed by Bekara et al. (2008) and Abma et al. (2007).

3.7 Conclusions

This article describes some of the noise generation mechanisms that is believed to affect towed seismic streamers. By combining fluid mechanical insight and analysis of seismic noise records it is clear that a significant amount of noise observed is generated in the turbulent boundary layer surrounding seismic streamers. This noise primarily originates from two different sources. First there is the low frequency hydrostatic pressure variation, and secondly there is the dynamical

flow noise. The dynamical flow noise appears to pass a threshold when the angle between the flow direction and the streamer exceeds around $6 - 15°$. During operations it should therefore be a goal to keep the tow angle below this critical value.

Previously, elevated noise levels have been explained by bulge-waves, tugging, strumming, vibrations and electrical interference. Engineering improvements in modern equipment have greatly reduced the influence of these sources of noise. The work towards these improvements has not addressed the turbulent streamer boundary layer which inevitably will create unwanted noise. As a direct consequence we see that in order to reduce the recorded noise levels further, changes to the physical design of seismic streamers alongside with improved signal processing algorithms need to be addressed. Engineering optimizations to improve the transfer of signal between the streamer hose, the fill materials and the hydrophones can probably improve the S/N-ratio on future streamers. However, more radical design changes might also have to be considered to really tackle the influence of flow noise.

Chapter 4

Investigation of flow and flow noise around a seismic streamer cable

Thomas Elboth <thomae@math.uio.no>
Fugro Geoteam AS, Hoffsveien 1c, P.O.Box 490 Skøyen N-0213 Oslo, Norway
Mechanics Division, Department of Mathematics, University of Oslo, Norway
Difrik Lilja <d.lilja@fugro.no>
Fugro Geoteam AS, Hoffsveien 1c, P.O.Box 490 Skøyen N-0213 Oslo, Norway
Bjørn Anders Pettersson Reif <Bjorn.Reif@ffi.no>
Norwegian Defense Research Establishment (FFI), P.O.Box 25 2027 Kjeller, Norway
Mechanics Division, Department of Mathematics, University of Oslo, Norway
Øyvind Andreassen <Oyvind.Andreassen@ffi.no>
Norwegian Defense Research Establishment (FFI), P.O.Box 25 2027 Kjeller, Norway

Article originally published as:
T. Elboth, D.Lilja, B. A. Pettersson Reif and Ø. Andreassen: Investigation of flow and flow noise around a seismic streamer cable, Geophysics XXX, in press (2010)

Abstract

In marine seismic explorations, flow noise from the turbulent boundary layer that forms around a streamer cable due to its relative motion through water significantly affects the quality of collected data. Understanding this noise generation mechanism is valuable for the development of future seismic streamer cables.
In this study, we qualitatively characterize the area of turbulent flow surrounding a seismic streamer cable, and relate this characteristic to the statistics of the measured noise signal. The main finding is that the boundary layer thickness around a seismic streamer appears to be around $25\,\mathrm{cm}$ in an ocean environment. This is significantly larger than the 2.5 to $5\,\mathrm{cm}$ that has been reported in the literatures from laboratory experiments. We attribute this discrepancy to the unsteadiness of the ocean environment. Estimations of the spatial extent of the recorded boundary layer noise indicate that the "optimal" hydrophone separation needs to be about $0.5\,\mathrm{m}$ in order for the noise to be uncorrelated. The SNR (signal-to-noise ratio) on streamer cables would

therefore be improved if hydrophones were placed more densely than the current industry practice of about $1\,\mathrm{m}$.

4.1 Nomenclature

TBL	=	Turbulent boundary layer
δ_{99}	=	TBL thickness, $u(y = \delta_{99}) = 0.99U_0$ (m)
d	=	Streamer diameter (m)
α	=	Streamer incidence angle (degree)
U_0	=	Sow speed or free-stream velocity (m/s)
y	=	Distance from the cable surface (m)
L	=	Streamer length (m)
Λ	=	Integral length scale (m)
ρ	=	Fluid density (kg/m^3)
ν	=	Kinematic viscosity of water ($1.01 \cdot 10^{-6}\mathrm{m}^2/\mathrm{s}$)
Re	=	Reynolds number; $Re_L = UL/\nu$; $Re_\delta = U\delta/\nu$
C_{xy}	=	Correlation coefficient of timeseries x and y

4.2 Introduction

The word seismology is often associated with earthquakes. However, the tightly related term "seismic" comprises a valuable technology used extensively by the oil and gas industry in its exploration, development, and reservoir management operations. Marine seismic exploration is normally done by towing long flexible streamer cables in the ocean. These cables are populated with pressure sensors (hydrophones), to acquire information about the subsurface geology. Pressure recordings are made from subsurface reflections of energy arising from a pressure source (air guns).

Various factors add complexity to streamer cable operations. Examples are wave motion from surface waves and currents that cause pressure fluctuations and rattling of the streamer. Other factors are tugging as swells abruptly force the towing vessel to different towing speeds, the presence of seismic equipment such as module cans and depth controllers along the streamer, as well as biological related flow phenomena, e.g., with barnacle growth. We also mention the wake of the towing vessel and ambient turbulence that often is present in the ocean.

All of these uncontrolled conditions of the ocean operating environment will result in elevated levels of noise and make it difficult to acquire data with sufficient quality. Different types of ocean ambient noise such as seismic interference, noise from oceanic traffic, and noise from marine creatures also affect seismic data. These types of noise will not be addressed in any detail in this paper. However, it should be recognized that they often contribute significantly to the total noise level.

As the ratio of inertial to viscous fluid forces, known as the Reynolds number, becomes large, a statistically axisymmetric turbulent boundary layer (TBL) is formed around a streamer cable. In fluid mechanics the TBL refers to a thickness beyond which the velocity is essen-

tially the free-stream velocity U_0[1]. This is customarily defined as the distance from a surface or wall to the point where the time-averaged velocity is $u(y = 0.99U_0)$. This is often denoted δ_{99}. Note that in an ocean environment the free-stream U_0 might contain ambient turbulence, characterized by low intensities and large scales. It differs from the more intense small-scale TBL formed by the relative motion between the cable surface and the surrounding water.
Apart from the recent work by Cipolla and Keith (2008) little or no previous work has dealt with the turbulent flow around sea-towed streamer cables. Industrial flows are significantly more complex than what is normally experienced in a laboratory environment, or what is simulated on computers. In the present work we seek insight into the TBL that surrounds the streamer cables in an ocean environment. Visualizations of the boundary layer based on a dye release experiment,along with noise recordings are presented and analyzed. In addition, we will consider the placement and density of hydrophones inside the streamer cable in an effort to determine the optimal configuration in order to obtain the best possible signal-to-noise ratio (SNR).

4.2.1 Previous works

The flow past a circular cylinder is a frequently studied problem in fluid mechanics. Unfortunately, most of the work performed has been on steady flow normal to the cylinder axis. Towed streamers are typically aligned in an angle $|\alpha| \leq 15°$ with the flow, and the available literature for such alignments is more limited. The flow on axially symmetric cylinders having $\alpha = 0°$, was studied by Willmarth and Yang (1970), Denli and Landweber (1979), and Willmarth et al. (1976). They investigated wall pressure fluctuations in conjunction with the mean velocity profiles. Furthermore, Willmarth and Sharma (1984) and Snarski and Lueptow (1995) also performed similar studies in whuch turbulent flow properties were investigated. In the latter study, two different groups of fluctuations in the TBL surrounding a cylinder were identified. The first was low-frequency high-energy fluctuations originating from the outer parts of the boundary layer. The second was in the form of small-scale high-frequency disturbances related to the so-called TBL burst-sweep cycle. Based on measurements, Lueptow et al. (1985) and Furey (2005) provided statistics of the distribution of the Reynolds stresses within the TBL at $\alpha = 0°$. In Cipolla and Keith (2003) and Keith et al. (2005) details about how the boundary layer thickness scale with the streamer length were presented. Recent work by Keith et al. (2008) also provided measurements on the boundary layer thickness on a long cylinder in a water-tank. In this study, they report a thicker boundary layer compared to boundary layers developed in wind tunnels, water tunnels, or pipe flows. Examples of such measurements and simulations are the work by Willmarth et al. (1976) and Tutty (2008a), who indicate a TBL thickness for a seismic cable in the range of 2.5 to $5.0\,\mathrm{cm}$.
Neves and Moin (1994a,b) conducted numerical simulations of axial flow and presented detailed turbulence statistics.

Lueptow et al. (1985), Heenan and Morrison (2002a), and a number of other researchers, have shown that even small misalignments of the axis of the cylinder relative to the mean towing direction will cause asymmetry of the boundary layer. As a result the fluctuating wall pressure levels around the cylinder are significantly modified.

[1] U_0 is here measured using the cable as the reference system.

Based on water-tank experiments, Bull and Dekkers (1993) observed that vortex shedding might occur for a limited range of Reynolds number for long cylinders (with the length to diameter ratio $L/d \approx 3000$) at inclination angles as low as $\alpha = 1°$. They also suggested that the vortex shedding might be relevant to turbulence-generation (and thus also to noise-generation) in thick axisymmetric TBLs. On the other hand, in wind tunnel experiments performed by Heenan and Morrison (2002a,b), no vortex shedding was observed for inclination between 0-$6°$. Their hypothesis was that low-frequency noise was caused by streamer cable oscillation or buckling. However, their experiment was performed on a rather short cylinder (small L/d ratio), which seems to suggest that the boundary layer, might not have had time to develop sufficiently for shedding to occur. It should be noted, that cross-flow induced vortices at small angles could remain attached to the surface and remain within the boundary layer. This phenomenon is sometimes referred to as 'trailing vortices', see e.g., Ramberg (1983) and Thomson and Morrison (1971). The spectral characteristics of flow over a cylinder $L/d = 23$ at different inclination angles were investigated by Snarski (2004). He reported significant Reynolds number effects for small inclination angles, and suggested that the energy spectra for high Reynolds number flow might be built up of contributions from both low-frequency large-scale shed vorticity and higher frequency small-scale boundary layer turbulence.

From a geophysical standpoint, investigation to identify sources of noise on streamer cables was reported by Schoenberger and Mifsud (1974), and by Fulton (1985). Since then, a significant amount of effort within the seismic industry has focused on improving streamer system technology to reduce the effects of many of the identified sources of noise. Both Peacock et al. (1983), Bjelland (1993), and Dowling (1998) contributed to the understanding of noise generation mechanisms related to fluid-filled streamer cables. The primary mechanism was identified to be longitudinal bulge-wave propagation inside the cable that created low-frequency noise. Brink and Spackman (2004) and Dowle (2006) showed that modern foam-filled streamer cables are less sensitive to such internal bulge-waves. Important recent contribution to the understanding of flow-noise on streamer cables are the works by Knight (1996) and Cipolla and Keith (2008).
As a result of design improvements, it can be concluded that the relative importance of flow-noise compared to other types of noise has increased, c.f. Elboth et al. (2009b). To further reduce the level of recorded noise during seismic acquisition, the influence of flow-noise needs to be addressed.

4.3 Experiment description

This section provides a description of the experimental setup and the equipment used, as well as some background theory. The objective is to qualitatively characterize the main fluid structures surrounding a streamer cable, and to relate these characteristics to the measured seismic noise signals.
The experiment was conducted in a Norwegian fjord in September 2008. There was very little wind during the experiment, and no currents were observed. Boat traffic in the area was light, and only occasionally did other vessels come within $5\,\mathrm{km}$ of our position. The water depth in

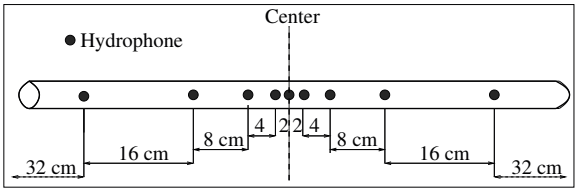

Figure 4.1: Sketch of the hydrophone distribution of the purpose built streamer.

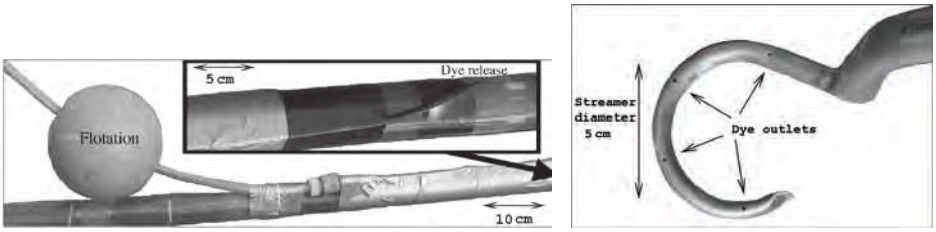

(a) (b)

Figure 4.2: Image a): The single hole outlet arrangement. A slight bend towards the nozzle is imposed to release the dye in an area where we hope there are minimal flow interactions with the arrangement (c.f., the zoomed inset). Image b): The 4-hole nozzle outlet, which was hooked onto the streamer cable.

the area varied between 100 and $200\,\mathrm{m}$.

The experiment was conduced by releasing an environmentally friendly colored dye into the boundary layer surrounding a streamer cable in the sea. This dye revealed turbulent flow structures, which were captured by an underwater camera. Complementary pressure field recordings were conducted with a purpose-built streamer cable with varying hydrophones distribution as depicted in Figure 4.1. No air gun or seismic source was used during the data acquisition. The noise measurements were used to compute correlations between hydrophones with the aim of determining how far apart hydrophones had to be separated in order to only record uncorrelated noise. This can be related to the spatial and temporal extent of the noise producing eddies in the TBL. The recording system utilized a $5\,\mathrm{Hz}$ $6\,\mathrm{db/octave}$ low-pass filter at $1\,\mathrm{ms}$ sampling rate.

4.3.1 Video recording

A workboat with a dye container and a camera was towed over the seismic streamer cable approximately $200\,\mathrm{m}$ behind the seismic vessel. At this distance the influence from the vessels wake and propellers was presumed to be minor. During the filming, the towing speed was $4\,\mathrm{knots}$ and the cable was kept at a depth between 1 and $2\,\mathrm{m}$. Unlike more conventional acquisition depths from 5 to $7\,\mathrm{m}$ our depths provided more daylight, with improved dye contrast. It was not expected that this depth discrepancy would be of any importance, as the most signifi-

cant depth-depending issue for realism, the sea state[2], was calm. A steering pole arrangement for the camera was placed on the workboat side. From the workboat a hose was connected to tubes with different nozzles in order to inject dye. The tubes were attached onto the streamer cable for approximately $0.8\,\mathrm{m}$ to reduce the interaction between the connecting hose and the flow close to the dye outlet. When visually inspected, the thin hose going to the surface did not seem to influence the TBL surrounding the streamer. A floating device, see Figure 4.2(a), raised the hose to the surface. The floating device did not give any lift on the streamer.
Three different nozzles were used. Figure 4.2(a) depicts the single-hole outlet arrangement. The three-hole outlet ejected dye along three different places downstream in an interval of approximately $5\,\mathrm{mm}$ while the four-hole outlet, seen in in Figure 4.2(b), had the outlet holes in the same lateral position but distributed around the streamer periphery. Images of the turbulent flow around the seismic streamer cable can be seen in the images in Figure 4.3.

4.3.2 Theory

Seismic data contain both noise and signal. A seismic trace is produced by summing the contribution from neighboring hydrophones. It is normal to assume that on neighboring hydrophones, the noise is random and uncorrelated, whereas the signal is correlated. When this assumption holds, the SNR of a trace behaves as

$$\mathrm{SNR}(\mathrm{n}) \sim \mathrm{SNR}(1) \cdot \sqrt{\mathrm{n}}, \tag{4.1}$$

where n is the number of hydrophones. This implies that the SNR improves as the number of hydrophones increases to a limit. Not all seismic noise is random and uncorrelated. Seismic interference can for example be correlated over an entire cable. However, flow-noise is normally the dominating source of noise. It therefore also governs the correlation distances. The purpose of correlating the recorded noise is therefore to determine the spatial extent of flow-noise, and to use this to determine an "optimal" hydrophone separation.

Acoustic theory

By rearranging the Navier-Stokes equations, which govern the flow of viscous fluids, into an inhomogeneous wave equation, (Lighthill, 1952) explained the physics behind turbulent flow-noise generation. Later work by Ffowcs Williams and Hawkings (1969) extended this work by also incorporating the effects of surfaces. In this context, a simplification by Landau and Lifshitz (1987) will serve to illustrate an important point. Basically, the generation of acoustic fluctuations (noise) in the TBL in a medium is described by

$$\frac{1}{c_0^2}\frac{\partial^2 \tilde{p}}{\partial t^2} - \nabla^2 \tilde{p} = \rho_0 \frac{\partial^2 (v_i v_j)}{\partial x_i \partial x_j}. \tag{4.2}$$

This is a wave equation with a source term on the right-hand side. The $c_0(x_i, t)$ denotes the local speed of sound and $\tilde{p}(x_i, t)$ is acoustic pressure. The source term depends on the moment

[2] In oceanography a sea state is the general condition of the ocean surface with respect to wind waves and swell. The sea state can be in the range from 0 to 9, where 0 is perfectly calm, and 9 is wave heights above $14\,\mathrm{m}$

flux density tensor of the flow, $\rho_0 v_i v_j$, where $i, j \in \{1, 2, 3\}$, and $v_i(x_i, t)$ is the velocity in the x_i direction indicated in Figure 4.4. (Summation is implied by repeated indices). Finally, ρ_0 denotes the constant fluid density.

Equation 4.2 depends on the fluctuating velocity tensor $v_i v_j$, which is a quadrupole source (Lighthill, 1978). That implies that its intensity decays as $1/r^4$ with distance r. Consequently, flow-noise can be expected to be rather local. The largest visible noise producing eddies have a diameter similar to the boundary layer thickness. Because of the $1/r^4$ relation, this thickness could also be expected to be their approximate noise imprint.

The term "eddy", used above, alludes to an image of swirling motion around a vortex. We have not attempted to define it more precisely however, the intuitive understanding given by a mental picture will probably suffice in this context. Finally, we mention that the TBL-noise recorded by a hydrophone is not only related to the wavelength of the signal (which can be tens of meters), but also depends on the nature of the source terms. Individual hydrophones will record the high-frequency spatial variations in the TBL noise, and not only the low-frequency temporal variations.

4.4 Results

From the images in Figure 4.3, we observe vorticial structures, or eddies, that are propagated in the TBL surrounding the streamer. The diameter of these eddies varies from about $30\,\mathrm{cm}$, and according to theory, down to well below of the camera resolution. The TBL appears to have a thickness $\delta \sim \mathcal{O}(25\,\mathrm{cm})$. However, the inner part of the boundary layer (from the streamer and out approximately $1\,\mathrm{cm}$) appears to have a higher turbulence intensity compared to the outer part, which is dominated by larger eddies. A Comparison of our observed TBL thickness with what has been reported in the literature suggests that the unsteadiness of the ocean environment has enlarged the TBL. The largest eddies turn over with a velocity of the same order as the towing/free-stream velocity U_0. They can typically be observed for up to one turnover, before they break down into smaller scales. It is reasonable to assume that during one eddy turnover, an eddy will induce coherent sound pressure on a certain part of the streamer. This will occur for $t = \pi d/U_0$ s. By choosing $U_0 = 2\,\mathrm{m/s}$, a typical large eddy will have a lifespan of about $0.4\,\mathrm{s}$. This corresponds to a correlation length of $0.8\,\mathrm{m}$, which is consistent with computations presented later in this section.

The filming was done during very quiet conditions. Even so, the TBL never developed undisturbed over distances greater than $\mathcal{O}(5)\,\mathrm{m}$. This probably means that statistically, the TBL characteristics are independent of downstream position on the streamer. The visible dye in Figures 4.3(a) and 4.3(b) does not correspond to a developing boundary layer. Instead it shows a developed TBL, where the dye is mixed by the turbulent fluid flow surrounding the streamer as illustrated in Figure 4.4. Because the streamer does not remain perfectly straight, this thick region of turbulence contains the TBL itself and, superimposed on top if it, trailing vortices created in upstream positions. The dye is efficiently mixed within the turbulent region. However, at the turbulent/non-turbulent interface the mixing efficiency abruptly decreases. This interface determines the thickness of the turbulent region that surrounds the cable. It is possible that the outer parts of the boundary layer seen in the images in Figure 4.3 should be interpreted more as

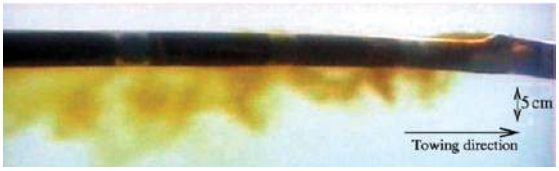

(a)

(b)

Figure 4.3: Snapshots of a seismic streamer cable in the ocean. Picture a): Cross-section view visualized by a single hole dye release. Picture b): 3-D view by a multi-hole dye release.

a wake, (Denli and Landweber, 1979) or a jet, instread of a boundary layer. The bottom image in Figure 4.4 is a sketch of the time-averaged velocity profile of the flow around a streamer cable. The actual TBL might be partly hidden within this jet or wake, and might only extend a short distance out from the streamer surface. Note that this indicates the time-averaged flow.

4.4.1 Rms-analysis

The rms (root mean square) analysis presented here is based on a number of $60\,\mathrm{s}$ records acquired during our experiment. From 10 records acquired at each velocity, the one with the lowest rms level is shown in Figure 4.5. The increase in rms level at $3.5\,\mathrm{knots}$ can probably be attributed to a small fishing vessel that passed about $2\,\mathrm{km}$ away during this particular recording. No other shipping was observed in the area during the period when the data in Figure 4.5 were acquired. Spectral estimates of the $3.5\,\mathrm{knots}$ data also show an amplitude-increase in the 100-$150\,\mathrm{Hz}$ range, which typically corresponds to propeller noise.

From Figure 4.5, we observe that an extrapolation of vessel speed to zero, indicates an ocean ambient noise level of roughly $1\,\mu\mathrm{Bar}$. The rms level for typical seismic vessel velocities is from 1.8 to $2.8\,\mu\mathrm{Bar}$. This indicates that at 4 to $5.5\,\mathrm{knots}$, ocean ambient noise makes up around 35%-55% of the overall noise during this experiment. This assumption will be refined further in the Correlation Analysis and Spectral Analysis sections, where other estimates on the relative amount of ocean ambient noise are provided. The rms-noise level seems to increase with vessel velocity below $20\,\mathrm{Hz}$. Above $20\,\mathrm{Hz}$ the rms-noise level appears to be almost constant,

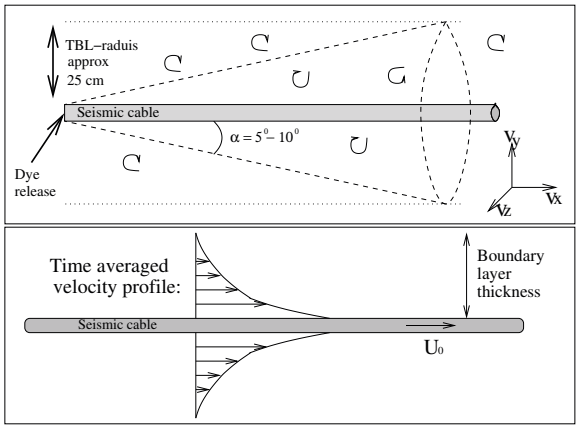

Figure 4.4: Top image: Schematic of how the dye spread in the TBL. The cone illustrates the angle with which dye is mixed by the turbulence, while the horizontal stapled lines illustrate the outer edge of the turbulent flow region surrounding the streamer. Bottom image: Conceptual sketch of the average velocity profile in the streamer TBL. This profile has a shape similar to that produced by a jet.

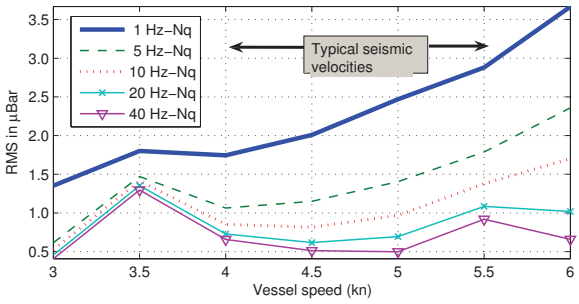

Figure 4.5: The rms noise level as a function of vessel speed and frequency. In the figure, 'Nq' denotes the Nyquist frequency, in this case $500\,\mathrm{Hz}$. To avoid losing streamer control the minimum practical vessel speed is $\approx 2.5\,\mathrm{knots}$.

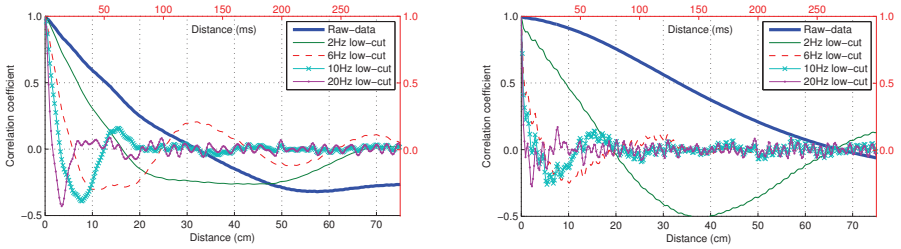

(a) (b)

Figure 4.6: Average autocorrelations of the recorded noise. Towing velocity was $5\,\mathrm{knots}$ and streamer depth was $5\,\mathrm{m}$. Image (a) and (b) was computed from records acquired at sea state 0.5 and 4, respectively. The top horizontal axis shows time, while the bottom shows distance.

not depending on vessel velocity.
According to Wenz (1962), ship noise normally peaks in the range of 50 to $100\,\mathrm{Hz}$ whereas it is almost insignificant below $10\,\mathrm{Hz}$. This indicates that the observed increase of rms level with velocity is not caused by far-field oceanic traffic. In addition, the traces close to the towing vessel did not have a higher rms noise level compared with the far traces. Most of the increase in rms level with speed was therefore most probably not caused by propeller or engine noise from the vessel itself. It is therefore reasonable to assume that the below $20\,\mathrm{Hz}$ increase in noise level with vessel velocity was due to the effects of the TBL surrounding the streamer cable.

4.4.2 Correlation analysis

The purpose of the correlation analysis is to determine an "optimal" separation between individual hydrophones.

Autocorrelations

The plots in Figure 4.6 were produced by averaging autocorrelations from noise records acquired at $5\,\mathrm{knots}$ during sea state 0.5 (calm) and sea state 4 ($1.5\,\mathrm{m}$ waves), respectively. Similar images were also obtained at other velocities. Figure 4.6(a) shows that in calm weather, raw unfiltered noise records are correlated out to around $120\,\mathrm{ms}$, corresponding to $30\,\mathrm{cm}$ by the frozen field hypothesis (Taylor, 1938). When a low-cut filter is applied, the correlation length is shortened. For example, with a $6\,\mathrm{Hz}$ low-cut filter, it is about $5\,\mathrm{cm}$.
During sea state 4, seen in Figure 4.6(b), the correlation lengths are similar. However, for the unfiltered data the correlation length is now almost $300\,\mathrm{ms}$ or $70\,\mathrm{cm}$. This can probably be explained by the presence of low-frequency swell or bulge wave noise produced by cross-flow over the streamer (Elboth et al., 2009b).
The integral length scale Λ, is defined as

$$\Lambda = \int_0^{r_c} C_{xx} dx. \tag{4.3}$$

Here r_c is where the autocorrelation coefficient C_{xx} has its first zero crossing.

Velocity	6.5m separation	175m separation
3.0 knots	48 %	3 %
3.5 knots	65 %	4 %
4.0 knots	55 %	8 %
4.5 knots	61 %	8 %
5.0 knots	65 %	10 %
5.5 knots	62 %	10 %
6.0 knots	55 %	5 %

Table 4.1: The relative amount of coherent background noise at varying velocities during our experiment. The data was acquired at sea-state 0.5.

Λ can be interpreted as collecting spatially correlated energy from 0 to r_c, to find a physical length representing the fully correlated energy within this range. This length can be seen as a weighted midpoint of energy. It is reasonable to use 2Λ separation to ensure uncorrelated energy between neighboring hydrophones, ensuring that two adjacent measurements are (nearly) uncorrelated.
By doing the integration to the data displayed in Figure 4.6 we get $2\Lambda \approx 26\,\mathrm{cm}$ and $64\,\mathrm{cm}$, respectively. When a $2\,\mathrm{Hz}$ low-cut filter to remove influence of swell noise is applied to the data in Figure 4.6(b), 2Λ is reduced to $40\,\mathrm{cm}$. Physically this autocorrelation Λ relates to the size of the largest noise producing features (eddies) in the TBL.

Ocean ambient noise

The relative amount of coherent background noise in a gather can also be estimated by the peak crosscorrelating coefficient of noise records from widely separated hydrophones. This is done in Table 4.1 for pairs of hydrophones separated by $175\,\mathrm{m}$ and $6.5\,\mathrm{m}$. For the $175\,\mathrm{m}$ separation the results reflect the amount of coherent ambient noise from distant shipping, onshore industrial activity or possibly the towing vessel itself. The $6.5\,\mathrm{m}$ separation was computed by picking out the zero-lag correlation coefficient. The strong correlations found at this distance can probably be explained by a combination of various sources of noise, such as surface wave effects, local ambient turbulence, currents (even though none were observed), bulge waves on the streamer cable, and far-field coherent noise. The coherent noise at $6.5\,\mathrm{m}$ separation can be seen as a "zero-level" for crosscorrelations of closely spaced hydrophones, and will be used in the next subsection.

Crosscorrelations

Figure 4.7 was produced by crosscorrelating traces with spatial separation $\leq 7\,\mathrm{m}$ in our special streamer cable. From each crosscorrelation we picked the correlation value found at zero-lag. The curves were then produced by fitting a spline through a large number of such correlations to show the average spatial correlation length of the noise.

We have also indicated a probable zero level, taken from Table 4.1. With this zero level flow-noise for typical seismic vessel velocities (4-$5.5\,\mathrm{knots}$) is spatially correlated up to between 0.4-$0.6\,\mathrm{m}$. The integral length-scale Λ is $\approx 0.25\,\mathrm{m}$, and a hydrophone separation of $2\Lambda \approx$

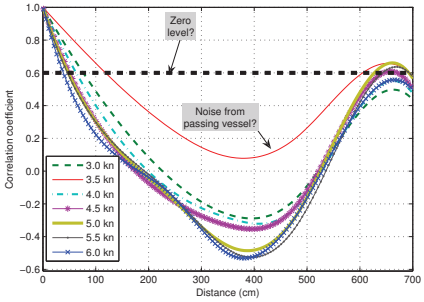

Figure 4.7: Average spatial correlation distance of noise recorded along the streamer at varying velocities. The horizontal stapled black line indicates the probable zero level.

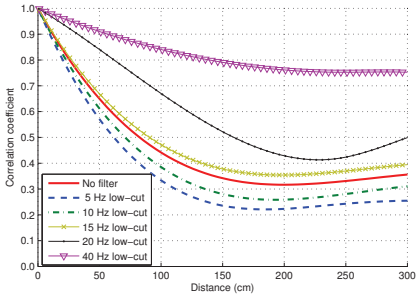

Figure 4.8: Averaged spatial correlation length of noise at different frequencies. The vessel velocity was $5.5\,\mathrm{knots}$.

$50\,\mathrm{cm}$ seems reasonable. This number is somewhat larger than the separation suggested by the autocorrelation analysis for sea-state 0.5. However, in the autocorrelation computations we relied on the Taylor (1938) frozen field hypothesis to convert between the time and space domains. No such assumptions are made here. In the above computations, uncertainty exists concerning the exact placement of the zero level. If the zero level was to be placed at 0.5 or 0.4, this would correspond to $2\Lambda \approx 60\,\mathrm{cm}$ and $2\Lambda \approx 80\,\mathrm{cm}$, respectively.
Finally, we investigated correlation length at different frequencies. Figure 4.8 was produced in the same way as Figure 4.7. However, in Figure 4.8 we also applied low-cut filters. The high-frequency content of the noise ($\geq 20\,\mathrm{Hz}$) appears to be correlated over very long distances.

Based upon field experience with seismic acquisition, and aided by the Wenz-curves (Wenz, 1962), we hypothesize that the coherent high frequency noise originates from distant shipping, industrial onshore activity or the towing vessel itself.

Figure 4.9 shows the maximum spatial crosscorrelation for a large number of traces. The thick line shows how the average correlation develops with spatial separation while the crosses show individual correlations. Recently, Tutkun et al. (2009) reported two-point correlations in high Reynolds number TBL flows of up to seven times the boundary layer thickness. In our

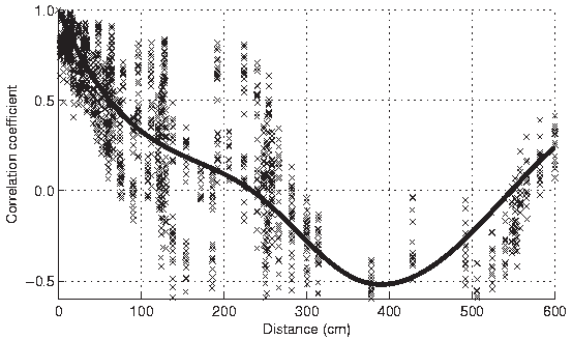

Figure 4.9: The maximum spatial crosscorrelation for a large number of traces. The line indicates the average, while each cross indicates the maximum correlation from two traces. The vessel speed was 5.5 knots.

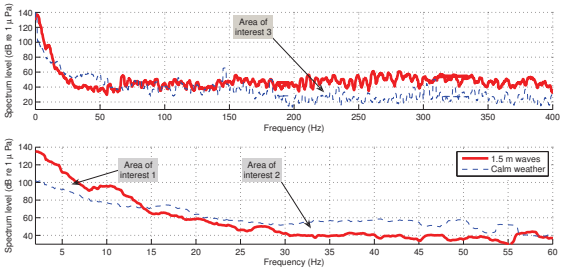

Figure 4.10: Power spectral estimates of noise records acquired on the streamer. The spectral estimates were obtained by using a multi-taper method. The bottom image is a zoom of the data in the range from 2 to 60 Hz. The steamer was at 5 m when the data were acquired, and the vessel velocity was 4.5 knots.

case, with a boundary layer of 30 cm, the maximum expected correlation length is therefore as much as 2.1 m. However, high correlations between hydrophones far apart might also be explained by far-field coherent noise or streamer bulge-wave noise.

4.4.3 Spectral analysis

In Figure 4.10, the spectral content of noise records acquired in sea state 0.5 and sea state 4 are compared.

The difference between these plots can be attributed to the influence of weather (sea state). Similar plots (not shown here) in which the frequency content of data acquired during good weather is compared with data acquired during non-optimal conditions show the same trend. Three areas of interest (1,2 and 3) where there is a difference in the noise level, have been marked in Figure 4.10, and are commented on below.

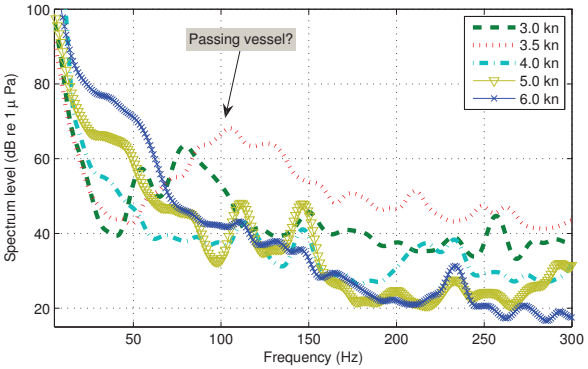

Figure 4.11: Power spectral estimates of noise records acquired on the streamer during quiet weather (sea state 0.5). The spectral estimates were obtained by using a multi-taper method. The steamer was towed $5\,\mathrm{m}$ below the surface.

1. From 0 to $15\,\mathrm{Hz}$: Elevated energy levels in the 0 to $2\,\mathrm{Hz}$ range are mainly related to hydrostatic pressure fluctuations (Elboth et al., 2009b). For the range from 2 to $15\,\mathrm{Hz}$, ocean waves induce crossflow over the streamer. According to Wenz (1962), this causes turbulent pressure fluctuations that induce noise on the hydrophones. In addition, bulge waves (Dowling, 1998) and (Bjelland, 1993) might start propagating within the cable. The combination of all of these mechanisms causes the elevated energy in the $0 - 15\,\mathrm{Hz}$ range when there are strong waves.

2. From 15-$55\,\mathrm{Hz}$: In this area there is more noise recorded during sea state 0.5, compared to sea state 4. Presently we do not have any conclusive explanations for this. One possibility is that during non-optimal weather, cross-flow and vortex shedding strip away parts of the TBL from the streamer, (Heenan and Morrison, 2002b) and (Heenan and Morrison, 2002a). Turbulent structures that normally would be responsible for the noise generation in this particular frequency range are therefore less common, and we get a reduced level of noise.

3. Above $150\,\mathrm{Hz}$: In this area there is more noise in times of non-optimal weather. According to Wenz (1962) this could be related to noise produced by bubbles near the surface by ocean waves. Other explanation could involve industrial activity or ship noise. However, the sea state 4 data were acquired offshore in an area with no visible shipping or industrial activity.

Figure 4.11 compares the frequency content of noise records acquired at different towing velocities. From this plot, we observe that below $60\,\mathrm{Hz}$, where most of the energy is found, there is an increase in noise level with vessel speed.

Comparing with reference data

Wenz (1962) provides curves with typical sound levels of ocean ambient noise. Similar data

are also available from McDonald et al. (2008). By comparing Figure 4.11 to the Wenz curves, we observe that below $20\,\mathrm{Hz}$ our curves have spectral levels from approximately 100 and down to $70\,\mathrm{dB\,re\,1}\,\mu\mathrm{Pa}$, indicating an typical "average" ocean noise environment. Above $20\,\mathrm{Hz}$ our curves roughly follow the minimum level of ocean ambient noise given by Wenz.
We also notice that below $50\,\mathrm{Hz}$, the amplitude level seems to depend on towing velocity, whereas no such dependence seems to exist above $50\,\mathrm{Hz}$.
The reference data were acquired from stationary nodes roughly $150\,\mathrm{m}$ below the surface. Such stationary nodes do not record TBL flow-noise. The increased level of noise below $20\,\mathrm{Hz}$ in Figure 4.11, compared to the minimum level indicated by Wenz, is therefore most likely due to flow-noise in the TBL of the streamer cable. Furthermore, the rms-level above 10 to $20\,\mathrm{Hz}$ should represent the overall rms-level for a stationary streamer cable. From Figure 4.5, we find that this rms-level is just below $1\,\mu\mathrm{Bar}$. This indicates that for the present survey, about half the overall rms-noise level is ambient of far-field noise, while the remaining probably is produced in the TBL of the streamer.

4.5 Conclusion

This paper describes an experiment conducted to study flow-noise along a seismic streamer cable. By releasing dye into the boundary layer we have obtained visual impressions of turbulent flow features. Complementary noise records were acquired from hydrophones placed inside the streamer cable. At typical seismic acquisition velocities, a significant part of the overall record is flow-noise that is produced in the streamer TBL. To improve the overall SNR the amount of flow-noise needs to be reduced.
A specially designed seismic cable with varying hydrophone separation distance was used to measure the correlation length of unfiltered flow-noise. The correlation length is strongly varying, from about $15\,\mathrm{cm}$ and all the way up to at least $5\,\mathrm{m}$. However, on average, hydrophones that are placed a $0.5\,\mathrm{m}$ apart record uncorrelated noise. We believe this is an optimal hydrophone separation. Most streamers today have between four and eight hydrophones per $12.5\,\mathrm{m}$ group. It is clear that in a $12.5\,\mathrm{m}$ group the signal-to-flownoise ratio could be significantly improved if the number of hydrophones was increased to 12 or even 24. Such an increase should be considered for future streamer designs. Images reveal that a streamer cable TBL has a typical thickness of 25-30 cm. This is almost an order of magnitude larger than what has been reported in the literature based upon controlled laboratory experiments and simulations. This difference can probably be attributed to the unsteadiness of an ocean environment compared to a controlled laboratory environment. In addition, the increased length of a real seismic cable, compared to what has been practical in laboratories or computer simulations, might play a role. We also note that a $\delta \sim \mathcal{O}(25\,\mathrm{cm})$ boundary layer thickness and a corresponding eddy size fit well with the obseved correlation lengths when seen in light of Lighthill's theory for the propagation of acoustic pressure from a turbulent source.

Chapter 5

Flow noise simulation around a cylinder

Thomas Elboth <thomae@math.uio.no>
Fugro Geoteam AS, Hoffsveien 1c, P.O.Box 490 Skøyen N-0213 Oslo, Norway
Mechanics Division, Department of Mathematics, University of Oslo, Norway
Carl Erik Wasberg <cew@ffi.no>
Norwegian Defense Research Establishment (FFI), P.O.Box 25 2027 Kjeller, Norway
Anders Helgeland <ahe@ffi.no>
Norwegian Defense Research Establishment (FFI), P.O.Box 25 2027 Kjeller, Norway
Øyvind Andreassen <Oyvind.Andreassen@ffi.no>
Norwegian Defense Research Establishment (FFI), P.O.Box 25 2027 Kjeller, Norway
Bjørn Anders Pettersson Reif <Bjorn.Reif@ffi.no>
Norwegian Defense Research Establishment (FFI), P.O.Box 25 2027 Kjeller, Norway
Mechanics Division, Department of Mathematics, University of Oslo, Norway

Conference proceeding originally published as:
T. Elboth, C. E. Wasberg, A. Helgeland, Ø. Andreassen, and B. A. Pettersson Reif: Flow noise simulations around a cylinder, Fifth national conference on Computational Mechanics (MekIT'09), (2009)

abstract

This work investigates flow noise from a turbulent boundary layer around an axi-symmetric cylinder. This is motivated by a problem faced by the oil and gas industry, where flow noise often limits the sensitivity and range of hydrophone arrays used for marine seismic exploration. We use a Direct Numerical Simulation (DNS) of fully developed turbulent channel flow, with Reynolds number $Re_\tau = 180$ as input to our calculations. From this DNS an acoustic analogy is used to obtain the pressure fluctuations (self-noise) from the interaction of turbulent flow structures. This self-noise is then propagated with a wave-equation to study the radiated sound field from a turbulent boundary layer in space and time. The computational domain is truncated by use of the Perfectly Matched Layer (PML) absorbing boundary condition. We find that the streamwise correlation of acoustic pressure along the cylinder is approximately $5\,\mathrm{cm}$. In the spanwise direction, the median integral length-scale is 66°, but occasional coherence up to the

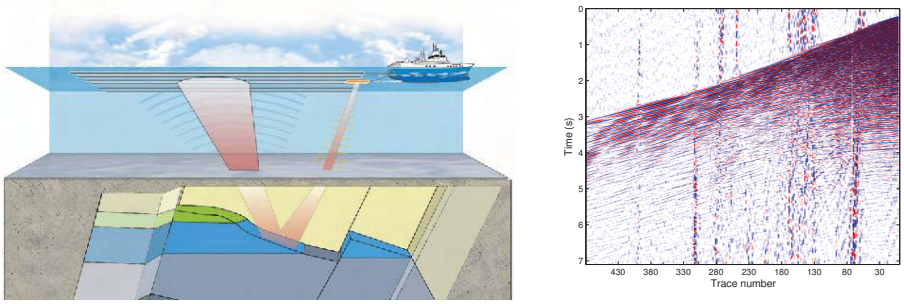

(a) (b)

Figure 5.1: Image a): Schematic of a vessel carrying out geophysical exploration. Image b): A typical marine seismic shot gather. Horizontally it covers 6 km, while vertically it covers 7 s recording time. Notice how the resolution of the data decreases with time (downwards). The vertical stripes are from swell-noise.

full 360° are found. These results compare well with measurement data obtained from real marine seismic exploration. All simulations are performed in 3D and the resulting data are visualized through state-of-the-art volume visualization software.

5.1 Introduction

In this article, we will look at the generation and propagation of flow noise around and inside an axisymmetric cylinder that is aligned with the flow direction. A prime example of this type of flow occurs on towed sonar arrays, commonly used for maritime surveillance and geophysical exploration. Figure 5.1(a) shows a schematic of a vessel recording seismic data. The seismic source is an air gun array that releases energy that partly travels down into the subsurface, where it is refracted and reflected by geological features. Some of the reflected energy is picked up by long hydrophone arrays that are towed behind the vessel.
The hydrophones are grouped in sections. From each section the input from the hydrophones are summed, and a trace, representing the reflected energy, is produced. A 6 km long hydrophone array (streamer) will typically record 480 traces, and a modern vessel can tow up to 20 parallel streamers.

As a general definition we can say that any recorded energy which interferes with the desired signal can be considered as noise. The noise can be classified as background noise (for instance wind, swell, noise from nearby production, or interference from nearby seismic acquisition), source-generated noise (for instance direct and scattered waves or multiples), and instrument noise and can show up as coherent or incoherent energy in seismic gathers.
During marine seismic exploration, the amount of recorded turbulent flow noise compared to other types of noise depend both on the flow velocity and weather conditions. However, with normal operation velocities, and in calm weather, turbulent flow noise typically makes up more than 50% of the recorded noise in a seismic survey Elboth et al. (2010a).
Figure 5.1(b) shows a shot-gather recorded on a marine seismic hydrophone array. The amount

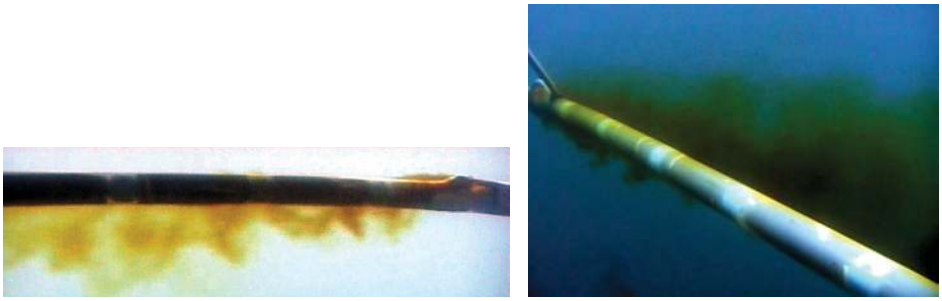

(a) (b)

Figure 5.2: Snapshots of the turbulent boundary layer surrounding a seismic streamer array. Image a): Cross-section view visualized by a single hole dye release. Image b): 3D view by a multi hole dye release. The streamer was towed at $4\,\text{kn} \approx 2\,\text{m/s}$ when the pictures were taken. The cable diameter is $5\,\text{cm}$.

of reflected energy decreases with time or depth. As the magnitude of the reflected energy approach the noise level, the quality of the seismic data decreases. This can be observed below $5\,\text{s}$.

According to Lighthill (1978), the flow noise level scales with vessel velocity as U^6 to U^8. This often limits the operational speed in which hydrophone array systems can be operated. In addition, flow noise is broad banded and covers much of the same frequency bands as the reflected seismic signal. To the best of our knowledge no known software filter algorithm is able to separate flow noise from the rest of the signal in a satisfactory way.

Figures 5.2(a) and 5.2(b) show snapshots of a seismic cable in the ocean. A colored dye is released to visualize the boundary layer. From these pictures the turbulent nature of the flow can clearly be observed. Through measurements Elboth et al. (2009b) it can be shown that the efficient Reynolds number Re_L of the flow along a seismic streamer at $5\,\text{kn}$ is around $3 \cdot 10^6$. The motivation for this work is to increase our understanding of flow noise on seismic hydrophone arrays, with a future objective of being able to reduce its influence.

5.1.1 Previous work

Turbulent flow noise is a common problem encountered in many types of engineering. The theoretical background for understanding turbulence as a source of noise, was laid out in the classical paper Lighthill (1954). Later contributions were added by Ffowcs Williams and Hawkings (1969), where surface effects were added. Traditionally, most flow noise research has focused on the noise emitted by jets, as this is relevant from an environmental point of view. Some recent relevant works are Bogey and Bailly (2007), Barre et al. (2006), Bogey et al. (2007) and Freund et al. (2002). Relevant works focusing more on measurements in turbulent boundary layers are Bull (1996) and Arguillat et al. (2005) who provide spectra of both the acoustic pressure field and the pressure fluctuations of wall pressure beneath turbulent flows.

In Hu et al. (2003) and Hu et al. (2006) a Re_τ=1440 Direct Numerical Simulation (DNS) of channel flow is used to study sound radiation from a turbulent boundary layer. They found that for low to medium Reynolds number flows, dipole radiation due to wall shear stress and

quadrupole radiation from Reynolds stresses $u_i u_j$ are of similar magnitude. However, for high Reynolds number flows, relevant in geophysical applications, the quadrupole radiation is dominating.

A number of articles on axisymmetric flow have been written in fluid dynamics. These works are mainly concerned with velocity and pressure fluctuations, and does not look at the acoustic field. However, they are still relevant, since the acoustic source terms, see Equation 5.1, relate directly to the turbulent fluctuations. Early work focusing mainly on the average flow on axially symmetric cylinders ($\alpha = 0°$) was carried out by Willmarth and Yang (1970) and Denli and Landweber (1979). In Willmarth et al. (2006) this is followed up and extended further. All these works investigate wall pressure fluctuations in conjunction with the mean velocity profiles. In Willmarth and Sharma (1984) and later also in Snarski and Lueptow (1995), similar studies were performed where the turbulent flow properties also were investigated. However, despite decades of research on the subject, there is still uncertainty over many of the fundamental relations for turbulent, axisymmetric boundary layers. For example, competing scaling relations for the mean-velocity profile near the cylinder wall have been proposed by Afzal and Narasimha (1976), Denli and Landweber (1979), and Lueptow et al. (1985) amongst others. Both Lueptow et al. (1985), and Heenan and Morrison (2002a), as well as a number of other researchers have shown that even a small misalignment of the axis of a cylinder relative to the mean flow will cause asymmetry of the boundary layer. This will induce significant deviations in the fluctuating wall pressure levels around the circumference of the cylinder. Early numerical simulations of axial flow were conducted by Neves and Moin (1994b,a) where they presented detailed turbulence statistics for axially aligned flow. DNS of near axial flows is also reported by Woods (2006). A recent overview of flow along long thin cylinders is also given by Tutty (2008b).

Within the field of geophysical exploration it is a goal to acquire data with as little noise as possible. A gradual improvement in data quality both through engineering and software development has taken place in recent years. Some relevant articles discussing engineering improvements on marine seismic streamers are Schoenberger and Mifsud (1974), Bjelland (1993), Brink and Spackman (2004) and Dowle (2006). A few recent articles on software de-noising are Watts et al. (1999), Gulunay (2008) and Elboth et al. (2008). Important recent contributions to the understanding of flow noise on streamer arrays are the works by Knight (1996) and Cipolla and Keith (2008).

As a result of design improvements, the relative importance of flow noise compared to other types of noise, has increased (Elboth et al., 2009b). It is therefore apparent that in order to further reduce the amount of recorded noise during seismic acquisition, the influence of flow noise needs to be reduced.

To our knowledge, no previous work has been published where an acoustic analogy has been used to simulate flow noise in an axisymmetric hydrophone array.

5.2 Method

This analysis of turbulent flow noise relies upon a so-called acoustic analogy, where the Navier-Stokes equations are transformed into a form reminiscent of the wave equation of "classical" (i.e., linear) acoustics. The most widely-used analogy is Lighthill's acoustic analogy presented

in Lighthill (1954). This inhomogeneous wave equation reads

$$\left(c_0^2\nabla^2 - \frac{\partial^2}{\partial t^2}\right)\rho = -\frac{\partial^2 T_{ij}}{\partial x_i \partial x_j}. \tag{5.1}$$

The source term $T_{ij} = \rho u_i u_j + (p - c^2\rho)\delta_{ij} - \tau_{ij}$ is known as Lighthill's stress tensor and is responsible for the generation of acoustic fluctuations (sound). Here, c_0 is the speed of sound, ρ is the density perturbation and p denotes pressure. The term $u_i u_j$ represents the velocity tensor at a given spatial location. For high Reynolds numbers the viscous stress tensor τ_{ij} can be neglected. For most geophysical applications it is also reasonable to assume incompressibility, i.e., $\rho = \rho_0$. The $(p - c^2\rho)$ term is normally responsible for thermo-acoustic effects, and will also be neglected for the data we currently are considering. To incorporate the effects of surfaces, Ffowcs Williams and Hawkings (1969) extended the work of Lighthill. Here we will use a simplified Ffowcs Williams acoustic analogy given as

$$\left(\frac{1}{c_0^2}\frac{\partial^2}{\partial t^2} - \nabla^2\right)p' = -\frac{\partial^2 \hat{T}_{ij}}{\partial x_i \partial x_j} - \frac{\partial \hat{T}_{ij}}{\partial x_i}\Big|_{z=0}^{z=2h}. \tag{5.2}$$

The term $p' = p/\rho$ is the fluctuating acoustic pressure. $\hat{T}_{ij} = u_i u_j - \nu\frac{\partial u_i}{\partial x_i}$, where ν denotes kinematic viscosity. The last term in the equation is only to be evaluated at the boundary. The right hand side in Equation 5.1 or 5.2 can be computed from DNS data for boundary layer flows.

The computations performed here are based on an incompressible three-dimensional DNS of a low Reynolds number channel flow ($Re_\tau = u_\tau l/\nu = 180$) from a high order spectral element code (Wasberg et al., 2009). Here, u_τ is the friction velocity, and ν denotes viscosity. The computations are performed on a non uniform grid with resolution $480 \times 240 \times 241$ in the stream-wise, span-wise and wall normal direction respectively. Physically, the computational box has a size of $1.44 \times 0.72 \times 0.36\,\mathrm{mm}$. The flow field with boundary conditions is illustrated in Figure 5.3.

From the DNS data we compute the source term given as the right hand side of Equation 5.1 or 5.2. This term is then re-sampled to a uniform grid of $512x256x128$ points, before Equation 5.2 is solved explicitly on a staggered grid using an eight-point finite difference scheme for spatial discretization. A forth-order Runge-Kutta algorithm is applied for time integration. The DNS has a lower Reynolds number than a real flow around a streamer array. Theoretically, this implies that the inertial subrange of the flow is smaller, and that a simulation will contain fewer small features with high energy. Acoustically this probably means that the simulation will contain less high frequency noise. However, as most of the acoustic energy is expected to be rather low frequency, it is reasonable to assume that the obtained results will capture the essence of the acoustic field.

5.2.1 The acoustic source term

The objective is to look at how turbulent flow noise propagates inside a seismic streamer. To simulate this, we use the acoustic pressure from the channel DNS as a substitute for the acoustic pressure from an axi-symmetric turbulent boundary layer. This acoustic pressure computed by Equation 5.2 and its normal derivative (the grid-cells at the boundary) are transferred onto the

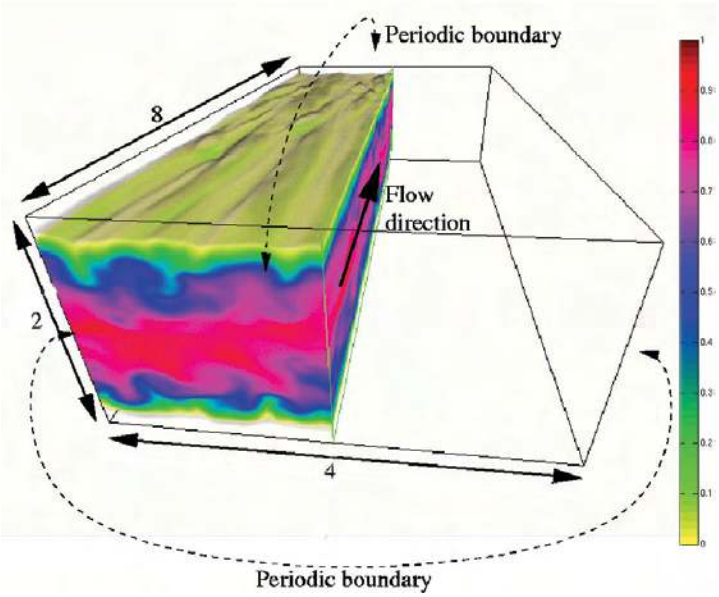

Figure 5.3: Instantaneous flow velocity from the channel flow simulation. Note the periodicity in the boundary conditions. The upper and lower boundaries are solid walls with a non-slip boundary condition. A clip-plane has been applied during visualization to better see the velocity distribution.

surface of a cylinder. A wave-equation, in cylindrical coordinates, is then used to propagate this acoustic pressure inside the cylinder. This is illustrated in Figure 5.4.
Figure 5.5 shows an instantaneous picture of how the energy $\hat{T}_{ii}^2$ from the source term is distributed in the channel. The double index ii implies summation. In non-dimensional coordinates, we find that $\hat{T}_{ii}$ peak at

$$z^+ \equiv z u_\tau / \nu \approx 30 - 35. \tag{5.3}$$

This is on the border between the viscous sublayer and the log-layer in a turbulent boundary layer. Here, the friction velocity u_τ is $1\,\mathrm{m/s}$ and $\nu = 1/180$. The characteristic length-scale l is set to half the channel height. This is consistent with results known from the literature Chang (1998) where the Reynolds stresses usually peak at $z^+ \approx 20$. From the right image in Figure 5.5. We also notice that the uu-velocity component is dominating, and that close to the wall ($y \to 0$), the tensor scales like z^2.

In z^+ coordinates, the cylinder has a diameter of $720/\pi \approx 230$ while the simulated channel boundary layer has a thickness of around $z^+ \approx 100$, see Figure 5.5. According to Bokde et al. (1999), the turbulent boundary layer on a cylinder in axial flow is not significantly different from that on a flat plate when the boundary layer thickness is of the same order or smaller than the radius of the cylinder. For a cylindrical geometry the turbulent structures are not bounded in the span-wise direction, and are free to move around the streamer. The result of this has been summed up in Heenan and Morrison (2002a), where they found that for a cylindrical geome-

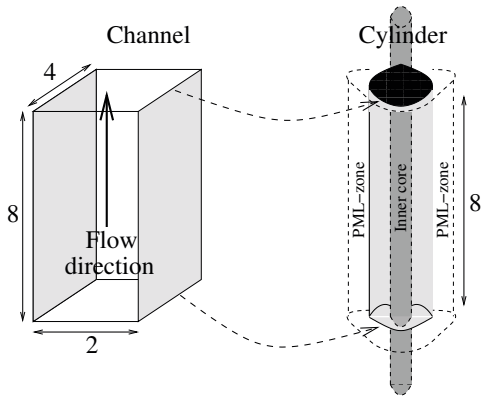

Figure 5.4: The sketch shows how the output from the acoustic computations in the channel(left) is used as input on the cylinder surface(right).

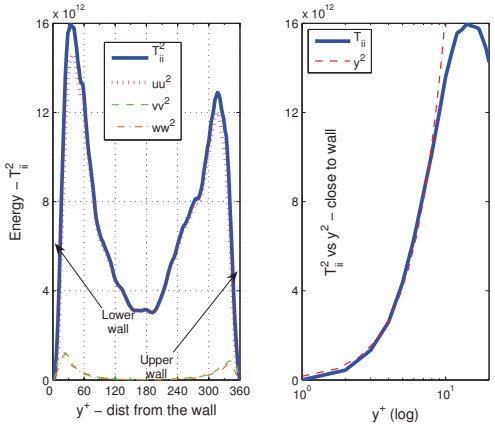

Figure 5.5: Average turbulence intensity profile. The left image shows the energy of the $\hat{T}_{ii}$-tensor, as well as the contribution from the different velocity components. The right image shows how $\hat{T}_{ii}$ scale close to the wall. The double index in T_{ii} implies summation.

try, the Reynolds stresses $\overline{u_i u_j}$ and the shear stress τ_w tend to be larger close to the surface, and smaller further away from the surface compared to the flat plate case. This is relevant for flow noise generation through Equation 5.2. Summing up, we state that the extrapolation of the acoustic noise field from a channel flow to the surface of a cylinder is not a perfect solution. However, we believe that the artifacts introduced are minor, and that the present data still captures the relevant parts of the physical problem we are studying.

5.2.2 Acoustic Boundary conditions

For the propagation of the acoustic self-noise in the channel, periodic boundary conditions in the span-wise directions are retained. However, in order to avoid an unnatural build-up of acoustic energy, the stream-wise and the wall-normal boundaries have been given a PML absorbing boundary condition.
The speed of sound in the streamer hose c_{hose} deviate by a few percent from c_{water}. This means that a few percent of the acoustic pressure are reflected, while the remaining will propagate into the cylinder. Near the center core of the cylinder we have implemented a reflective boundary to simulate the presence of a metal wire. To avoid build-up of acoustic energy, the cylinder is surrounded by a PML absorbing boundary layer.

5.2.3 Quadrupole, dipole and monopole radiation

According to Lighthill (1978), noise generated by turbulence is quadrupole in nature. This means that its intensity drops off as $1/r^4$, where r is the radial distance to the source. This implies that flow noise can be difficult to detect from a remote observer, but it is not necessarily weak at the surface of an array close to where the Reynolds stresses (the fluctuating velocity components $u_i u_j$) peak. Quadrupole noise is produced by the $u_i u_j$ source term, while the remaining terms on the right hand side of Equation 5.2 are dipole sources. For high Reynolds number flow, Hu et al. (2003) states that quadrupole noise is dominating and that the monopole source is small. However, as the input DNS data only has medium Reynolds number, we initially opted to retain some dipole sources for the present computations. Numerical experiments shows that for the present low Mach number, moderate Strouhal number, and moderate Reynolds number DNS data, around 99% of all acoustic far-field energy is obtained by only including the source terms suggested by Landau Lifshitz in Landau and Lifshitz (1987).

$$\frac{\partial^2 \hat{T}_{ij}}{\partial x_i \partial x_j} \approx \rho\Big(\frac{\partial^2 u_i u_j}{\partial x_i \partial x_j}\Big). \tag{5.4}$$

In an ocean environment, there is also the added complexity of hydrostatic pressure variations due to wave-motion and cross-flow over seismic streamers. In Elboth et al. (2009b) it is shown that for frequencies below 10 Hz, these noise sources can be very large. With the present DNS input data, we were not able to simulate these types of flow noise.

5.2.4 Perfectly Matched Layers - PML

The PML boundary condition was first introduced by Berenger (1994) for Maxwell's equations. Later it has been adapted and extended for use with a number of other wave-like equations. In this work, we have adapted a formulation given by Hu (2005) for the Euler equations to be used with Equation 5.1 or 5.2. The basic idea is that PML provides boundary conditions that ensure that a wave does not reflect from the ends of the computational domain. This is an important prerequisite for acoustic computations. For computational reasons it is convenient to rewrite the wave equation

$$\frac{\partial^2 \hat{p}}{dt^2} = c_0^2 \frac{\partial^2 \hat{p}}{\partial x_j^2} \tag{5.5}$$

as a first-order pressure-velocity system

$$\frac{\partial p}{\partial t} = c^2 \rho \left(\frac{\partial u_j}{\partial x_j}\right) \tag{5.6}$$

$$\frac{\partial u_j}{\partial t} = \frac{1}{\rho}\left(\frac{\partial p}{\partial x_j}\right), \qquad j = \{1, 2, 3\}. \tag{5.7}$$

Here, $\hat{p}(x_i, t)$=$\partial p/\partial t$ is the amplitude and c is the sound velocity. The term ρ denotes the density of the medium where the wave are propagating. For simplicity, we have not included the acoustic source term in this formulation. We apply the variable changes

$$\frac{\partial}{\partial x_j} \rightarrow \frac{1}{1 + i\sigma_{x_j}/\omega} \frac{\partial}{\partial x_j}, \qquad j = \{1, 2, 3\}.$$

Here, $\sigma_x(x)$, $\sigma_y(y)$ and $\sigma_z(z)$ are absorption coefficients. They are zero in the computational domain, and are increased smoothly to one in the PML zone. The variable i represents the imaginary number and ω is the frequency. In the frequency domain, we multiply Equation 5.6 and 9.10 with $(1 + i\sigma_x/\omega)(1 + i\sigma_y/\omega)(1 + i\sigma_z/\omega)$, and apply the variable change described above. Back in the time domain, the PML formulation for 3D-Cartesian coordinates becomes:

$$\begin{aligned} \frac{1}{c^2\rho}\frac{\partial p}{\partial t} &= \frac{\partial u_j}{\partial x_j} + (\sigma_y + \sigma_z)\frac{\partial(\psi 1_u)}{\partial x} + (\sigma_x + \sigma_z)\frac{\partial(\psi 1_v)}{\partial y} + (\sigma_x + \sigma_y)\frac{\partial(\psi 1_w)}{\partial y} \\ &+ \sigma_y\sigma_z\frac{\partial(\psi 2_u)}{\partial x} + \sigma_x\sigma_z\frac{\partial(\psi 2_v)}{\partial y} + \sigma_x\sigma_y\frac{\partial(\psi 2_w)}{\partial y} - \beta_1 p - \beta_2\psi 1_p - \beta_3\psi 2_p \end{aligned} \tag{5.8}$$

$$\rho\frac{\partial u}{\partial t} = \frac{\partial p}{\partial x} + (\sigma_y + \sigma_z)\frac{\partial(\psi 1_p)}{\partial x} + \sigma_y\sigma_z\frac{\partial(\psi 2_p)}{\partial x} - \beta_1 u - \beta_2\psi 1_u - \beta_3\psi 2_u \tag{5.9}$$

$$\rho\frac{\partial v}{\partial t} = \frac{\partial p}{\partial y} + (\sigma_x + \sigma_z)\frac{\partial(\psi 1_p)}{\partial y} + \sigma_x\sigma_z\frac{\partial(\psi 2_p)}{\partial y} - \beta_1 v - \beta_2\psi 1_v - \beta_3\psi 2_v \tag{5.10}$$

$$\rho\frac{\partial w}{\partial t} = \frac{\partial p}{\partial z} + (\sigma_x + \sigma_y)\frac{\partial(\psi 1_p)}{\partial z} + \sigma_x\sigma_y\frac{\partial(\psi 2_p)}{\partial z} - \beta_1 w - \beta_2\psi 1_w - \beta_3\psi 2_w. \tag{5.11}$$

Here, $\beta_1 = (\sigma_x + \sigma_y + \sigma_z)$, $\beta_2 = (\sigma_y\sigma_z + \sigma_x\sigma_z + \sigma_x\sigma_y)$ and $\beta_3 = \sigma_x\sigma_y\sigma_z$. The auxiliary variables ψ can be updated as

$$\begin{aligned} \frac{\partial(\psi 1_p)}{\partial t} &= c^2\rho p \qquad & \frac{\partial(\psi 2_p)}{\partial t} &= \psi 1_p \\ \frac{\partial(\psi 1_{u_j})}{\partial t} &= c^2\rho u_j \qquad & \frac{\partial(\psi 2_{u_j})}{\partial t} &= \psi 1_{u_j}, \qquad j = \{1,2,3\}. \end{aligned} \tag{5.12}$$

Note that a large number of fields and variables are needed in this formulation. However, the auxiliary variables only need to be stored and computed in the PML-region. Also note that when we have a non-PML boundary condition in a given direction, the σ in that direction will also be zero. This greatly simplifies Equation 5.8 to 5.11. Numerical experiments have shown that the PML-region needs to be at least 15 grid cells wide to avoid reflections.

5.2.5 Cylindrical coordinates

In cylindrical coordinates (r, θ, z), the mathematical expressions describing PML are simplified compared to the 3D Cartesian case. This is mainly because no PML will ever be needed in the θ direction. In the z-direction, we can normally also use a reflective or a periodic boundary condition. This means that PML in cylindrical coordinates only needs to be employed on the radial r-direction. Some attention needs to be paid in the center of a cylinder to avoid numerical problems. However, when simulating a streamer array, this problem can neatly be avoided by placing a reflective Neumann boundary condition along a cylinder near the center of the streamer. This will physically represent the metal wire that goes through the center of most hydrophone arrays.

5.3 Analysis

5.3.1 Spectral estimates

Figure 5.6 compares the power spectrum from a time-series in the simulation with a time-series taken from a real noise data acquired during a seismic survey. The frequencies are scaled by an estimate of displacement thickness δ^* and flow velocity. For the simulation data we used half the channel height as δ^*_{DNS}, while an estimate of $\delta^*_{seismic} \approx 4\,\text{mm}$ based on Reynolds number Tutty (2008b), was used for the real seismic data. There is a reasonably good fit for low frequencies, where also most of the energy is found. However, for high frequencies the simulation data drops of. This is probably due to the relative low Reynolds number in the simulation compared to the real seismic data.

5.3.2 Correlation distances

An engineering objective is always to maximize signal-to-noise (S/N)-ratio recorded data. One common approach to obtain a higher (S/N)-ratio is to increase the number of the data-sensors. For geophysical exploration, these sensors (hydrophones) are normally placed inside the seismic streamer. If the noise between individual sensors are uncorrelated, while the signal is correlated,

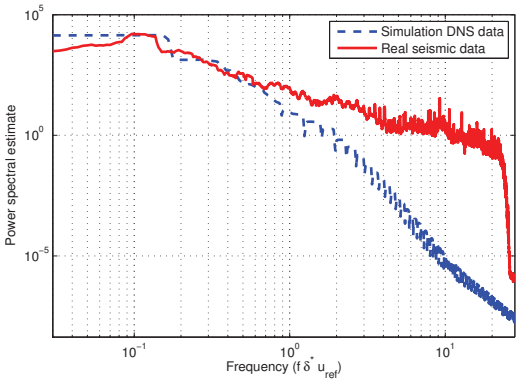

Figure 5.6: Spectral estimates of the frequency content for time-series both from simulation DNS data and from a real seismic survey (single sensor data). The spectral estimates were obtained by using a multi-taper method Thomson (1982). Notice that the y-axis is logarithmic.

the S/N-ratio will improve as $\sqrt{n} \cdot S/N$, where n is the number of hydrophones[1]. There is however also a limit. If sensors are places to close together, they will record the same noise, and no S/N improvement is achieved. A limiting factor for the number of sensors to employ is therefore the physical correlation distance of the noise we want to attenuate.

5.3.3 One-dimensional Correlations

In Figure 5.7, we have computed a number of 1D correlations in the streamwise direction in the cylinder. From this figure we observe that the correlation distance of the flow noise varies, but that on average it is around 250 z^+ units.

We also compute the integral length-scale L, defined as

$$L = \int_0^{r_c} c(x)dx. \tag{5.13}$$

Here, r_c is where the correlation coefficient $c(z)$ has its first zero-crossing. In Figure 5.8, we have computed L for a great number of one-dimensional cases in the stream-wise direction. We also did a numerical experiment where 2% of the low frequency part of the boundary layer pressure field was allowed to propagate through the streamer surface. This was done to study how this might influence the correlation distance. Figure 5.9 shows how this influences the correlation length-scale by doubling the average value.

The cylinder diameter is 230 z^+ units. This means that typical correlation integral length-scales are $0.5 - 2$ times the cylinder diameter, ref Figure 5.8 and 5.9. In physical coordinates, using a seismic streamer with a diameter of $5\,\text{cm}$, we could expect the correlation integral length-scale to be $2.5 - 10\,\text{cm}$ for the acoustic field. Such an estimate fits well with measure-

[1] It is a reasonable assumption that any signal from sub-surface reflections will be correlated over tens of meters. A seismic reflection signal is therefore strongly correlated over neighboring hydrophones.

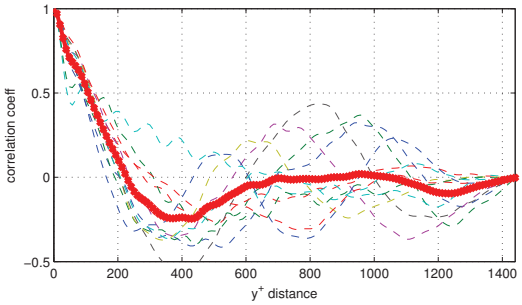

Figure 5.7: Stream-wise correlations of the acoustic pressure field taken from the cylinder simulation. The stapled lines represent auto-correlations taken at different time-steps, while the tick line represents an average. The measurement points were about half way between the cylinder surface and center.

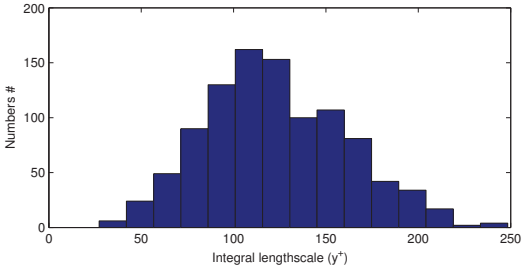

Figure 5.8: Histograms of the integral length-scale L in the stream-wise direction. The measurement points were at the same position as in Figure 5.7.

ments done on real seismic data. In Elboth et al. (2010a), it is shown that after the application of a 2 Hz low-cut filter to remove hydrostatic pressure variation from ocean waves, a typical integral length-scale for flow noise over a real seismic streamer is 8 cm. The simulation therefore appears to be well suited to derive this parameter which is an important design parameter for streamer arrays. We have also made computations in the spanwise (θ) direction to look at the correlation around the cylinder. In this direction, it is natural to use degrees as the length-scale measure. Figure 5.10 shows that in the spanwise direction the correlation distance is strongly varying with $L_{average} = 79^\circ$ while $L_{median} = 66^\circ$.

These results differ somewhat from the wall pressure fluctuation measurements presented by Bokde et al. (1999) and Willmarth and Yang (1970). In the boundary layer, they found spanwise correlations of wall pressure of around 30° and 24° respectively. However, their experiments were performed after filtering that had removed all frequencies below 60 and 100 Hz. Their measurements were performed on the outer surface of a cylinder while our data is taken inside the cylinder, and is of the acoustic pressure. Based on numerical experiments, Neves and Moin (1994b) found that the spanwise wall-pressure correlation angle mostly

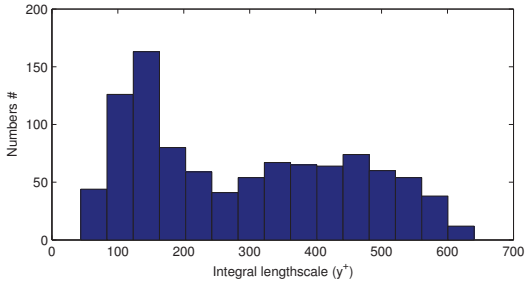

Figure 5.9: Histograms of the integral length-scale L in the streamwise direction when 2% of the boundary layer pressure was allowed to propagate through the streamer surface.

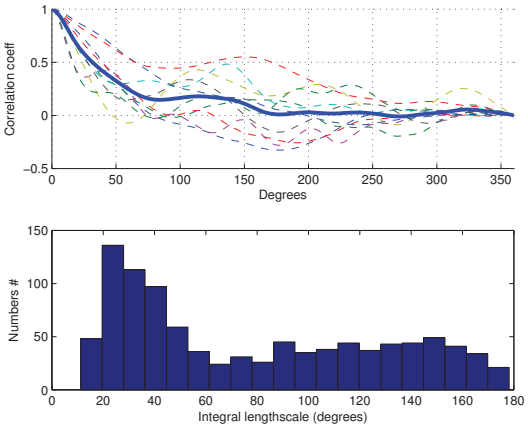

Figure 5.10: From the cylinder: Top image: Spanwise (θ) correlation distances. The stapled lines represent individual auto-correlations taken at different time-steps, while the tick line represents an average. Bottom image: Histograms of the integral length-scale L in the spanwise direction.

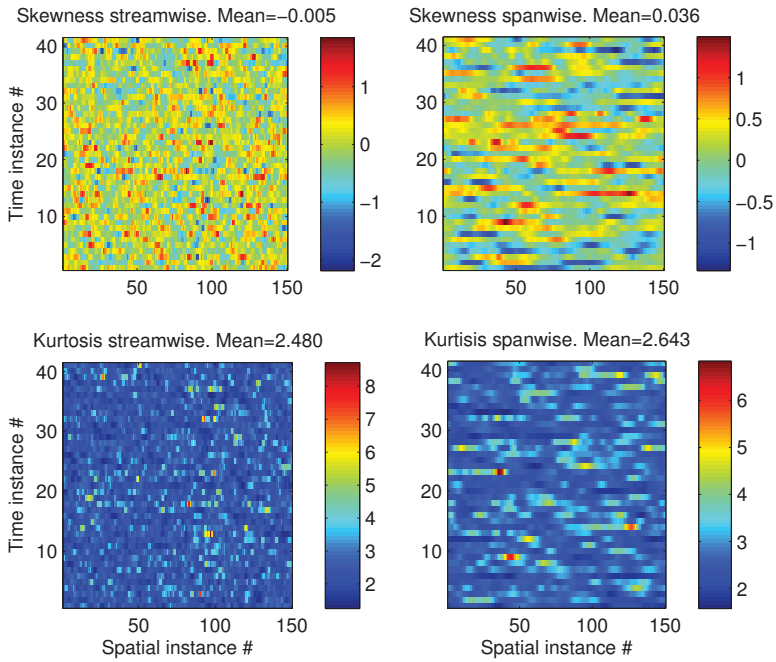

Figure 5.11: Skewness and kurtosis computed different time-steps and spatial locations. Values are indicated by the color-bar. The measurement points are the same as in Figure 5.7.

depended on the geometry δ/a, where a denotes cable radius, and that there was little dependence on Reynolds number.

5.3.4 Higher order moments

Skewness $S_i = \langle p_i^3 \rangle / \langle p_i^2 \rangle^{\frac{3}{2}}$ is a measure of anisotropy of the data around the sample mean. If skewness is negative, the data is spread out more to the left of the mean than to the right. The skewness of a symmetric distribution is zero. The kurtosis $K_i = \langle p_i^4 \rangle / \langle p_i^2 \rangle^2$ is a measure of how outlier prone a distribution is. The kurtosis of a normal distribution is 3. More outlier prone distributions will have a higher kurtosis value than 3.

In Figure 5.11, both skewness and kurtosis are computed for a large number of instances in the simulation. The skewness has an average that is close to zero. On average, the acoustic pressure therefore seems to have a distribution that is fairly symmetrical. Its maximum values are ± 1 both in the streamwise and spanwise direction. This indicates that the acoustic pressure sometimes shows an anisotropic behavior. The kurtosis has a mean around 2.5, but occasionally higher values (up to around 10) are found both streamwise and spanwise. This also indicates the occasional presence of strong fluctuations. The Kurtosis mean of 2.5 shows that the distribution on average are flatter than a Gaussian.

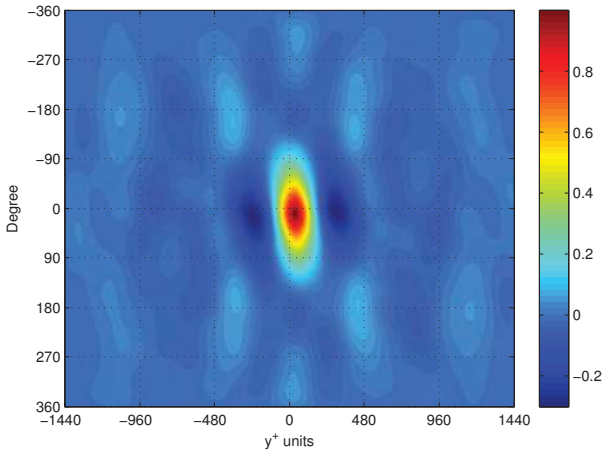

Figure 5.12: Average correlation from 20 $z-\theta$ planes from the cylinder. The measurement points are about 33% in from the cylinder surface.

5.3.5 2D auto-correlations of acoustic field

In Figure 5.12, an average of 20 2D auto-correlation of a $z-\theta$ plane is plotted. From this plot it is apparent that correlation distance is around $z^+ \approx 200$ in the streamwise direction. Spanwise the data is correlated around $\pm 90°$.

5.3.6 Propagation velocities

The acoustic propagation velocity is a measure of the average velocity of the dominating acoustic sources. This indicates where in the turbulent boundary layer most of the observed flow noise is produced. We find the propagation velocity by cross-correlating two instances of the acoustic field on the outer cylinder surface. This correlation will have a peak with a certain lag. By comparing this lag with the distance the free flow U=U_0 has propagated over the time period between the two fields, the propagation velocity can be found. The term U_0 is the average streamwise velocity in the middle of the channel.
In the current dataset, the propagation velocity of the acoustic pressure at the cylinder surface was consistently $0.69\,U_0$. This corresponds to the velocity found around $z^+ \approx 25$, which is close to where T_{ij} peak, see Figure 5.5. Since most of the acoustic noise source is quadrupole, the acoustic pressure drops like $1/r^4$ from the source. This means that a relative small source close to a sensor might contribute more to the recorded noise than a larger source placed further away. Our estimates are in line with measurements from Willmarth and Yang (1970) who reports convection velocities on the range of $0.56\,U_0$ to $0.83\,U_0$. Based on simulation data, Tutty (2008b) reports a convection velocity for pressure producing turbulent structures in a cylinder boundary layer of 0.7.

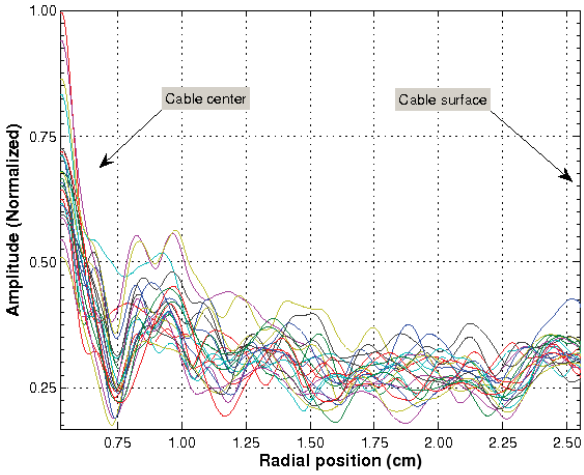

Figure 5.13: Flow noise levels as a function of distance from the center of a cable with diameter $y^+ = 1440$. On a real seismic streamer this roughly corresponds to a radius of $5.2\,\mathrm{cm}$. The sharp increase towards the center is partly caused by a reflective boundary near the cylinder core used in the simulation.

5.3.7 Noise distribution inside the cable

Traditional wisdom says that to avoid flow noise, sensors (hydrophones) should be placed as fare away from the cable surface (where the flow noise is produced) as possible. Based upon our simulation of flow noise propagation inside a cylinde, we plotted flow noise level as a function of distance from the cable surface in Figure 5.13. The diameter of the cable is $y^+ = 1440$. By using Equation 3.7, from a real seismic streamer flow, this can be converted to a diameter of roughly $10\,\mathrm{cm}$. From this last figure, it seems like flow noise level is independent of sensor position. This was a somewhat surprising result. What probably happens is that the $1/r^4$ decrease of amplitude with separation (turbulence creates quadrupole noise) is counteracted by the cylinders ability to focus energy towards its center. However, it is also a valuable result in that removes previously assumed limitations as to how hydrophones (or other sensors) need to be placed inside a streamer array. These numerical results were also partly confirmed by field tests where we recorded flow noise on our purpose built hydrophone array. Within this array, we had placed hydrophones with varying separation from the outer hose. The data did not show any significant difference in flow noise level on these hydrophones. .

5.4 Volume visualization

In this section, we will use a volume visualization tool (Gaarder and Helgeland, 2002) to investigate the acoustic fields produced by our simulation.

Figure 5.14 shows a snapshot of the source-term $\partial^2(u_i u_j)/\partial x_i \partial x_j$ from Equation 5.4. We

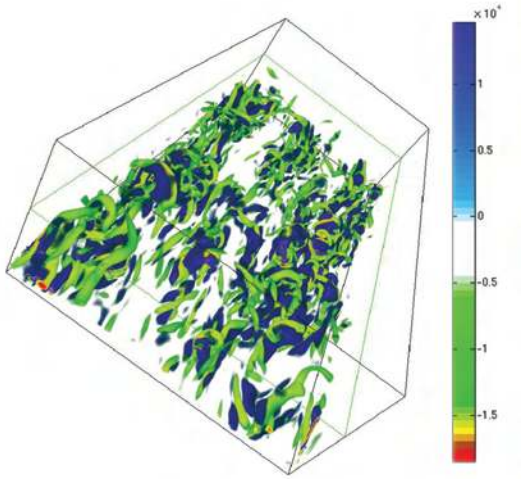

Figure 5.14: Instantaneous source term from Equation 5.4 visualized for the lower half of the channel data.

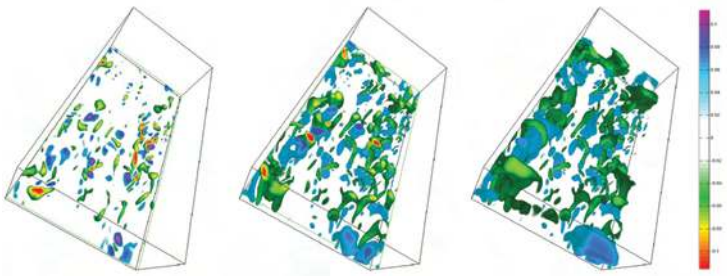

Figure 5.15: Instantaneous acoustic noise field in the lower half of the channel used to simulate a turbulent boundary layer. From left to right a clip-plane has been applied to better visualize the character of the data.

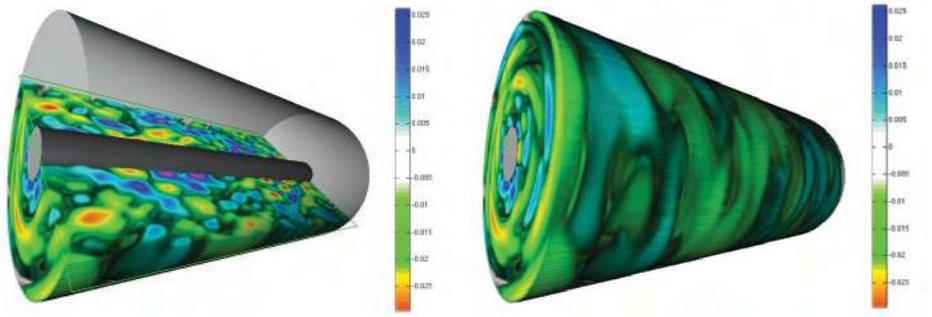

(a) (b)

Figure 5.16: Instantaneous noise field inside the cylinder. Image a) shows the field with a clip-plane. Image b) shows the whole cylinder. The cylinder in the center of the images represents the steel wires that go through the center of most hydrophone arrays, while the semi-transparent surface represents the outer surface.

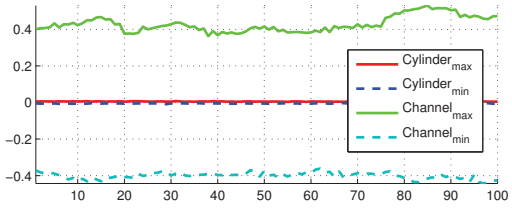

Figure 5.17: The relation between the maximum and minimum values found in the channel (source-field) and in the cylinder (far-field) for a chosen time-range.

observe that the small details in the noise field are rather chaotic. Negative pressure (green color) tends to be more tube-formed than the positive pressure (blue color) which are more blobbed. The source term gets smoother as it is propagated acoustically. Figure 5.15 shows a snapshot from the acoustic noise field in the DNS channel derived from Equation 5.1. The acoustic field in the cylinder looks quite different, see Figure 5.16(a). It is smoother and does not have small scale features. Another thing to notice is that the minimum and maximum values of the cylinder is significantly smaller than those found in the channel. This is further quantified in Figure 5.17. A question to pose is why the acoustic field in the cylinder is smoother than in the channel. This can be explained by transferring Equation 5.1 to the frequency domain. After dropping the time-dependence, we obtain

$$ck^2 p \sim \rho k^2 u_i u_j \rightarrow cp \sim \rho u_i u_j. \tag{5.14}$$

The sound-field p is quadrapole, i.e., the amplitude decays like $1/r^4$ with distance r. The effects of multiplying the amplitudes with this decay factor, corresponds to convolving with the same factor in Equation 5.14. The function $1/r^4$ is very smooth and approaches zero rapidly. The result is a smoothing of the acoustic fluctuations in the far-field as we observe in Figure 5.16(a).

5.5 Conclusions

This article has outlined how a DNS of turbulent flow can be used as a basis for an acoustic noise-field computation through the use of an acoustic analogy. Due to a moderate Reynolds number it was not possible to capture all the high frequency fluctuations found in the reference flow we were attempting to simulate. However, features such as the propagation velocity and the coherence distance of the acoustic flow noise field were well captured. They were found to be $0.69\,U_0$ and $5-10$ cm respectively, which close to what is found on real seismic streamers. This shows that a computer simulation can be used to determine design parameters for acoustic sensor arrays.

Another result from our simulation is that the flow noise level inside a streamer streamer does not seem to depend on the distance from the surface. This removes previously assumed limitations on hydrophone placements for future streamer designs.

We have used visualization software to make illustrative images of the instantaneous acoustic field inside a cylinder. Together with an analysis of the governing equations this has improved our understanding of turbulent flow noise. Turbulent flow noise fluctuates around a mean and is fairly isotropic most of the time. However, occasional outliers appear, that probably make significant contributions to the total rms-pressure level. This opens up the possibility that if these energetic outliers could be avoided through design changes, or filtered out, a significant reduction in the rms flow noise level could be achieved.

5.6 Future work

This work presents some results from a research project where the objective is to study seismic noise. Within this project it is a goal to use an axisymmetric high-Reynolds number boundary

layer as input data instead if the channel-data used here. This is an ongoing effort that hopefully will be achieved soon. In addition, we would like to use more refined boundary conditions for the interaction between the acoustic pressure and the cylinder (streamer) surface. This is all done to try to improve our physical understanding of flow noise, with a future aim of being able to dampen its influence through either design-changes on the hardware or through software filtering algorithms.

Chapter 6

Time-frequency seismic data de-noising

Thomas Elboth <thomae@math.uio.no>
Fugro Geoteam AS, Hoffsveien 1c, P.O.Box 490 Skøyen N-0213 Oslo, Norway
Mechanics Division, Department of Mathematics, University of Oslo, Norway
Ida Vik Presterud <ida@presterud.no>
Department of Geosciences, University of Oslo, Norway
Dag Hermansen
Fugro Seismic Imaging AS, Hoffsveien 1c, P.O.Box 490 Skøyen N-0213 Oslo, Norway

Journal article originally published as:
T. Elboth, I. V. Presterud and D. Hermansen: Time-frequency seismic data de-noising, Geophysical Prospecting XXX, in press (2010)

Abstract

Marine seismic data are always affected by noise. An effective method to handle a broad range of noise problems is a **T**ime-**F**requency **D**e-**N**oising (TFDN) algorithm. In this paper we explain details regarding the implementation of such a method. Special emphasis is given to the choice of threshold values, where several different strategies are investigated. In addition we present a number of processing results where time-frequency de-noising has been successfully applied to attenuate noise resulting from swell, cavitation, strumming, and seismic interference. Our seismic interference noise removal approach applies time-frequency de-noising on slowness gathers (τ-p domain). This processing trick represents a novel approach, that efficiently handle certain types of seismic interference noise that otherwise are difficult to attenuate. We show that time-frequency de-noising is an effective, amplitude preserving and robust tool that gives superior results compared to many other conventional de-noising algorithms. (For example frequency filtering, τ-p or fx-prediction). As a background, some of the physical mechanisms responsible for the different types of noise are also explained. Such physical understanding is important because it can provide guidelines for future survey planning and for the actual processing.

6.1 Introduction

Seismic data always consist of a signal and a noise component. As a general definition we can say that any recorded energy which interferes with the desired signal can be considered as noise. The noise can be classified as background noise (e.g., wind, swell, noise from nearby production platforms, or interference from nearby seismic acquisition), source-generated noise (e.g., direct and scattered waves or multiples), and instrument noise. This can show up as coherent or incoherent energy in seismic gathers. Fulton (1985) provides a comprehensive overview with examples of many types of noise found in marine seismic. The diversity of noise types with different characteristics makes separation of signal and noise a challenging process. However, efficient noise attenuation or removal is important for high quality imaging, and from an economic point of view. This article will not discuss noise in the form of scattered waves or multiples. Instead we will focus on noise caused by weather, seismic interference, engine/propellers, and strumming/tugging. Smith (1999) claims that costs associated with weather-induced delays can account for up to 40% of the total cost of a marine survey. Such delays usually occur when the wave heights surpass $2 - 2.5\,\mathrm{m}$, reducing the resolution and accuracy of the seismic survey to an unacceptable level.
Seismic interference noise is also quite common, especially in areas like the North Sea and the Gulf of Mexico where lots of exploration activities are taking place. The level of engine or propeller noise varies greatly between different vessels, and can occasionally cause trouble. Finally, tugging/strumming noise is usually problematic in situations of non-optimal weather. This article will give examples of all of these types of noise, and demonstrates how time-frequency de-noising successfully allows for improved imaging.

6.1.1 De-noising methods

There is no single algorithm that can remove all types of noise from seismic gathers. It is rather the combination of a number of different techniques, each adapted to the specific problem at hand, which will lead to optimal de-noising results. Nevertheless, the general algorithm of de-noising can be summarized as:

1. Transform the DATA from the time domain into a domain where SIGNAL and NOISE can be separated.

2. In this new domain, remove or attenuate the NOISE.

3. Transform the DATA back to the time domain.

The main challenge is to identify a suitable domain in which separation of each individual contribution of noise from the signal can be done. Below we will briefly describe some commonly used de-noising algorithms that are relevant for the examples that will follow in this article. A full algorithmic description of a time-frequency de-noising algorithm (TFDN) is provided in the next section.

Frequency filtering

One of the most basic forms of de-noising is frequency filtering. However, simple frequency filters are seldom applied because they remove too much of the seismic signal. A notable exception is low-cut filters used to remove the influence of hydrostatic pressure variations. These variations are due to differences in water depth over the seismic streamer cable caused by ocean waves and/or streamer buckling. In 2-D, the circular movement w due to surface waves of a particle at depth z in deep water is approximately given by Kundu (1977) as:

$$w(x, z) = A\omega e^{-kz} \sin(kx - \omega t). \tag{6.1}$$

Here, A denotes the amplitude of the surface wave. Positive z is downward. The wavenumber is $k = 2\pi/\lambda$, where λ is the wavelength, and $\omega = \sqrt{gk}$ denotes the angular frequency, g being gravity. The main frequency of a $150\,\mathrm{m}$ wave is typically around $0.1\,\mathrm{Hz}$, while a wavelength of $50\,\mathrm{m}$ will have a frequency of around $0.3\,\mathrm{Hz}$. Details about streamer movement relative to the wave-motion can be found in Elboth et al. (2009b). The frequency of hydrostatic pressure variation is thus normally limited to the $0 - 1\,\mathrm{Hz}$ band. Since this frequency band does not contain much useful seismic data, hydrostatic pressure variation noise can be removed with a simple low-cut filter.
Fig. 6.1(a) shows the results of applying a $10\,\mathrm{Hz}$ low-cut filter with the objective to remove swell noise. Notice all the seismic information that is present in the difference plot at the bottom of this figure. This illustrates the limitation of frequency filtering for swell noise removal.

Prediction filtering

Fx-prediction filtering was introduced by Canales (1984). A number of improvements and extensions have been published since then, see for example Gulunay (1986), Wang (1999), and recently Gulunay (2008). In prediction filtering Wiener filters are used to approximate the underlying signal. The method performs well for removing some types of incoherent noise. However, it is not amplitude preserving. A specific problem is that prediction filters affect signals that do not appear along a straight line, commonly found in areas of complex geology. Fig. 6.1(b) shows the after and difference plots obtained by applying fx-prediction filtering to the same shot gather as used in Fig. 6.1(a). The results are not good. Large amounts of valuable seismic information can be seen in the difference plot, amplitudes are not preserved, and the swell noise is only partly attenuated.
It might be argued that it is not fair to apply fx-prediction on a shot gather, as this is not an optimal domain for this method, or that better results could have been obtained by applying the prediction filter in smaller windows. This is in fact also our experience, and as discussed later in this article, fx-prediction filtering and time-frequency de-noising can be combined to give good results.

Radon/τ-p transforms

Radon-based transforms in combination with muting are commonly applied for de-noising. The concept rests on the idea that the noise and signal components separate in the Radon or τ-p domain due to different move-out behavior (dip and/or curvature) in the time domain. The noise

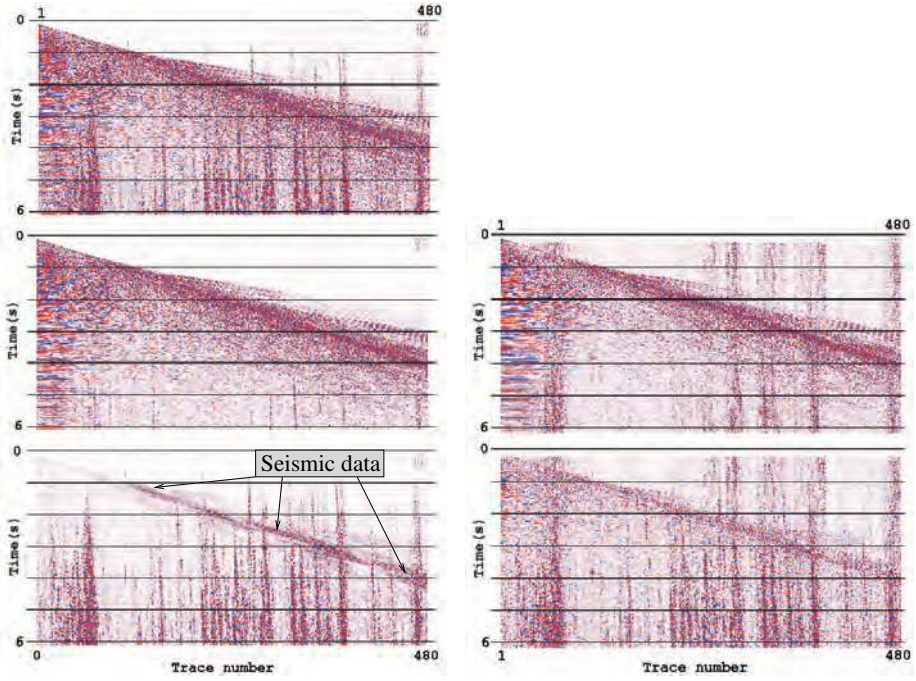

(a) (b)

Figure 6.1: Image a): From top to bottom: Before, after, and difference plot of applying a 10 Hz low-cut filter to a 6 s, 480 trace seismic shot gather with lots of swell noise. Image b): Top image: Results of applying fx-prediction filtering to the shot gather seen in the top image of Fig. 6.1(a). Bottom image: The difference plot.

component can then be muted or attenuated before the data is transformed back, or the noise component is transformed back and then adaptively subtracted from the gathers. Later in this article we will give an example where a τ-p transform has been combined with time-frequency de-noising to successfully remove seismic interference noise.

Wavelets

Wavelet transforms have successfully been applied to removal of ground-roll (Deighan and Watts, 1997), and as a method for more general de-noising (Miao and Cheadle, 1998).
Ground-roll has a distinctive character in both the time-space and frequency-wavenumber domains. Whichever domain we choose, we loose some useful, distinguishing characteristics of the ground-roll noise. 2-D wavelet transforms provide a 'compromise' domain (a t-x local f-k domain). We can separate noise and signal of similar dips provided they have different positions in time-space, and vice-versa. Clearly, a compromise implies that we weaken the resolving power in both time and frequency. This is a disadvantage of the wavelet domain. In addition the optimal selection of processing parameters within the wavelet domain is arduous and unattractive. An alternative method for exploiting the wavelet domain is to apply thresholding in order

to attenuate random noise (Yu et al., 2004; Ulrych et al., 1999). Curvelets, which can be thought of as 2-D oriented wavelets, are promising as they can provide a sparse representation of seismic events allowing for clean severing of the noise component. Thus, they are also suitable as a domain in which to match a multiple estimate (for example, as output from the Surface-Related Multiple Elimination {SRME} process) to the actual recorded multiples (Herrmann, 2004).

Stacking

A final form of de-noising is stacking. Uncorrelated noise will dampen during group forming as $1/\sqrt{n}$, where n is the number of independent traces. From this expression it is clear that the more traces (larger fold), the better the signal-to-noise ratio (SNR). However, there is a problem in that some types of noise have very large amplitudes compared to the underlying signal. In these cases, stacking might not be sufficient to attenuate the noise. Moreover, during processing it is normal to perform most of the processing steps prior to stacking. To get good results from algorithms such as SRME or pre stack migration, the pre-stack gathers therefore need to be fairly noise free.

6.2 Method - and initial assessments

This section provides an algorithmic description of a time-frequency de-noising (TFDN) algorithm. The general idea behind TFDN is widely known, and most seismic contractors offer some variants of this approach in their processing. However, TFDN seems to have received less attention than many of the other de-noising algorithms mentioned in the previous section, and its full potential for use in de-noising has probably not been fully realized.
Two relevant background publications for our time-frequency de-noising algorithm are given by Anderson and McMechan (1989) and Partyka et al. (1999) who address noisy trace identification/editing and short window Fourier transforms, respectively. The combination of these two techniques form the basis for TFDN. Herkenhoff et al. (2004) also describes a related de-noising algorithm that only differs in the way noise is identified. More recently Stein and Langston (2007) presented a similar algorithm applied to suppress certain types of noise in land data, while Bekara et al. (2008) presented an application tailored for swell noise attenuation.

Time-frequency de-noising (TFDN) works by applying a sliding window, both in space and time. A spectral estimate of all traces segments within this window is first computed[1]. The amplitude estimate at each frequency is subsequently compared with an amplitude estimate of a presumably reliable trace segment within the sliding window. If the amplitude is larger than a user-supplied threshold times the presumably reliable one, the amplitude in question is attenuated to the level of the presumably correct trace segment. This process is repeated for all frequencies specified by the user. The modified spectrum is finally transformed back to the time domain, and the process is repeated for each sliding window. The algorithm is illustrated in Fig. 6.2.

The parts of the frequency spectrum that are affected by noise are thus not simply removed. Instead, we try to predict what the actual amplitude of the affected frequency should have been,

[1]Note that we use the frequency domain as an example. In fact, other transforms can be equally suitable.

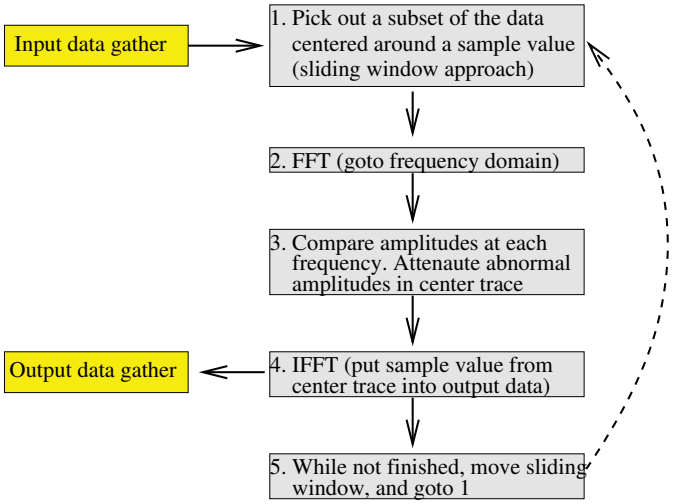

Figure 6.2: Illustration of a time-frequency de-noising algorithm.

based upon a spectral estimate of a reliable trace in its neighborhood. Because of the use of sliding windows, time-frequency de-noising is a localized method, and since it is data-driven, it is also adaptive. With the correct parameter settings it will only remove data with abnormal amplitude levels at certain frequencies and certain locations, and leave everything else unchanged. time-frequency de-noising is therefore principally amplitude preserving; i.e., it does not affect traces that statistically are determined to be reliable. This means that the algorithm can be applied to almost any dataset, with no negative effects.

In a production environment where tera-byte size data need to be de-noised, this aspect of time-frequency de-noising is important as it keeps user intervention at a minimum once the module parameters have been chosen. Conceptually, the fairly simple TFDN algorithm is situated somewhere between a normal band-pass filter and a more complicated wavelet transform approach.

6.2.1 Choice of threshold

An important part of the time-frequency de-noising (TFDN) algorithm is how it determines if an amplitude at a given frequency is to be attenuated or not. This is done by comparing amplitudes of neighboring traces within a sliding window. In noise-free data, amplitude variations between neighboring traces depend largely on the subsurface geology, and are typically small. However, many common types of noise are characterized by having large amplitudes at certain frequencies and certain spatial locations. Fig. 6.3 shows amplitudes of 50 neighboring traces, at 6 Hz, found in the shot gather seen in the top image of Fig. 6.1(a). The amplitudes vary by at least two orders of magnitude within each window. All the large and abnormal amplitudes are caused by swell noise. Below, a number of strategies for identifying and attenuating abnormal amplitudes

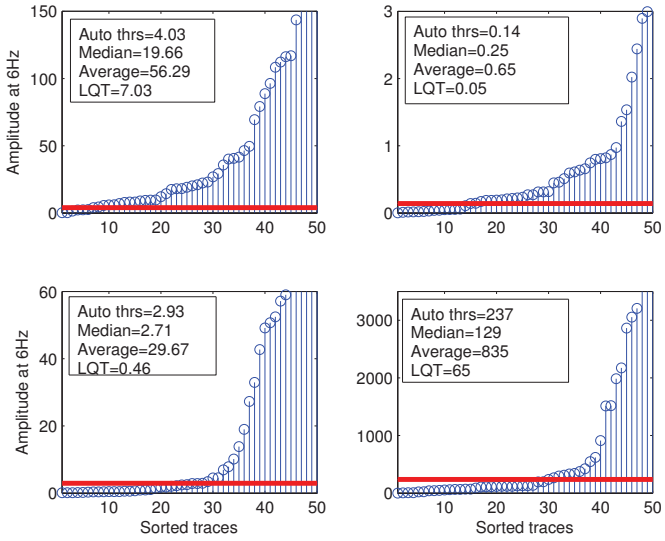

Figure 6.3: Results of different thresholding strategies applied different places to the shot gather seen in the top image of Fig. 6.1(a). Note that this dataset is heavily contaminated by swell noise, and that a t^2 gain has been applied to the data. The amplitudes were found at $6\,\mathrm{Hz}$, and 50 neighboring traces were considered. The horizontal line shows the threshold found by the automatic algorithm.

are discussed.

The median

A simple, fast, and reliable alternative is to compare amplitudes found in the central trace in the sliding window with the median amplitude found at the same frequency among all the traces. If less than 50% of the traces in the window are affected by noise, the median will represent a reliable, noisefree recording.

The lower quartile

Another simple, fast, and reliable option is to use the lower quartile as a reference for a noise-free amplitude. This option is useful if there are many noisy traces. It only requires that 25% of the traces in a window be noise-free to give good results.

The average

To compute the average amplitude, and then to use this as a threshold is normally not a recommended approach. The problem is related to abnormally large amplitudes, which often make an average estimate biased. A trimmed average (by first removing some of the largest amplitudes)

might be a better option. Experiments with real seismic noise have shown that the median or the lower quartile gives better and more robust results than the average.

Automatic threshold

In Bekara et al. (2008), a statistical technique for high amplitude noise detection was proposed. The technique considers the noise problem from an outlier detection perspective. The theory is that samples within a dataset will fall into either valid signal (regular), or noise (outliers). In statistical terms, data is categorized into n subpopulations, commonly referred to as Finite Mixture of Models. The method employs an adaptation of an algorithm presented in Hasselblad (1969). This algorithm separates outliers from regulars through an iterative procedure. Although reliable, it is also computationally demanding, and requires running times up to 10 times longer than that required by a simple median, or lower quartile. However, good results can be obtained.

Super trace

We have investigated the use of a new method called the super trace approach. First, the idea is to compute and sort the energy of all traces in a sliding window. Second, traces that are considered noise-free (below the median or lower quartile energy) are correlated and shifted up or down, before they are stacked. Only traces that correlate well are used in this stacking procedure. Finally, when comparing amplitudes in the frequency-domain, amplitudes are compared with those found in the stacked super trace, instead of the median, lower quartile, average or automatic trace, respectively. This approach ensures that the reference trace has a good SNR (it is a result of stacking), which is physically appealing. As with the automatic threshold option, a drawback is that this approach is computationally intensive. Also, conflicting dips could potentially cause problems during the stacking part of this algorithm, unless dip-moveout correction is applied apriori. Fig. 6.4 shows the number of traces the algorithm uses during its stacking phase when a window width of 51 traces was used.

Iterative fx

The last method we consider here is one that combines time-frequency de-noising (TFDN) and fx-prediction filtering in an iterative approach. When a noisy trace segment (sample) is identified by TFDN, the iterative fx approach applies fx-prediction in a sliding window surrounding the noisy trace segment. The output of the fx-prediction is then used to replace the noisy trace segment identified by TFDN. We have found that the best results from the fx-part of the algorithm are obtained by using a somewhat larger window (in space and time) than the window used by the TFDN part of the algorithm. Testing has indicated that an optimal window size for the fx-part is 100-200 traces wide and typically $1\,\mathrm{s}$ (assuming $4\,\mathrm{ms}$ sampling rate). This feature distinguishes our algorithm somewhat from the algorithm proposed by Schonewille et al. (2008), where it seems that both TFDN and fx-prediction are applied within the same sliding window. Unlike normal fx-filtering, this approach is amplitude preserving. Only noisy data are changed, while all good data are left intact. The drawback is its complexity, making it computationally expensive.

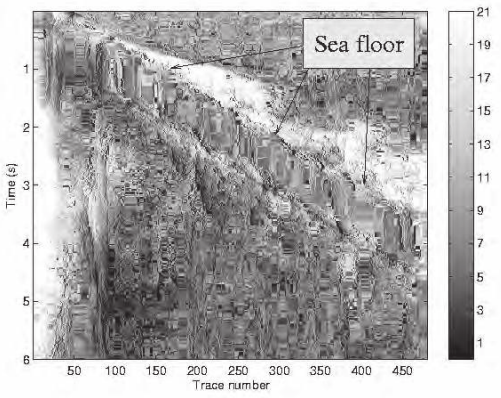

Figure 6.4: Plot that uses gray-scales to indicate the number of traces used by the super trace method to build up a master trace. (This is from the same shot gather as Fig. 6.1(a).) Note that the number of traces used in the stacking clearly depends on the SNR.

6.3 Results

In Fig. 6.3, the thresholds found by the different methods are compared. Generally, it seems like in cases of medium to large amounts of swell noise, the median, lower quartile, and the automatic methods give comparable results. The estimates provided by the average approach are consistently too high. Through experiments, not shown here, the super trace approach gave results that were comparable with the median, lower quartile, or the automatic option.
In Fig. 6.5, the threshold methods are applied to a seismic shot gather in order to visually compare them. During all processing, 51 traces were used in a horizontal sliding window. The aim was to remove as much noise as possible without simultaneously affecting the seismic reflection signal. Experience has shown that time-frequency de-noising should be repeated (3-7 iterations) to get optimal results. Images b and c in Fig. 6.5 show results of using the simple lower quartile option on a shot gather. Images d and f show the results of the automatic threshold and the iterative fx options. Generally, the results are similar, and only small differences are visible. Nevertheless, the iterative fx option has removed both slightly more noise, and coherent energy, compared to the two other options. A problem with the super trace approach, not shown here, is that it tends to remove too much energy from the region close to the ocean bottom. This is probably because it uses the traces with the least energy to build up a reference trace. The super trace algorithm is therefore better suited to be applied in domains where all events are relatively flat, e.g., a common-offset section or an NMO-corrected CDP gather. In its current form we do not recommend its usage on shot gathers.
In the remaining part of this section further results from de-noising of seismic data are presented. The objective is to show how the choice of proper domains for the application of time-frequency de-noising can result in very good de-noising results. The results were all obtained by using the median or the lower quartile option for threshold determination.

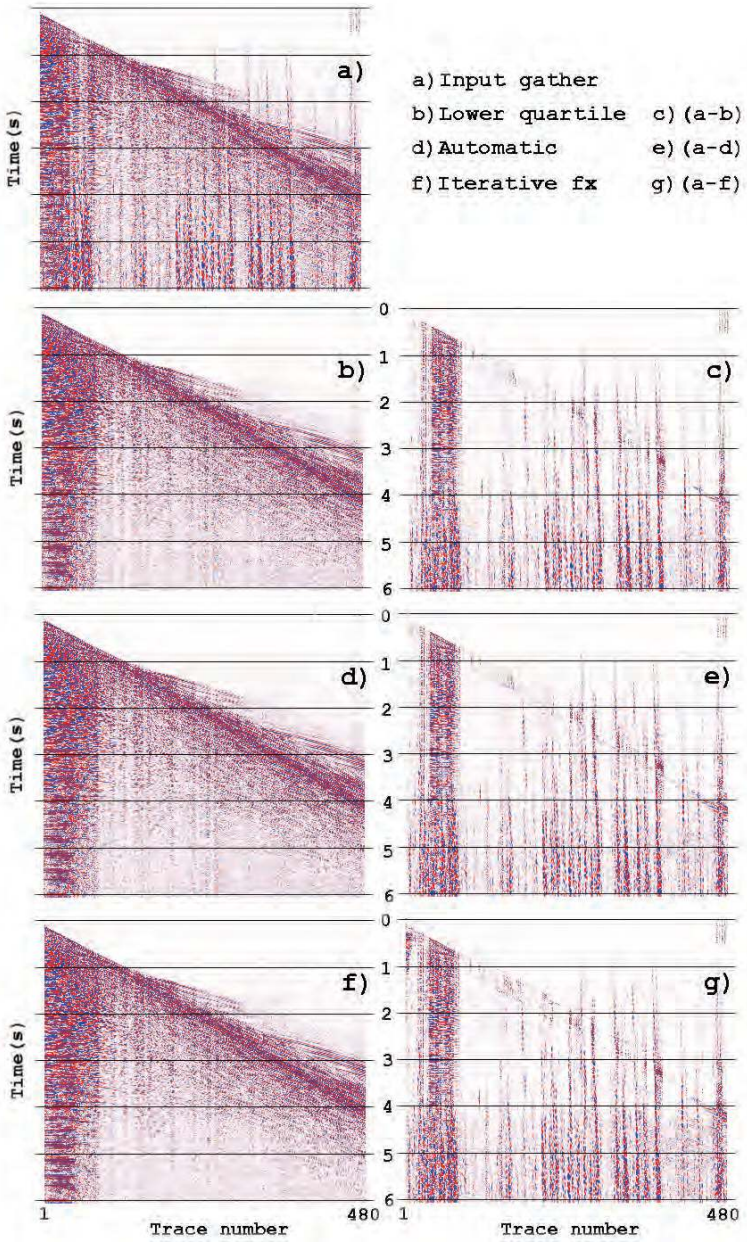

Figure 6.5: Top left image: The original input shot gather. Image b) and c): After and difference plot from using the lower quartile to remove noise. Image d) and e): After and difference plot from using the automatic threshold option. Image f) and g): After and difference plot from using the iterative fx option. The results appear very similar.

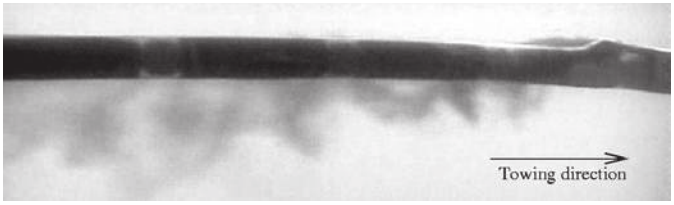

Figure 6.6: Snapshot of the turbulent boundary layer surrounding a $5\,\mathrm{cm}$ thick seismic streamer cable in the ocean. An environmentally friendly dye is released from the cable surface to reveal structures in the turbulent boundary layer.

6.3.1 Swell noise

Swell noise is high amplitude noise that normally contains frequencies from $2 - 10\,\mathrm{Hz}$. It usually affects a number of neighboring traces, and can be observed in seismic data as vertical stripes or 'blobs' as shown in Fig. 6.5. Two different mechanisms create swell noise. On fluid filled streamer the cable motion can induce transversal waves (so-called bulge waves), described by Peacock et al. (1983), Bjelland (1993), and Dowling (1998). Bulge waves are known to generate high amplitude noise up to around $10\,\mathrm{Hz}$. Modern foam filled seismic cables are less troubled by such bulge waves. However, there is also a second swell noise producing mechanism. From equation 6.1 it is apparent that waves can induce a cross flow over the streamer. Cross flow can also be induced by ocean currents. Experiments by Bull and Dekkers (1993), Heenan and Morrison (2002a,b), and Snarski (2004) indicate that the flow characteristics in the turbulent boundary layer surrounding long cylindrical objects like seismic streamer cables will change when the local angle between the streamer and the flow direction exceeds approximately $6°$. Instead of having a symmetrical turbulent boundary layer, an increased angle will result in an unsymmetrical boundary layer where vortex shedding can take place. Vortex shedding is an unsteady flow phenomenon where vortices are created and detached with a period that depends on the local flow conditions. This creates strong alternating pressure fluctuations that will be observed as high amplitude swell noise. Fig. 6.6 is a snapshot of a seismic cable in the ocean, where a colored dye is released to visualize the turbulent nature of the flow around this streamer cable.

As already mentioned, swell noise typically covers a large number of neighboring traces, and appears as 'blobs' with large amplitudes in the data. It can often be difficult to find a noise-free reference trace in a sliding window that passes over such a 'noise-blob'.

A prerequisite for effective attenuation of swell noise is therefore to break it up, and randomize it. This can be achieved by sorting the data to the common-offset or the CDP domain. Time-frequency de-noising is then applied in these domains, before the data is sorted back for further processing. Fig. 6.7 shows the results of applying time-frequency de-noising to remove the influence of swell noise in these domains. Note that all the swell noise has been removed in the right image. In order to appreciate the effects of swell noise removal, we look at the effect it can have on the quality of a stacked section. Fig. 6.8 illustrates that time-frequency de-noising, applied on pre-stack data, clearly improved the quality of this stack.

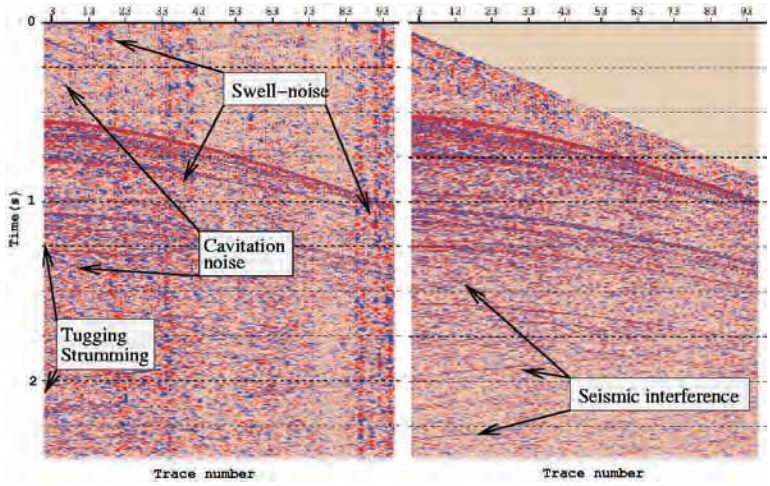

Figure 6.7: Seismic shot gather cleaned from swell noise by applying time-frequency de-noising in the shot, CDP and common-offset domains. Notice also that the tugging noise, seen on the first traces, as well as some cavitation noise have been attenuated by the same step.

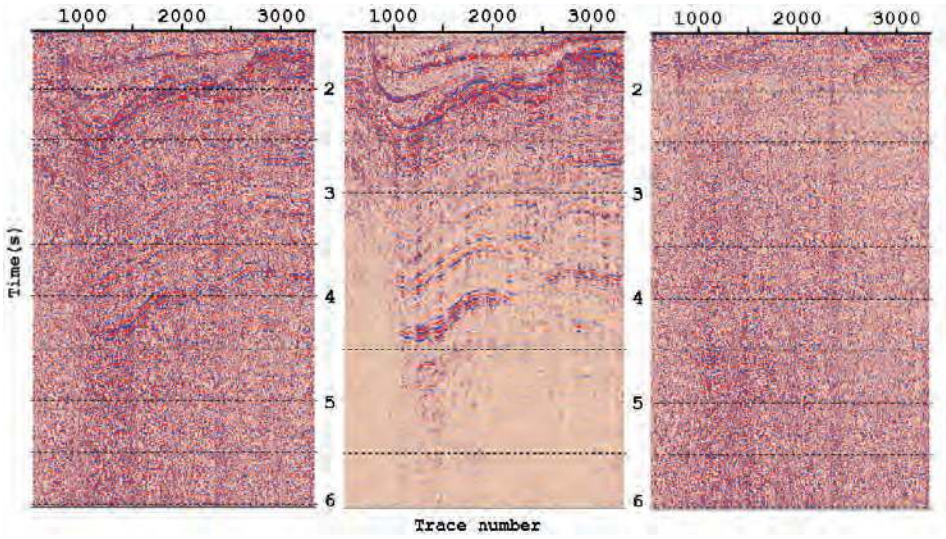

Figure 6.8: Left: original stack between 1.5 and 6 s. Middle: stack after application of prestack de-noising. Right: difference plot. Notice that very little seismic information is visible in the difference plot.

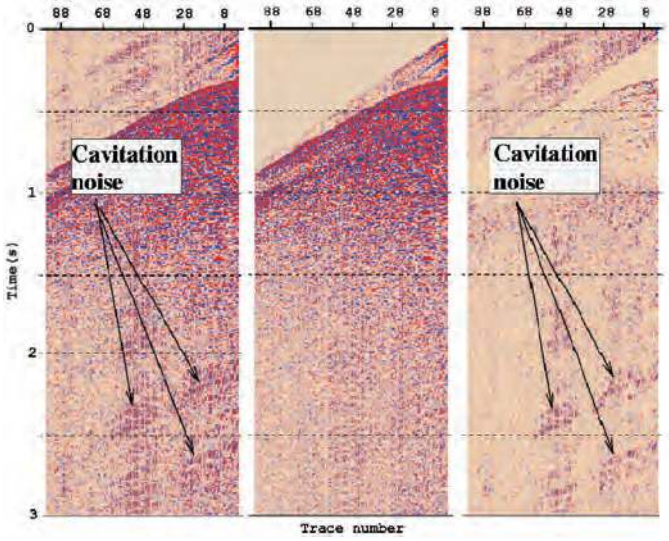

Figure 6.9: A 3 s 96 trace shot record. From left to right: Before, after, and difference plot of a typical shot record after the application of time-frequency de-noising. A 4 Hz low-cut filter was applied to the data to remove the influence of swell noise.

6.3.2 Cavitation noise

As propeller blades move through a fluid, low-pressure areas are formed as the fluid accelerates around and moves past the blades. If these low-pressure areas reach vapor pressure, the fluid vaporizes and forms small bubbles of gas. This is cavitation, which normally takes place when the combination of propeller speed, angle, and load is wrong. According to Brennen (2005), the time varying component of the far-field pressure p_a, resulting from the collapse of a spherical bubble, can be approximated by

$$p_a = \frac{\rho_L}{4\pi R}\frac{d^2V}{dt^2}. \tag{6.2}$$

Here, ρ_L denotes liquid density and R is the distance from the location of the cavitation to the measurement point. The term $V(t)$ is the time varying volume of the collapsing bubble. A number of effects like temperature, compressibility, turbulence, and evaporation have been neglected in equation 6.2. Nevertheless, in a collapsing bubble the d^2V/dt^2 term can become very large and typically trigger strong local shock-waves manifesting as noise in seismic recordings. Cavitation noise from an experimental seismic survey recently acquired on the Norwegian continental shelf can be seen in the left image in Fig. 6.9. The processing applied to remove this noise was very similar to the one applied to remove swell noise described above. The idea was to break up and randomize the cavitation noise, by sorting the data to the CDP and common-offset domains, and then apply time-frequency de-noising (TFDN). There was nevertheless one important difference; swell noise is normally band-limited to 2-10 Hz, while cavitation noise is broad banded. The results seen in Fig. 6.9, taken from Elboth et al. (2009a) was obtained by applying TFDN all the way up to the Nyquist frequency.

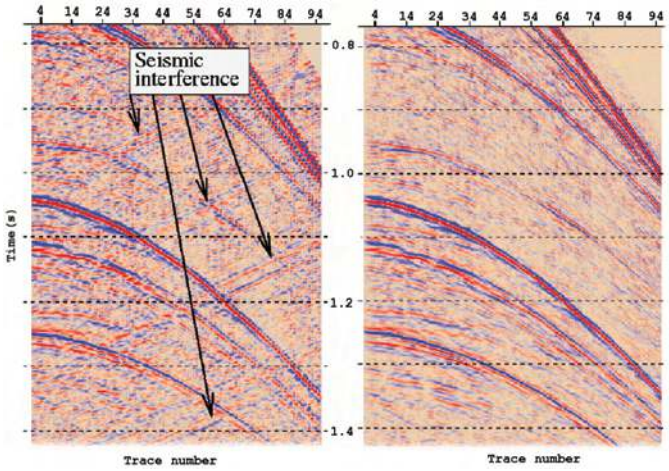

Figure 6.10: Part of a shot gather before and after seismic interference removal. Notice how the seismic interference (the stripes going from lower left to upper right in the left image) has been attenuated in the right image. (This data is a zoom taken from the right image of Fig. 6.7.)

6.3.3 Seismic interference

This sub-section gives a novel example of seismic interference noise removal. In the left image in Fig. 6.10, interference noise can be observed as stripes. Such noise is broad banded, and can often have large amplitudes compared to subsurface reflection data.

A common approach for removing seismic interference is to take advantage of its different move-out behavior(dip and/or curvature) compared to reflection data. When transformed to the Radon or τ-p domain, seismic interference will often map into an area that can be muted. he problem in this data was that the move-out of the seismic interference was close to that of the seismic reflection signal. Traditional muting was therefore not optimal. Another approach used for seismic interference attenuation is variants of fx-prediction filtering. Gulunay et al. (2004) and Gulunay (2008) discuss a number of such algorithms. The general idea is to suppress seismic interference by sorting it into a domain where it is random, compared to the reflection signal, and apply fx-prediction filtering. This approach could also work for our data. However, the geology in the area where the data was acquired contains a number of dipping features. Such features could also be easily removed by prediction filters. It was therefore decided to investigate another seismic interference removal approach that included the use of time-frequency de-noising.

The left image in Fig. 6.11 shows the shot gather from the left image in Fig. 6.10 transformed into the τ-p domain. The 'blobby' area that stands out is caused by interference from a vessel with a shot point interval of around $10\,\mathrm{s}$. Our data was acquired with a shot interval of $4\,\mathrm{s}$. When the τ-p gathers were sorted to the 'common-slowness domain[2]', less than half of the traces were therefore affected by seismic interference.

[2]A common-slowness gather is one that contains the same ray from several τ-p gathers. Conceptually, they relate to τ-p gathers the same way as common-offset gathers do to shot gathers.

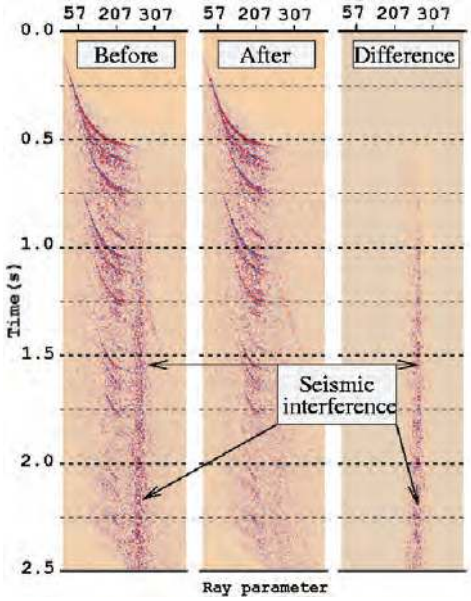

Figure 6.11: From left to right: Before, after, and difference τ-p shots from de-noising. Notice the vertical noise train caused by seismic interference. It is removed by time-frequency de-noising. (This is again data from the same shot gather as the right image in Fig. 6.7.).

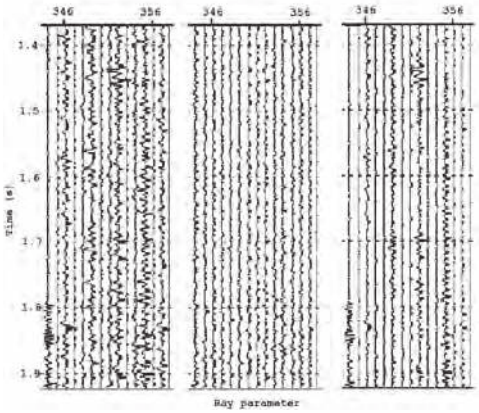

Figure 6.12: Part of a typical slowness gather from the processed dataset. From left to right: Before, after, and difference plot of time-frequency de-noising applied to the gather. Notice that only traces affected by seismic interference are attenuated.

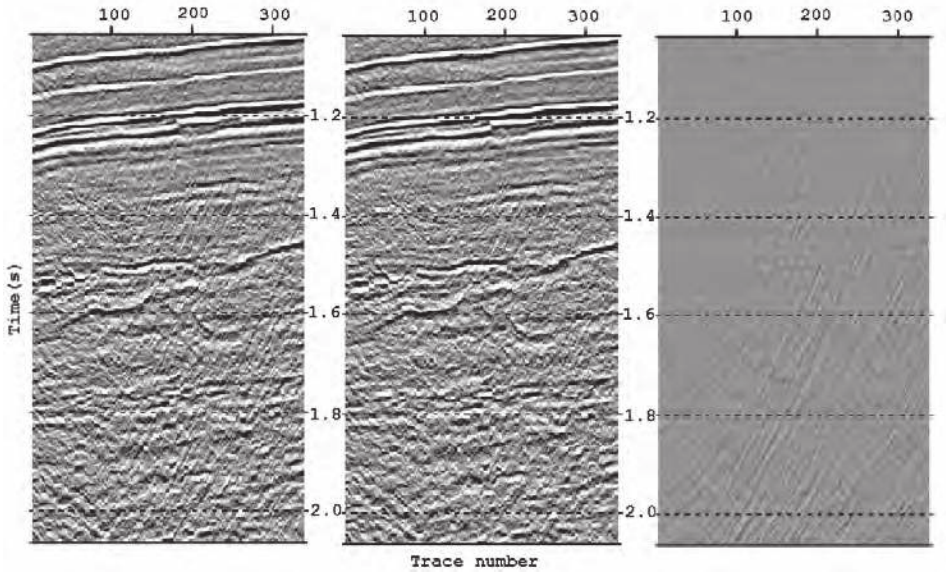

Figure 6.13: Part of a stack after de-multiple and migration. Left: After de-noising (excluding seismic interference removal). Middle: After de-noising (including seismic interference removal). Right: Difference. The de-noising were applied pre-stack.

Fig. 6.12 shows before, after, and difference plots of part of a typical common-slowness gather from this line. In the left image the traces (rays) that come from τ-p gathers affected by seismic interference clearly stand out. Time-frequency de-noising effectively attenuated the amplitudes of these noisy traces (rays) down to the level of the traces (rays) unaffected by seismic interference (middle image). The results of our novel seismic interference removal approach on a shot gather can be seen in the right image in Fig. 6.10. Notice how the interference has been attenuated in this image compared to the original data.
The final test of our seismic interference de-noising is to compare stacked data, after de-multiple and migration. The middle image in Fig. 6.13 shows part of the stack after all de-noising, including the new seismic interference removal approach. The quality is acceptable. The left image show the same data, without the seismic interference removal approach. The problem seems to be that the high-energy seismic interference noise was smeared out by the migration, and appears as strongly dipping events all over the data. The right image shows the difference plot. Clearly, the quality of the final product was significantly improved by our seismic interference de-noising.

6.3.4 Tugging and strumming noise

This last example is concerned with tugging and strumming noise, caused by sudden vessel movements and vibrations from the lead-in cables. Strumming appears to be especially problematic on the outer streamer cables in a spread, when lead-in cables are dragged with an angle

compared to the flow direction. When this is the case, vibrations are induced by the Von-Karman vortices that detach when cross flow passes over the streamer cable. These vibrations can be reduced by making the lead-in cables more hydrodynamic, but they will never entirely vanish. Some strumming noise can be observed in the top image in Figures 6.5 and 6.7 as horizontal stripes on the first few traces. Even though strumming noise looks different from swell noise, it has approximately the same frequency content. During time-frequency de-noising swell noise removal, it is consequently also attenuated. This can be observed by comparing the plots in Fig. 6.7.

6.4 Conclusion

We have presented examples on how time-frequency de-noising (TFDN) can be applied to remove a number of common types of noise found in marine seismic data. Apart from being noisy, the data examples used are not in any way special. The de-noising results can therefore be considered as general, and it can be expected that TFDN will provide similar results on any seismic data affected by swell, cavitation, strumming, or seismic interference noise. It is also likely that some types of noise not discussed in this article, including noise types found in land data, also effectively can be attenuated by TFDN.

During marine seismic acquisition, vessels spend a considerable amount of time on weather standby and lines are often rejected due to excessive levels of swell noise. With efficient software de-noising, a number of such lines that are otherwise are deemed unsatisfactory, could probably have been accepted and processed. Consequently, with day rates (2009) of a modern seismic vessel in the order of several hundred thousand US dollars, there is a significant economical side to de-noising.

We have investigated different strategies for obtaining a threshold to decide if an amplitude in a frequency spectrum should be attenuated or not by time-frequency de-noising. Both the use of the median and the lower quartile approach appear to be good choices. The use of an automatic, a super trace, and a hybrid iterative TFDN/fx-prediction approach also works well. However, we are not sure if the potential benefits of these methods outweigh the fact that they require CPU-time that is an order of magnitude larger than the simpler median or lower quartile options. We are also interested in considering the phase information in future versions of our time-frequency de-noising. This could hopefully improve the algorithm further.

A number of time-frequency de-noising implementations are available within the seismic processing industry. However, based upon the number of published articles on de-noising, time-frequency de-noising has received little attention compared to many other de-noising algorithms. This is somewhat surprising, since, as shown here, time-frequency de-noising provides adaptive, robust, and high quality de-noising, with a rather simple underlying algorithm.

Chapter 7

De-noising seismic data in the time-frequency domain

Thomas Elboth <thomae@math.uio.no>
Fugro Geoteam AS, Hoffsveien 1c, P.O.Box 490 Skøyen N-0213 Oslo, Norway
Mechanics Division, Department of Mathematics, University of Oslo, Norway
Hamid Hayat Qaisrani <h.qaisrani@fugro.no>
Fugro Seismic Imaging AS, Hoffsveien 1c, P.O.Box 490 Skøyen N-0213 Oslo, Norway
Thomas Hertweck<thomas.hertweck@fugro-fsi.com>

Fugro Seismic Imaging, Horizon House, Azalea Drive, Swanley, Kent, BR8 8JR, UK.

Expanded abstract originally published as:
T. Elboth, H. Qaisrani, and T. Hertweck: De-noising seismic data in the time-frequency domain, SEG Technical Program Expanded Abstracts, 27(1) 2622-2626 (2008).

Abstract

Marine seismic data are quite often affected by noise. For successful imaging, it is crucial that as much coherent and incoherent noise as possible is removed in an early stage of processing. An effective method to handle a broad range of noise problems is a time-frequency de-noising (TFDN) algorithm. In this paper, we present background information on the physics of weather and flow noise generation on seismic streamers, some details regarding the implementation of a TFDN method, and three examples where it has been successfully applied to seismic data.

7.1 Introduction

Seismic data always consist of a signal and a noise component. What has to be considered as noise depends on the application. However, as a general definition we can say that any recorded energy which interferes with the desired signal can be considered as noise. The noise can be classified as background noise (for instance wind, swell, noise from nearby production, or interference from nearby seismic acquisition), source-generated noise (for instance direct and

scattered waves or multiples), and instrument noise and can show up as coherent or incoherent energy in seismic gathers. This diversity of noise types with different characteristics makes separation of signal and noise a challenging process. However, efficient noise attenuation and/or removal is important for high-quality imaging and from an economical point of view. Smith (1999) claims that costs associated with weather-induced delays can account for up to 40% of the total cost of a marine survey. Such delays usually occur when the wave heights surpass 2-2.5 meters, and swell noise reduces the resolution and accuracy of the seismic survey to an unacceptable level. Surely, in this paper we cannot address all the different types of noise. Therefore, in the following sections we focus on weather-induced flow and swell noise. We present three examples where a time-frequency de-noising method has successfully attenuated the noise and allowed for improved imaging.

7.2 Weather noise generation

Seismic streamers are operated in a highly complex fluid environment. Experiments and theory developed by Keith et al. (2005) and Furey (2005) show that streamers are surrounded by a turbulent boundary layer that grows from a few millimeters near the front to perhaps several decimeters near the tail, depending on the length of the streamer. In addition, a streamer is subjected to sea motion from waves and currents. Unsteady tugging motion by the towing system and lift from steering birds that try to maintain the streamer at a constant depth also add to the complexity of the flow environment. Experiments by Bull and Dekkers (1993), Heenan and Morrison (2002a,b) and Snarski (2004) indicate that the flow characteristics in the turbulent boundary layer surrounding long cylindrical objects like seismic streamers will change when the local angle between the streamer and the flow direction exceeds 6-15°. Instead of having a symmetrical turbulent boundary layer, an increased angle will result in an unsymmetrical boundary layer where so-called vortex shedding can take place. Vortex shedding is an unsteady flow where vortices are created at the back of the object in the stream. The vortices are then detached with a period that depends on the local flow conditions. This creates strong and broad-banded alternating pressure fluctuations near the streamer that will be observed as high-amplitude noise in seismic recordings. Piecewise vortex shedding from a seismic streamer at 7-8 meters depth can probably occur when the surface wave-heights exceed 2-3 meters, see Elboth et al. (2009b). This can explain some of the noise observed in Figure 7.1. In situations of strong side-currents, a more continuous vortex shedding environment is likely. This can be observed in Figure 7.2 where noise from vortex shedding and tugging noise from the vessel can be observed. This kind of noise is broad-banded and has very large amplitudes compared to the seismic reflection signal.

Another kind of weather noise comes from the low-frequency hydrostatic pressure fluctuations originating from the wave-induced vertical motion of the ocean. This component has frequencies comparable to ocean swells, which are well below 1Hz, and can simply be filtered out during normal processing. However, vertical streamer motion can on some occasions induce transversal waves (so-called bulge wave), especially within fluid-filled streamers. This is described by Dowling (1998). Bulge waves are known to generate high-amplitude noise up to around 10Hz. It is the combination of bulge-wave noise and the vortex-shedding noise described

above that usually is referred to as swell noise. The amount of bulge-wave noise versus vortex-shedding noise depends on the flow conditions as well as the equipment used. However, both noise types typically produce amplitudes that are an order of magnitude or more larger than the typical seismic reflection signal. In most cases seismic acquisition is suspended when the noise level exceeds a predetermined level. However, occasionally the data acquisition is continued despite of the weather conditions and seismic data processing has to deal with all noise problems later on. Such surveys with high noise levels present a significant challenge and opportunity for the processing geophysicist to get the most out of existing de-noising algorithms.

7.3 De-noising algorithms

There is no single algorithm that can remove all types of noise in seismic gathers. It is rather the combination of a number of different techniques, each adapted to the specific problem at hand, that will lead to optimal de-noising results. The general approach of almost all de-noising methods is that they transfer the data to a domain where the signal and the noise component can be separated. The presumed noise is subsequently removed, before the data component is transformed back to normal physical t-x space. Thus, the challenge is to find a domain where the noise and the signal are well separated. Below we will briefly describe some de-noising algorithms that are relevant for the examples that will follow later in this article. A full algorithmic description is only provided for a TFDN algorithm that is used in all the examples.

Prediction filtering was introduced by Canales (1984). A number of improvements and extensions have been published since then, see for example Gulunay (1986), Wang (1999) and recently Gulunay (2008). Prediction filtering works by using Wiener filters to obtain a least squares approximation of the underlying signal. The method performs well when used to remove some types of incoherent noise. Unfortunately it is not amplitude preserving.

Radon-based transforms in combination with muting is another powerful de-noising approach. The idea is that noise and signal components separate in the Radon or τ-p domain due to different move-out behavior (dip and/or curvature) in the time domain. The noise component can then be muted before the data is transformed back to normal t-x space, or the noise component is transformed back and then adaptively subtracted from the gathers.

Wavelet transforms have had successful application to the removal of ground-roll, Deighan and Watts (1997), and more general de-noising, see Miao and Cheadle (1998). Ground-roll has a distinctive character in both the time-space domain and frequency-wavenumber domain. Whichever domain we choose, we lose some useful, distinguishing characteristics of the ground-roll noise. 2D Wavelet transforms find a 'compromise' domain (a t-x local f-k domain). We can separate noise and signal of similar dips if they have different positions in time-space, and vice-versa. Clearly, a compromise means we weaken the resolving power in both time and frequency. This is a disadvantage of the Wavelet domain. Also the optimal selection of processing parameters within the Wavelet domain is arduous and unattractive. An alternative method for exploiting the Wavelet domain is thresholding to attenuate random noise, see Yu et al. (2004)

and Ulrych et al. (1999). Curvelets can be thought of as 2D-oriented wavelets. They are promising as they provide a sparse representation of seismic events (optimal in a sense) allowing for clean severing of the noise component.

Time-frequency filtering (TFDN) is an important and versatile approach for seismic data de-noising. It is well suited to remove weather-related noise with large amplitudes. Normally this algorithm is applied to pre-stack data. TFDN works by using a sliding window, both in space and time. A spectral estimate of all traces within this window is first computed. Note that we use the frequency domain as an example. In fact, other transforms can be suitable equally well. The amplitude estimates at each frequency are then compared with the amplitude estimate of a presumed good trace within the chosen window. If the amplitude is larger than a user-supplied threshold factor times the presumed good amplitude, the amplitude in question is attenuated to the level of the presumed correct trace. This process is repeated for all frequencies specified by the user. The modified spectrum is finally transformed back to the time domain, and so on for each sliding window. In this way, we do not simply remove the parts of the frequency spectrum that are affected by noise. We also try to predict what the actual amplitude of the affected frequency should have been, based upon a spectral estimate of a presumed good trace in its neighborhood. In principle, not only the amplitude spectrum but also the phase spectrum can be utilized. Because of the use of sliding windows, TFDN is a quite localized method. At the same time the procedure is data-driven and thus adaptive. With the correct parameter settings it will only remove data with abnormal amplitude levels at certain frequencies and certain locations and leave everything else unchanged. TFDN is therefore in most cases amplitude preserving, i.e. it does not affect traces that are determined to be good. This means that the algorithm can be applied to almost any dataset, with few negative effects.
In a production environment where a geophysicist might have to de-noise Tera-bytes of data in a work-flow, this is important as it keeps user intervention at a minimum once the module parameters have been chosen. The processor can simply focus on the quality control of the application. Conceptually, a TFDN algorithm is fairly simple and situated somewhere in between a normal band-pass filter and a more complicated wavelet transform approach.

7.4 Data examples

7.4.1 Seismic shot gather

The first data example in Figure 7.1 shows a shot gather from a recently acquired seismic survey. It was recorded by using a 6km fluid-filled seismic streamer in 2-2.5 meter swells and suffers from significant swell-noise. The data were de-noised by means of the time-frequency algorithm described above. In order to remove swell-noise only, it is usually sufficient to apply the algorithm in the 0-15Hz frequency range. Note that the abnormal amplitudes found in the swell-noise have almost completely been attenuated by the algorithm. Very little actual seismic signal can be seen in the difference plot.

7.4.2 Seismic 2D line

The second data example in Figure 7.2 and 7.3 is from a recent seismic survey acquired by a vessel carrying an 8km fluid-filled streamer. The data presented are from a line that was recorded during fairly large waves/swell, and with some side-currents. On a number of shots we can observe swell-bursts, similar to those seen in Figure 7.1. In addition, the currents and the vessel turning caused a significant feathering angle. This resulted in a high incidence angle between the streamer and the flow direction. It is likely this led to the broad-banded and high-amplitude vortex shedding noise observed. As a result of the unsteady towing conditions, there was also significant tugging noise present from the vessel and lead-in cable.

Figure 7.2 shows a typical shot-gather from this line. The influence of noise in prestack gathers will be reduced when the data are stacked. Assuming incoherent (Gaussian) noise, abnormal amplitudes will be attenuated by a factor of $1/\sqrt{N}$, where N is the number of traces used in the stacking. However, as observed in Figure 7.2, some of the noisy amplitudes in the prestack gathers are very large. This means that the noise will still be present in the stack. To obtain optimal results, pre-stack de-noising therefore needs to be performed. In Figure 7.3 the same stacked section with and without de-noising is plotted. Most of the noise has been removed with prestack time-frequency filtering (TFDN), applied both in the shot and in the CMP domain. In addition, $\tau - p$ muting was applied to attenuate the dipping noise originating from the lead-in cable. In the lower section, we tried to apply FX prediction filtering. However, this was found to have a negative effect on dipping geological features, and was therefore dropped. The result of the de-noising was a reasonable stack, even though some of the shot gathers had very low quality.

7.4.3 Ocean Bottom Cable (OBC) de-noising

The last de-noising example is taken from a survey that was acquired by using a combination of hydrophones and geophones at the bottom of a lake. In Figure 4 some of the geophone records are shown. The objective of the processiDeng was to improve the signal-to-noise ratio of these records such that they could be used to de-ghost the hydrophone records. The geophone data suffered from severe noise problems that were probably caused by poor geophone coupling to the lake bed and possible electrical problems on the cable and/or recording instruments. This resulted in huge spikes, see left image in Figure 4, that had to be removed by a de-spike algorithm. De-noising through the use of a TFDN algorithm was then applied to further suppress the noise. The result was a dataset with a reasonable quality as seen in image 3 in Figure 4, which allowed to get some success out of the project.

Conclusions

Time-frequency (TFDN) algorithms are effective tools to remove a variety of noise energy from seismic gathers. The technique combines the usability of a simple band-pass filter with the data quality that is close to what can usually only be achieved with much more complex wavelet- or curvelet-based algorithms. Furthermore, using a careful choice of processing parameters the method can be considered as amplitude-preserving and can be applied in a fully automatic way.

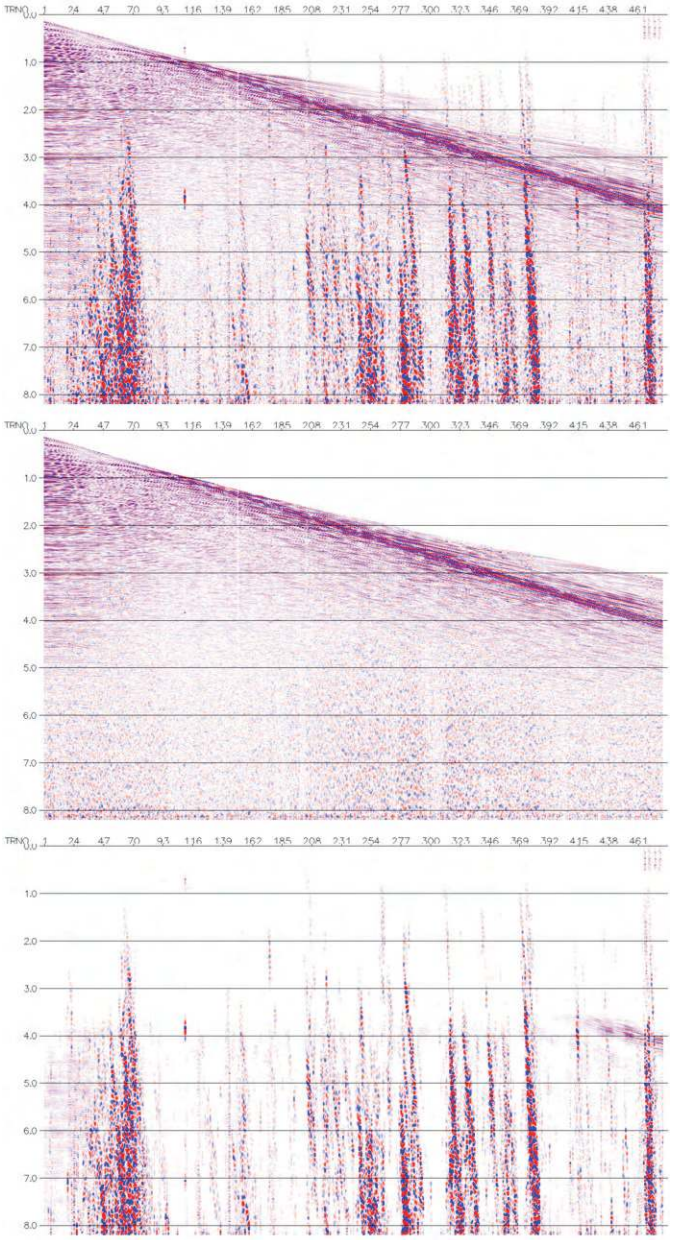

Figure 7.1: Top: original shot gather. Middle: shot gather after application of a time-frequency algorithm targeted to remove swell noise and spikes. Bottom: difference plot

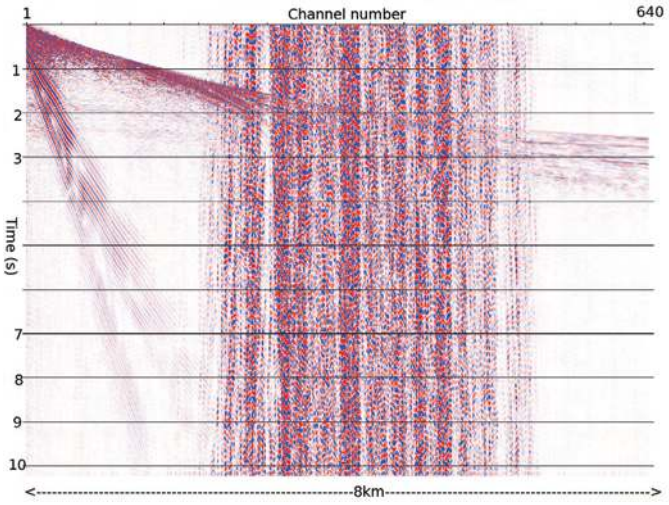

Figure 7.2: Shot gather from a line acquired with a significant feathering angle

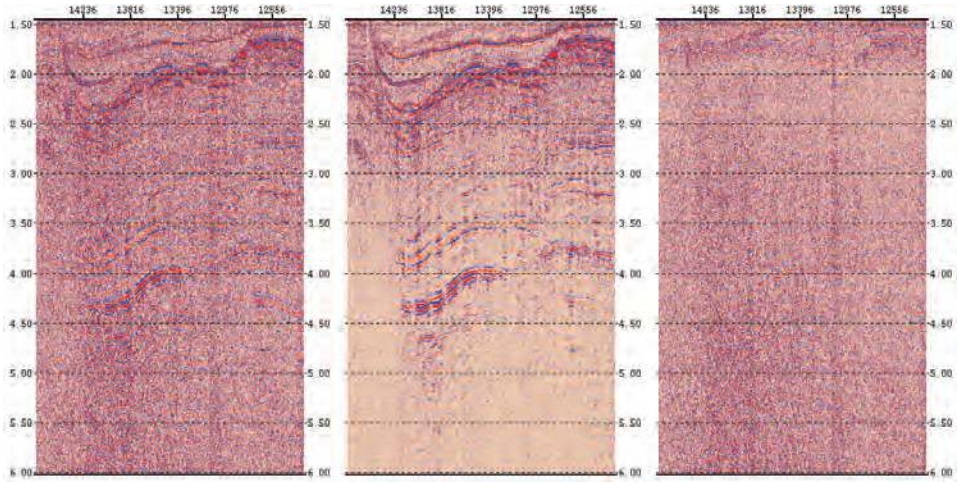

Figure 7.3: Left: original stack. Middle: stack after application of prestack de-noising. Right: difference plot

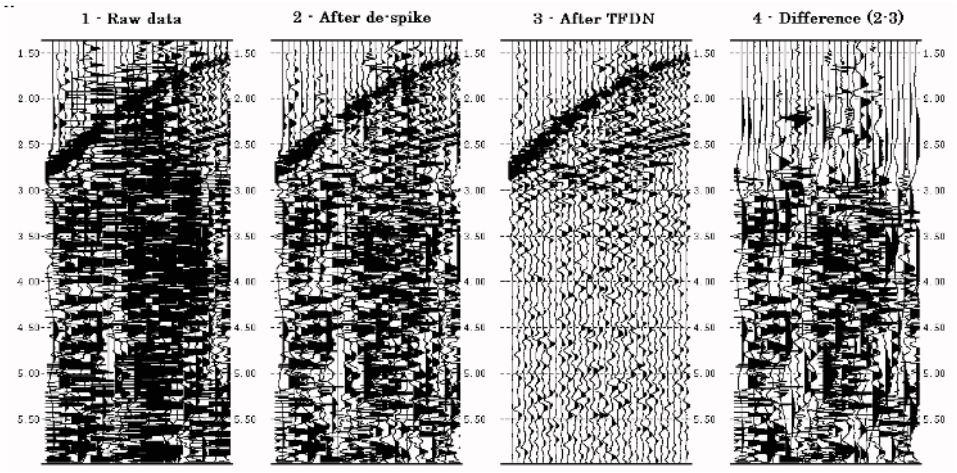

Figure 7.4: Traces from an OBC-survey. The left image shows the initial data with very large spikes. (Note that the wiggles have been clipped). The three next images show the data after de-spiking. Left and middle: data before and after application of time-frequency de-noising. Right: difference plot from the time-frequency de-noising.

Other techniques usually require more adaption to the specific noise problem at hand. This makes the TFDN method a general tool to significantly improve the data quality in both the prestack and post-stack domain and allows for more successful imaging.

Chapter 8

Attenuation of noise in marine seismic data

Thomas Elboth <thomae@math.uio.no>
Fugro Geoteam AS, Hoffsveien 1c, P.O.Box 490 Skøyen N-0213 Oslo, Norway
Mechanics Division, Department of Mathematics, University of Oslo, Norway
Dag Hermansen
Fugro Seismic Imaging AS, Hoffsveien 1c, P.O.Box 490 Skøyen N-0213 Oslo, Norway

Expanded abstract originally published as:
T. Elboth, and D. Hermansen: De-noising marine seismic: A case study, SEG Technical Program Expanded Abstracts, 28 (2009).

Abstract

This work presents how data from a marine seismic survey, heavily contaminated by noise, was de-noised through the use of a time-frequency filter. In addition to a fairly standard work flow designed to remove swell-noise, cavitation noise, and strumming noise, we introduce a new approach to tackle seismic interference. This is done by applying time-frequency de-noising on slowness gathers. As a background and motivation for the processing we also explain some of the physics behind the generation of the different noise types.
The end story is that rather low quality input data can be turned into high quality seismic sections. Even though only one data-set is used, the results and methodologies presented here are believed to be general, and should be applicable to a large number of seismic surveys.

8.1 Introduction

Seismic data always consists of a signal and a noise component. As a general definition we can say that any recorded energy which interferes with the desired signal can be considered as noise. The diversity of noise types often makes separation of signal and noise a challenging process. However, efficient noise attenuation and/or removal is important for high-quality imaging. From an industrial point of view it is also desirable that de-noising algorithms should work on

many types of similar noise without the need for time consuming parameter adjustments.

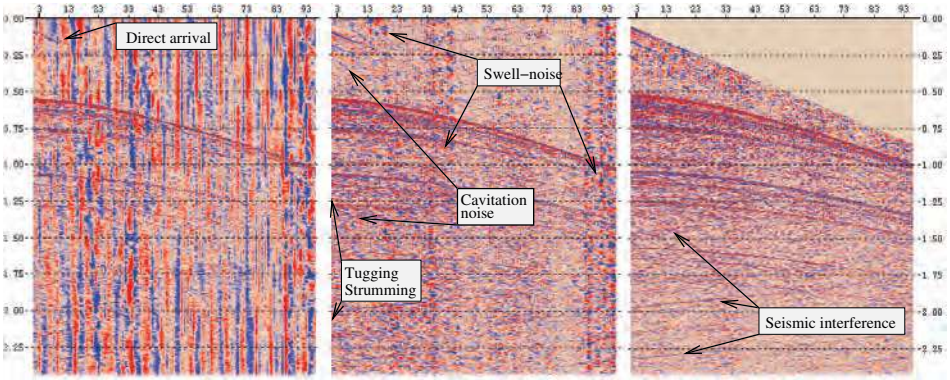

Figure 8.1: 96 trace, 2.5 s shot gather. Left: A raw shot. Middle: The same shot after the application of a low-cut filter. Right: The shot gather after the application of time-frequency de-noising to attenuate swell noise, strumming noise and cavitation noise. In the right image some noise in the water column has been muted away

In this paper we will look at a number of different noise types from a recent marine seismic survey acquired offshore Norway. The left image in Figure 8.1 shows a typical shot gather from this survey. In this gather the following types of noise were identified:

- Hydrostatic pressure variation noise (0-1(2) Hz)
- Swell noise (1-10(15) Hz)
- Tugging/strumming noise from the vessel (3-10 Hz)
- Propeller cavitation noise from the vessel (broad banded)
- Seismic interference (SI) noise (broad banded)

In the following sections we will explain the physical origin of these noise types. Furthermore we will show how most of this noise can be removed or attenuated, with special emphasis on SI removal and time-frequency de-noising.

8.2 Hydrostatic pressure noise

Hydrostatic pressure variations relates directly to the height of the water column over the seismic streamer. Such variations are caused by ocean swells and by streamer buckling.
The vertical movement $w(x, z, t)$ due to surface waves of a particle, in deep water, at depth z in deep water is approximately given by Kundu (1977) as

$$w(x, z) = A\omega e^{-kz} \sin(kx - \omega t). \tag{8.1}$$

Here A denotes the amplitude of the surface waves, with positive z pointing downwards. The wave-number is $k = 2\pi/\lambda$, where λ is the wave-length, and $\omega = \sqrt{gk}$ is the angular frequency, where g denotes gravity. Typical ocean swells have λ around 50-$100\,\mathrm{m}$ and frequencies well below $1\,\mathrm{Hz}$. Such waves cause very large amplitude, low frequency noise on seismic data, as can be observed in the left image in Figure 8.1. In Parrish (2005) it is shown that streamer buckling also can induce low frequencies (≤ 0.1 Hz), large amplitude pressure variation noise. Thankfully, the frequency content of hydrostatic pressure variations is limited to 0-$1(2)\,\mathrm{Hz}$. This frequency band does normally not contain much useful seismic data, and can therefore be removed with a low-cut filter. The second image in Figure 8.1 shows the result of applying a low-cut filter to the input data.

8.3 Swell-noise

The second problem in this data-set is swell-noise, as seen in the middle image in Figure 8.1. Swell-noise is high amplitude noise that normally contains frequencies from 2-$10(15)\,\mathrm{Hz}$. It usually affects a number of neighboring traces, and can be observed in seismic data as vertical stripes or 'blobs'. There are two different mechanisms that create swell-noise. On fluid filled streamers the streamer motion can induce transversal waves (so-called bulge wave), described by Peacock et al. (1983), Bjelland (1993), and Dowling (1998). Bulge waves are known to generate high-amplitude noise up to around $10\,\mathrm{Hz}$. Modern foam filled streamers are less troubled by such bulge waves. However, there is also a second swell-noise producing mechanism. From Eq 8.1 it is apparent that waves can induce a cross flow over the streamer. Cross flow can also be induced by ocean currents. Experiments by Bull and Dekkers (1993), Heenan and Morrison (2002a,b) and Snarski (2004) indicate that the flow characteristics in the turbulent boundary layer surrounding long cylindrical objects like seismic streamers will change when the local angle between the streamer and the flow direction exceeds 6-$15°$. Instead of having a symmetrical turbulent boundary layer, an increased angle will result in an unsymmetrical boundary layer where vortex shedding can take place. Vortex shedding is an unsteady flow where vortices are created and detached with a period that depends on the local flow conditions. This creates strong alternating pressure fluctuations that will be observed as high-amplitude swell-noise.
Figure 8.2 is a snapshot of a seismic cable in the ocean, where an environmentally friendly colored dye is released to visualize the boundary layer. From this picture the turbulent nature of the flow can clearly be observed.

8.3.1 Removing the swell-noise

Swell-noise can not be removed by a band-pass filter without also removing large parts of the seismic reflection signal. Instead, we have found that time-frequency filtering, see Elboth et al. (2008) and Bekara et al. (2008), is a well suited algorithm. It works by computing a spectral estimate of all traces within a sliding window. Amplitude estimates at each frequency are then compared with the amplitude estimate of a presumed good trace within the chosen window. If the amplitude difference is larger, the amplitude in question is attenuated to the level of the presumed good trace. This process is repeated for all frequencies specified by the user. The modified spectrum is finally transformed back to the time domain for each sliding window. In

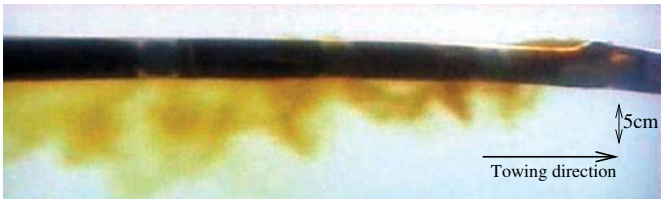

Figure 8.2: Snapshot of the turbulent boundary layer surrounding a seismic streamer array in the ocean. A dye is released to reveal structures in the turbulent boundary layer. The diameter of the cable in the image is $5\,\mathrm{cm}$.

this way, we do not simply remove the parts of the frequency spectrum that are affected by high amplitude noise. We also try to predict what the actual amplitude of the affected frequency should have been, based upon a spectral estimate of a presumed good trace in its neighborhood. Now, to get optimal results from time-frequency de-noising, it is important that the size of the chosen window is not made too large. Unfortunately, as observed in Figure 8.1, swell-noise tend to affect a number of neighboring traces. This problem can be solved by sorting the data into the CDP and/or common offset domain before applying the de-noising. In this way the large 'blobs' of swell-noise are broken up, and good estimates of data signal can be obtained. The results of applying this procedure to a data-set can be observed in the right image in Figure 8.1.

8.4 Tugging/strumming noise

Tugging noise is caused by sudden movements of the vessel due to wave motion. In addition to tugging, vibrations or strumming from the lead-in cables also affect some seismic gathers. These types of noise are most visible on the first sections on a streamer. Visually, small amounts of strumming noise can be observed in the middle image in Figure 8.1. This kind of noise is characterized by relatively large amplitudes in a narrow frequency band. It was therefore efficiently removed by the same time-frequency de-noising algorithm that we applied to remove the swell-noise.

8.5 Propeller cavitation noise

As a propeller move through a fluid, low pressure areas are formed as the fluid accelerates around and moves past the blades. If these low pressure areas reach vapor pressure, the fluid vaporizes and forms small bubbles. The collapse of these bubbles cause strong local 'shock-waves' (cavitation) that are seen as noise in seismic data, see Brennen (2005). Cavitation normally occurs when a propeller operates outside its design window. In some gathers in this survey cavitation noise could be observed. However, most of the time it was obscured by other types of noise. Because cavitation noise originates from the vessel propeller, the noise follows almost the same move-out curve as the ocean bottom. Cavitation noise is normally broad banded, and somewhat intermittent, see Elboth et al. (2009a). To remove the cavitation noise we adapted the time-frequency de-noising already used for swell-noise removal. The only difference was

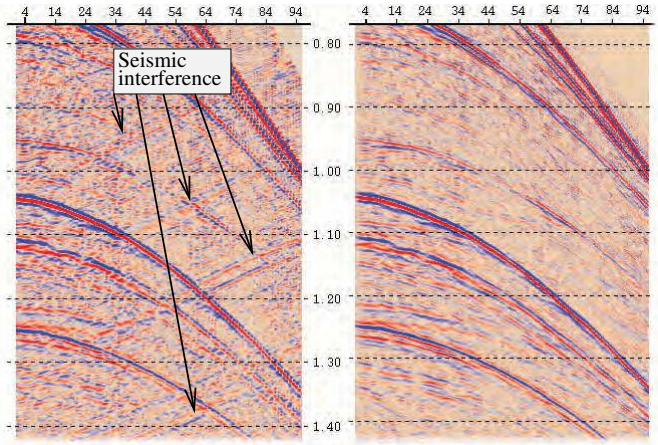

Figure 8.3: Part of shot gather before and after SI removal. Notice how the SI (the stripes going from lower left to upper right in the left image) has been attenuated in the right image. (This data is a zoom taken from the right image in Figure 8.1.)

that instead of only attacking swell-noise in the 0-10 Hz range, we applied the de-noising all the way up to the Nyquist frequency.

8.6 Seismic interference

The last type of noise observed in the data from this survey was seismic interference (SI) from another vessel operating in the same area. In the left image in Figure 8.3 SI noise can be observed as stripes. SI is broad banded, and can often have large amplitudes compared to subsurface reflection data.

A common approach for removing SI is to take advantage of the different move-out behavior(dip and/or curvature) of SI compared to the reflection data. When transformed to the Radon or τ-p domain, SI will often map into an area that can be muted.

The problem in this data was that the move-out of the SI was very close to the move-out of the seismic signal. Traditional muting was therefore not possible. Another approach used for SI attenuation is variants of f-x prediction filtering. In Gulunay et al. (2004) and Gulunay (2008) a number of such algorithms are discussed. The general idea is to attack SI by sorting it into a domain where it is random, compared to the reflection signal. In this new domain f-x prediction filtering is applied to suppress the SI, before the data is sorted back.

This approach could also work for our data. However, the geology in the area where the data was acquired contains a number of dipping features. Such features are unfortunately also easily removed by prediction filters. It was therefore decided to try out another SI-removal approach. The left image in Figure 8.4 shows the shot gather from the right image in Figure 8.1 transformed into the τ-p domain. The 'blobby' area that stands out is caused by SI.

The seismic vessel causing the SI has a shot point interval of around 10 s, while the data presented here was acquired with a shot interval of 4 s. When sorting τ-p gathers to the 'common'

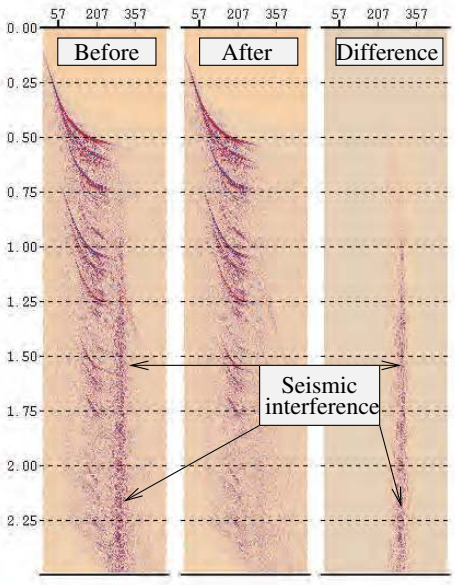

Figure 8.4: From left to right: Before, after and difference τ-p shots from de-noising. Notice the vertical noise train caused by SI. It is removed by the de-noising. (This is again data from the same shot gather as the right image in Figure 8.1.)

slowness domain, less than half of the traces were affected by SI.

The left image in Figure 8.5 shows part of a typical slowness gather from this line. Notice that the traces that come from τ-p gathers affected by SI stand out. The challenge now is what to do with the noisy traces. The approach chosen here was to apply time-frequency de-noising to the data in this slowness domain. This effectively attenuated the amplitudes of 'noisy' traces down to the level of the traces unaffected by SI. The middle image in Figure 8.5 shows the result of this, while the right image is the difference plot. Notice that unlike prediction filtering, time-frequency de-noising is amplitude preserving. It does not affect the traces that are assumed to be good.

8.7 Results

The results of the time-frequency SI removal approach on a shot gather can be seen in the right image in Figure 8.3. Notice how the SI has been attenuated in this image compared to the original data.

The final test of our SI de-noising is to compare stacked data, after de-multiple and migration. Figure 8.6 shows two versions of a final stack from the processing. The left image shows the data after de-noising, but excluding the new SI-removal approach. The middle image show the same data, where the new SI-removal approach was applied, while the right image shows the difference. It is clear that the SI-removal has attenuated lots of energy that otherwise was

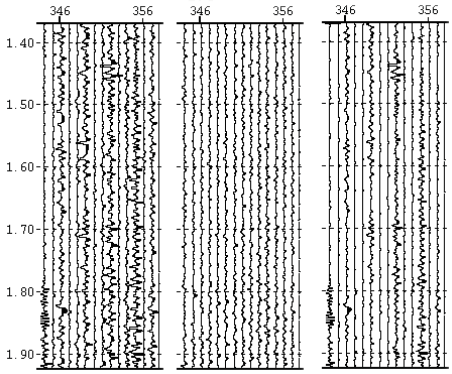

Figure 8.5: Part of a typical slowness gather from the data-set we have processed. From left to right: Before, After and Difference plot of time-frequency de-noising applied to the gather. Notice that only traces affected by SI are attenuated.

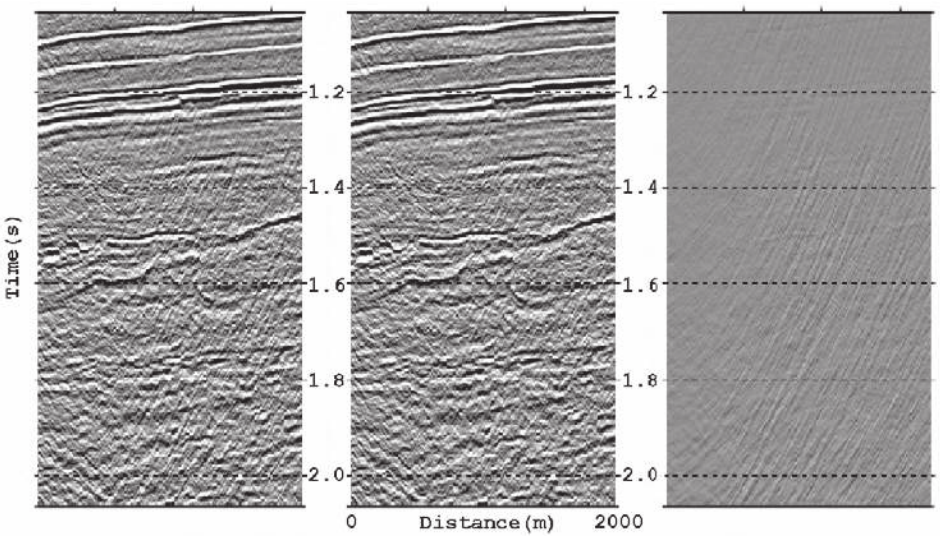

Figure 8.6: Part of stack between 1 and 2 s after de-multiple and migration. Left: After de-noising (excluding SI-removal). Middle: After de-noising (including SI-removal). Right: Difference plot. Note that all de-noising was applied pre-stack.

smeared out by the migration, and appears as strongly dipping events all over the data. We observe that SI de-noising significantly improved the quality of the data.

8.8 Conclusion

De-noising of seismic data is important to obtain good quality seismic sections. In this article we have outlined how time-frequency de-noising can be applied to attenuate many of the most common types of noise found in marine seismic. The general idea is to transform each type of noise into a domain where it somehow stands out, and then to attenuate it. A good physical understanding of how the noise is created helps us in choosing suitable domains for the attenuation, and provides a guide for the choice of de-noising parameters.
We have also introduced a new approach to attenuate SI, based upon these same ideas. Through the use of production data from a recent North Sea site-survey, we show the potential of this new method. SI attenuation on slowness gathers using time-frequency de-noising is especially suited when the move-out of the SI (linear noise) is close to that of the actual data. This is also a case where other de-noising algorithms often have problems.

Chapter 9 is removed

Chapter 10

Summary

This chapter sums up the main results of the research presented in this thesis. The summary is supplemented by estimates of the economical implications these results, and a final section that points towards some ongoing and future initiatives that are following up the work presented.

10.1 Contributions of this thesis

Loosely based upon the chapters in this thesis, the main contributions can be summed up as:

- Detailed physical and statistical descriptions of flow and swell noise on towed hydrophone arrays, obtained both from measurements and simulations. (Chapters 3, 4 and 5.)
- De-noising software and methodology to attenuate various types of noise found in seismic data. (Chapters 6, 7 and 8.)
- A proof of concept, based upon both simulations and practical measurements that super-hydrophobic surface coatings can be used to reduce both drag and flow-noise on seismic streamer arrays. (Chapter 9.)

10.1.1 Theory and measurements

Academically, the work describing and measuring flow and flow noise on a long streamer (cylinder) contributes to a field that started in the early stages of the cold war when the military needed to detect and track submarines. To do this the they started to tow hydrophone arrays, which inevitable were troubled by noise. This sparked research into topics of pressure fluctuations in turbulent boundary layers, with the aim of improving the performance of the sensor arrays. Within the seismic exploration industry similar hydrophone arrays called streamers, are used to study the subsurface geology. Seismic streamer data are normally also degraded by flow noise. Most previous works done to measure and describe such flow and flow noise is based on laboratory measurements of perfectly symmetric flows. In this thesis is that we have made measurements of flow and flow noise on streamers, towed at around $5\,\mathrm{kn}$, in the (unsteady) ocean. Based upon these measurements we present three results:

1. We show that it is the unsteadiness found in real life flows that are the reason for much of the low frequency flow and swell noise recorded on hydrophones inside axially aligned

cylinders (towed streamers). Excessive levels of flow (swell)-noise is produced when the angle between the streamer cable and the flow direction exceeds 5 to 10^0. This often happens when wave heights grow beyond 2 to $3\,\mathrm{m}$ or currents act on the streamer cables.

2. From measurements on a purpose built single sensor hydrophone array we computed the 'correlation length' of flow noise. Based on this computation we argue that an optimal hydrophone separation for seismic exploration is around $0.5\,\mathrm{m}$. This separation differs from standard practice in the industry today, and by placing hydrophones more densely, it should therefore be possible to improve the signal-to-noise ratio of data collected on hydrophone streamers.

3. Traditional wisdom says that to avoid flow noise, sensors (hydrophones) should be placed as fare away from the cable surface (where the flow noise is produced) as possible. Based upon our simulation of flow noise propagation inside a cylinder, it seems like the flow noise level is independent of sensor position. This was a somewhat surprising result, but it is also valuable in that it removes a number of limitations on how a future streamer needs to be designed.

Based upon our measurements and statistical analysis of the flow and swell noise, we have proceeded in two different directions, as explained below:

10.1.2 Software de-noising

As part of the work done in this thesis I have developed, implemented and maintained a software de-noising tool called TFDN, (time-frequency de-noise). The making of this module required quite a bit of computer science work, in order to transform academic ideas into a product suitable for commercial usage. The module works by employing a sliding window on a data gather. Within this window the data is compared statistically in order to identify abnormal (noisy) frequencies that needs to be attenuated. TFDN was initially developed to help attenuate swell noise from marine seismic data. This is also its primary usage. However, it has also successfully been applied to remove various other types of noise found in seismic data. These new noise attenuation methods often involves sorting or transforming the data to randomize the noise before the actual de-noising is performed. In most cases this means sorting shot gathers to the CDP or the common offset domain to make the noise random. Nevertheless, sometimes more drastic measures are needed. A processing sequence that involved sorting data in the radon and/or τ-p domains was introduced in chapters 6 and 8. Another approach, see was exemplified in Chapter 2 where traces are randomized within a given gather to break up the noise.
Due to its ease of usage, flexibility and efficiency, TFDN (de-noising) has become a standard commercial processing step withinthe geoscience company Fugro.

10.1.3 Superhydrophobic surface coatings

The last important academic contribution presented in this thesis is the use of superhydrophobic surface (SHS) coatings to reduce drag and flow-noise on seismic streamer cables. SHS are created by combining surface roughness with chemical hydrophobicity, and can on a macroscopic

scale support slip as water flows over a surface. In practice, SHS are in the form of a coating (paint) that is applied to a surface. The novel thing here is that we are the first to observe that a SHS coat reduces flow noise. This has been shown both through practical measurements, and through computer simulations.

10.2 Economic potential

It is fairly difficult to provide accurate estimates of the economical implications of the work done in this thesis. Never the less, the subsections below contain some rough calculations intended to illustrate the value of proper seismic data de-noising.

10.2.1 Economics of software de-noising

Software de-noising is valuable since is removes unwanted noise. However, it is also a prerequisite for later processing steps, like multiple removal and migration that require fairly noise free input to work optimally. The main effect of de-noising is therefore that it improves the quality of the seismic data. It is difficult to put a value on this directly. Nevertheless, commercially, it is always preferable to deliver a good, rather than a suboptimal product.

Contracts between oil-companies and seismic contractors typically state that if the average rms noise level on a line, after applying a certain low-cut filter, exceed 15 or $20\,\mu Bar$, this line will have to be re-acquired. This involves turning a vessel around, and placing it at the start of the line, before the acquisition can be redone. A single line in a 3-D survey can typically have a length of $50\,\mathrm{km}$, while a seismic vessel normally move at 4 to $5\,\mathrm{kn}$. The total time-expenditure for re-shooting such a line, including the time it takes to turn a vessel around, will therefore typically be about 12 hours. At present rates this correspond to an expenditure of about $US\$\,100\,\mathrm{K}$. Based upon de-noising examples shown in this thesis, it is reasonable to assume that proper de-noising can 'save' one marginal line pr 1-2 month pr vessel. For one seismic vessel, this corresponds to somewhere between $US\$\,0.5\,\mathrm{to}\,1\,\mathrm{M}$ pr year.
(Actually, this is not just a future potential, but is very much the way many of the seismic vessels already are operating.)

10.2.2 Economics of superhydrophobic surface coatings

The measurements we did on the effects of a superhydrophobic surface (SHS) showed a 5% decrease in drag on seismic streamer cables. Simulation and results reported in the literature indicate that it should be possible to achieve even better results. Nevertheless, lets assume that we by coating both the vessel, and all the seismic equipment are able to reduce the overall drag on a seismic vessel by 5%. Let's also assume that we do not increase the vessel speed, but rather take advantage of the drag reduction to achieve fuel savings. Again, very conservatively, lets assume we achieve a 5% decrease in fuel consumption. At 75 US$ pr barrel, the monthly fuel bill for a modern seismic vessel, towing 10-16 streamers, is around $US\$800\,\mathrm{K}$. Reducing this by 5% would therefore correspond to $US\$\,40\,\mathrm{K}$, or roughly $US\$\,500\,\mathrm{K}$ pr year.
In addition to this cost saving, a SHS will also improve the quality of the recorded data (less

flow/swell noise). It is difficult to put an exact value on this, but lets assume that SHS reduces the noise level in such a way that a vessel spends one day less on standby every 6 month. Based upon current vessel rates, this would correspond to an additional saving of around $US\$\,500\,\mathrm{K}$ pr year.

This quick computation does not stop at seismic vessels. Actually, there is no particular reason why not all marine vessels could be equipped with a similar SHS coating to reduce drag. The combined economical benefits for all ship operations would then be enormous.
Unfortunately, some caution is needed. As we showed in chapter 9, a problem was that the SHS we used was washed of after some time in the water. There are also significant costs associated with the actual coating process. The future challenge lies in developing low cost SHS coats that somehow are integrated with long lasting vessel paints.

10.3 Ongoing and future work

As a result of the research work done over the last 3-4 years several projects have emerged. The two first of these are mainly academic, while the others are more practically oriented, but with a significant industrial potential.

- An ongoing project is to extend the simulation work on flow noise around streamers. Presently we are working on increasing the Reynolds number of the simulations. Currently we are running simulations where we study how flow noise depend on cable diameter, curvature, and how cross flow affect the nature of the flow noise. Similar goals are also part of an European Defense Agency initiative that we participate in.

- In the signal processing field we continuously work on the time-frequency de-noise (TFDN) module for noise removal from seismic data. The aim is to extend the functionality in this module by coming up with new statistical methods to discriminate between signal and noise. Some ideas is to use correlations between traces or to employ the concept of mutual information.

- In cooperation with several partners we are actively developing and testing new coating materials for seismic streamers, and other in-water equipment. The aim if this is to come up with coats that in addition to reducing drag and flow noise, also have an anti-fouling effect. That is, they should prevent barnacle growth on streamers. This is a ambitious goal which require coating materials to be long lasting. Some of our initial tests have nevertheless been encouraging, and we plan to preform full scale testing (10 stramer cables of 6 km each) by Aug or Sept 2010.

- One of the seismic streamer manufacturer have take interest in the work on determining the correlation distance of flow noise. The aim is to improve the S/N ratio of seismic recordings by having sensors placed more densely within a streamer. During the summer 2010 we plan a first field test of this new generation of seismic streamer.

- New, small and emerging electro-optical and/or micro-electro-mechanical systems (MEMS) sensors might also offer possibilities with regard to future array systems. Different sensor

types might have different sensitivity to various types of noise. Signal processing can exploit this to improve the SNR. In addition, a MEMS vector sensor would solve the left-right ambiguity troubling hydrophone systems today. This means that theoretically, it should be possible to get a 3-D image (a cone) of the subsurface, by employing only one cable. This is more of a long term goal, which currently does not have any founding.

Bibliography

Abma, R., Jilek, P., Rothe, S., and Mika, J. (2007). Seismic interference noise removal, interpolation and regularization. *EAGE Technical Program Expanded Abstracts*, 69(B026).

Afzal, N. and Narasimha, R. (1976). Axisymmetric turbulent boundary layers along a circular cylinder at constant pressure. *Journal of Fluid Mechanics*, 74:113–128.

Anderson, R. G. and McMechan, G. A. (1989). Automatic editing of noisy seismic data. *Geophysical Prospecting*, 37(8):875–892.

Arguillat, B., Ricot, D., Robert, G., and Bailly, C. (2005). Measurements of the wavenumber-frequency spectrum of wall pressure fluctuations under turbulent flows. *11th Aeroacoustic Conf.. 23-25 may 2005. Monterey, CA*, 2005-2855.

Atta, C. (1968). Experiments on vortex shedding from yawed circular cylinders. *AIAA*, 6(5):931–933.

Barre, S., Bogey, C., and Bailly, C. (2006). Computation of the noise radiated by jets with laminae/turbulent nozzle-exit conditions. *27th AIAA Aeroacoustic Conference*, 2006-2443.

Barthlott, W. and Ehler, N. (1977). Raster-Elektronenmikroskopie der Epidermis-Oberflächen von Spermatophyten. *Tropische und subtropische Pflanzenwelt (Akad. Wiss. Lit. Mainz)*, 19:110.

Bechert, D. W., Bruse, M., Hage, W., van der Hoeven, J. G. T., and Hoppe, G. (1997). Experiments on drag-reducing surfaces and their optimization with an adjustable geometry. *Journal of Fluid Mechanics*, 338:59–87.

Bekara, M., Ferreira, A., and van der Baan, M. (2008). A statistical technique for high amplitude noise detection: Application to swell noise attenuation. *SEG Technical Program Expanded Abstracts*, 27(1).

Berenger, J.-P. (1994). A perfectly matched layer for the absorption of electromagnetic waves. *J. Comput. Phys.*, 114(1):185–200.

Bjelland, C. (1993). *Reduction of noise in seismic hydrophone arrays modeling of breathing waves and adaptive noise canceling*. PhD thesis, University of Bergen, Norway.

Bogey, C. and Bailly, C. (2007). An analysis of the correlations between the turbulent flow and the sound pressure fields of subsonic jets. *Journal of Fluid Mechanics*, 583:71–97.

Bogey, C., Barre, S., and Bailly, C. (2007). Direct computation of the noise generated by a hot coaxial jet. *28th AIAA Aeroacoustic Conference*, 2007-3387.

Bokde, A. L., Lueptow, R. M., and Abrahm, B. (1999). Spanwise structure of wall pressure on a cylinder in axial flow. *Physics of Fluids*, 11(1):151.

Brennen, C. E. (2005). *Fundamentals of multiphase Flow*. Cambridge University Press.

Brink, M. and Spackman, J. (2004). Solid streamers and single hydrophones. *SEG Technical Program Expanded Abstracts*, 23(1):41–44.

Bull, M. K. (1996). Wall-pressure fluctuations beneath turbulent boundary layers: Some reflections on forty years of research. *Journal of Sound and Vibration*, 2:299–315.

Bull, M. K. and Dekkers, W. (1993). Vortex shedding from long slender cylinders in near-axial flow. *Physics of Fluids*, 5:3296–3298.

Canales, L. L. (1984). Random noise reduction. *SEG Technical Program Expanded Abstracts*, 3(1):525–527.

Chang, P. A. (1998). *Relationship between turbulent wall pressure and velocity field sources*. PhD thesis, University of Maryland, USA.

Cipolla, K. M. and Keith, W. L. (2003). High Reynolds number tick axisymmetric turbulent boundary layer measurements. *Experiments in Fluids*, 35:477–485.

Cipolla, K. M. and Keith, W. L. (2008). Measurements of the wall pressure spectra on a full-scale experimental towed array. *Ocean Engineering*, 35:1052–1059.

Daniello, R. J., Waterhouse, N. E., and Rothstein, J. P. (2009). Drag reduction in turbulent flows over superhydrophobic surfaces. *Physics of Fluids*, 21(8):085103.

Deighan, A. J. and Watts, D. R. (1997). Ground-roll suppression using the wavelet transform. *Geophysics*, 62(6):1896–1903.

Denli, N. and Landweber, L. (1979). Thick axisymmetrical turbulent boundary layer on a circular cylinder. *AIAA*, 13(3):92–104.

Dowle, R. (2006). Solid streamer noise reduction principles. *SEG Technical Program Expanded Abstracts*, 25(1):85–89.

Dowling, A. (1998). Underwater flow noise. *Theoretical and Computational Fluid Dynamics*, 10(1-4):135–153.

Elbing, B. R., Winkel, E. S., Lay, K. A., Ceccio, S. L., Dowling, D. R., and Perlin, M. (2008). Bubble-induced skin-friction drag reduction and the abrupt transition to air-layer drag reduction. *Journal of Fluid Mechanics*, 612:201–236.

Elboth, T., Hermansen, D., and Andreassen, Ø. (2009a). Some unusual types of noise. *EAGE Technical Program Expanded Abstracts*, 71:5658.

Elboth, T. and Herrmansen, D. (2009). Attenuation of nooise in marine seismic data. *SEG Technical Program Expanded Abstracts*, 28(1):3312–3316.

Elboth, T., Lilja, D., Reif, B.A., and Andreassen, Ø. (2010a). Investigation of flow and flow noise around a seismic streamer cable. *Geophysics*, 75(1):Q1–Q9.

Elboth, T., Presterud, I., and Hermansen, D. (2010b). Time-frequency seismic data de-noising. *Geophysical Prospecting*, 58(3):441–453.

Elboth, T., Qaisrani, H., and Hertweck, T. (2008). De-noising seismic data in the time-frequency domain. *SEG Technical Program Expanded Abstracts*, 27(1):2622–2626.

Elboth, T., Reif, B., and Andreassen, Ø. (2009b). Flow and swell noise in marine seismic. *Geophysics*, 74(2):Q17–Q25.

Elboth, T., Reif, B., and Andreassen, Ø. (2010c). Hydrodynamic Flow Noise Reduction from Superhydrophobic Surfaces. *Acoustical Society of America Journal*, 1:submitted.

Elboth, T., Wasberg, C. E., Helgeland, A., Andreassen, Ø., and Reif, B. A. P. (2009c). Flow noise simulations around a cylinder. In *Fifth national conference on Computational Mechanics (MekIT'09)*.

Ffowcs Williams, J. E. and Hawkings, D. L. (1969). Sound generated by turbulence and surfaces in arbitrary motion. *Philosophical Transactions of the Royal Society*, 264(A):321–342.

Freund, J. B., Bodony, D. J., and Lele, S. K. (2002). Turbulence interactions leading to far-field jet noise. In *Proceedings of the Summer Program 2002*, pages 15–25. Center for Turbulence Research.

Frohnapfel, B., Lammers, P., Jovanović, J., and Durst, F. (2007). Interpretation of the mechanism associated with turbulent drag reduction in terms of anisotropy invariants. *Journal of Fluid Mechanics*, 577:457–466.

Fulton, T. (1985). Some interesting seismic noise. *The Leading Edge*, 4:70–75.

Furey, D. A. (2005). *The turbulent boundary layer on small diameter flexible cylinder on the wake of a streamlined towing apparatus*. PhD thesis, University of Maryland.

Gaarder, T. and Helgeland, A. (2002). VoluViz 1.0 Report. Technical Report FFI/RAPPORT-2002/03449, FFI (Norwegian Defence Research Establishment).

Gogte, S., Vorobieff, P., Truesdell, R., li, A. M., van Swol, F., Shah, P., and Brinker, C. J. (2005). Effective slip on textured superhydrophobic surfaces. *Physics of Fluids*, 17(5):051701.

Greene, Jr., C. R. and Richardson, W. J. (1988). Characteristics of marine seismic survey sounds in the Beaufort Sea. *Acoustical Society of America Journal*, 83:2246–2254.

Gulunay (1986). Fxdecon and complex wiener prediction filter. In *In Proceedings of 56th Annual Internat. Mtg., Soc. Exp. Geophys.*, pages 279–281.

Gulunay, N. (2008). Two different algorithms for seismic interference noise attenuation. *The Leading Edge*, 27(2):176–181.

Gulunay, N., Magesan, M., and Baldock, S. (2004). Seismic interference noise attenuation. *SEG Technical Program Expanded Abstracts*, 74.

Haddle, G. P. (1969). The Physics of Flow Noise. *Acoustical Society of America Journal*, 46:130–+.

Hahn, S., Je, J., and Choi, H. (2002). Direct numerical simulation of turbulent channel flow with permeable walls. *Journal of Fluid Mechanics*, 450:259–285.

Hasselblad, V. (1969). Estimation of finite mixtures of distributions from the exponential family. *Journal of the American Statistical Association*, pages 1459–1471.

Heenan, A. F. and Morrison, J. F. (2002a). Turbulent boundary layers on axially-inclined cylinders. I. Surface-pressure/velocity correlations. *Experiments in Fluids*, 32:547–557.

Heenan, A. F. and Morrison, J. F. (2002b). Turbulent boundary layers on axially-inclined cylinders. II. Circumferentially averaged wall-pressure wavenumber-frequency spectra. *Experiments in Fluids*, 32:616–623.

Henoch, C., Krupenkin, T. N., Kolodner, P., Taylor, J. A., Hodes, M. S., and Lyons, A. M. (2006). Turbulent drag reduction using superhydrophobic surfaces. *3rd AIAA Flow Control Conferance*, (AIAA paper 2006-3192).

Herkenhoff, E., Bones, F., Louiel, D., and Hu, K. B. (2004). (Patent wo/2004/104636) Method for signal-to-noise ration enhancement of seismic data using amplitude noise attenuation.

Herrmann, F. J. (2004). Curvelet imaging and processing: an overview. CSEG National Convention.

Hite, D., Fontana, P., and Haugland, T. (2003). Towed streamer data bandwidth — a ghost story. *SEG Technical Program Expanded Abstracts*, 22(1):1–3.

Hu, F. Q. (2005). A perfectly matched layer absorbing boundary condition for linearized euler equations with a non-uniform mean flow. *J. Comput. Phys.*, 208(2):469–492.

Hu, Z., Morfey, C. L., and Sandham, N. D. (2003). Sound radiation in turbulent channel flows. *J. Fluid Mech*, 475(1):269–302.

Hu, Z., Morfey, C. L., and Sandham, N. D. (2006). Prediction of boundary layer sound radiation from wall shear stresses using dns data. In *12th AIAA/CEAS Aeroacoustic Conference (27th AIAA Aeroacoustic Conference)*. iaee.

Hutchins, N. and Marusic, I. (2007). Evidence of very large meandering features in the logarithmic region of turbulent boundary layers. *Journal of Fluid Mechanics*, 579:1–28.

Keith, W. L., Cipolla, K. M., and Furey, D. (2008). Turbulent wall pressure fluctuation measurements on a towed model at high Reynolds numbers. *Experiments in Fluids*, pages 119–+.

Keith, W. L., Cipolla, K. M., Hart, D. R., and Furey, D. A. (2005). Drag measurements on long thin cylinders at small angles and high Reynolds numbers. *Experiments in Fluids*, 38:759–769.

Kerman, B. R. (1984). Underwater sound generation by breaking wind waves. *Acoustical Society of America Journal*, 75:149–165.

Kjellgren, P. and Davidson, L. (2009). Large eddy simulations of turulent flow noise on streamers. *SEG Technical Program Expanded Abstracts*, 28(1).

Knight, A. (1996). Flow noise calculations for extended hydrophones in fluid- and solid-filled towed arrays. *Acoustical Society of America Journal*, 100:245–251.

Kundu, P. K. (1977). *Fluid Mechanics*. Academic Press.

Landau, L. D. and Lifshitz, E. M. (1987). *Fluid Mechanics 2ed., Course of Theoretical Physics vol. 6*. Butterworth-Heinemann.

Landrø, M. (2008). The effect of noise generated by previous shot on seismic reflection data. *Geophysics*, 73(3):Q9–Q17.

Lighthill, J. (1952). On sound generated aerodynamically. i. general theory. *Proc. R. Soc. Lond*, A(211):564–587.

Lighthill, J. (1954). On sound generated aerodynamically. ii. turbulence as a source of sound. *Proc. R. Soc. Lond*, A(222):1–32.

Lighthill, J. (1978). *Waves In Fluids*. Cambridge University Press.

Lueptow, R., Leehey, P., and Stellinger, T. (1985). The thick, turbulent boundary layer on a cylinder - mean and fluctuating velocities. *Physics of Fluids*, 28:3495–3505.

Lumley, J. L. (1978). Computational modelling of turbulent flow. *Adv. Appl. Mech.*, 18:123–176.

Lumley, J. L. and Newman, G. (1977). The return to isotropy of homogenious turbulence. *Journal of Fluid Mechanics*, 82:161–178.

Ma, M. and Hill, R. M. (2006). Superhydrophobic surfaces. *Current Opinion in Colloid & Interface Science*, 11(4):193–202.

Martell, M. B. (2009). Simulation of turbulence over superhydrophobic surfaces. Master's thesis, University of Massachusetts Amherst.

Martell, M. B., Perot, J. B., and Rothstein, J. P. (2009). Direct numerical simulations of turbulent flows over drag reducing ultrahydrophobic surfaces. *Journal of Fluid Mechanics*, 620(620):31–41.

McDonald, M. A., Hildebrand, J. A., Wiggins, S. M., and Ross, D. (2008). A 50 Year comparison of ambient ocean noise near San Clemente Island: A bathymetrically complex coastal region off Southern Califirnia. *Acoustical Society of America Journal*, 124:1985–1992.

Miao, X. and Cheadle, S. (1998). Noise attenuation with wavelet transforms. *SEG Technical Program Expanded Abstracts*, pages 1072–1075.

Monty, J. P., Stewart, J. A., Williams, R. C., and Chong, M. S. (2007). Large-scale features in turbulent pipe and channel flows. *Journal of Fluid Mechanics*, 589:147–156.

Neves, J. C. and Moin, P. (1994a). Effects of convex transverse curvature on wall-bounded turbulence. Part 1. The velocity and vorticity. *Journal of Fluid Mechanics*, 272:349–381.

Neves, J. C. and Moin, P. (1994b). Effects of convex transverse curvature on wall-bounded turbulence. Part 2. The pressure fluctuations. *Journal of Fluid Mechanics*, 272:383–406.

Nishi, R. Y. (1970). Measurement of Noise on an Underwater Towed Body. *Acoustical Society of America Journal*, 48:753–758.

Paidoussis, M. P. (1966). Dynamics of flexible slender cylinders in axial flow. Part 2. Experiments. *Journal of Fluid Mechanics*, 26:737–751.

Parrish, J. F. (2005). Streamer string waves and swell noise. *SEG Technical Program Expanded Abstracts*, 24(1):72–75.

Partyka, G., Gridley, J., and Lopez, J. (1999). Interpretational applications of spectral decomposition in reservoir characterization. *The Leading Edge*, 18(3):353–360.

Peacock, J. H., Sykes, C. G., Cameron, N. W., and Peardon, L. G. (1983). Advanced acoustic design for a new seismic streamer. *SEG Technical Program Expanded Abstracts*, 2(1):465–466.

Ramberg, S. (1983). The effects of yaw and finite length upon the vortex wakes of stationary and vibrating circular cylinders. *Journal of Fluid Mechanics*, 128:81–107.

Rothstein, J. (2010). Slip on superhydrophobic surfaces. *Annual Review of Fluid Mechanics*, 42:in press.

Sanders, W. C., Winkel, E. S., Dowlling, D. R., Perlin, M., and Ceccio, S. L. (2006). Bubble friction drag reduction in a high-reynolds-number flat-plate turbulent boundary layer. *Journal of Fluid Mechanics*, 552(-1):353–380.

Schlichting, H. (1979). *Boundary Layer Theory*. McGrawHill.

Schoenberger, M. and Mifsud, J. F. (1974). Hydrophone streamer noise. *Geophysics*, 39(6):781–793.

Schonewille, M., Vigner, A., and Ryder, A. (2008). Swell-noise attenuation using an iterative fx prediction filtering approach. *SEG Technical Program Expanded Abstracts*, 27(1):2646–2651.

Smith, J. G. (1999). Amplitude and phase effects of weather noise. *SEG Technical Program Expanded Abstracts*, 18(1):1485–1488.

Snarski, S. (1993). *Relation Between the Fluctuating Wall Pressure and the Turbulent Structure Of a Boundary Layer on a Cylinder In Axial Flow*. PhD thesis, Northwestern University.

Snarski, S. (2004). Flow over yawed circular cylinders: Wall pressure spectra and flow regimes. *Physics of Fluids*, 16:344–359.

Snarski, S. R. and Lueptow, R. M. (1995). Wall pressure and coherent structures in a turbulent boundary layer on a cylinder in axial flow. *Journal of Fluid Mechanics*, 286:137–171.

Solbakken, S. and Andersson, H. I. (2004). On the drag reduction mechanism in a lubricated turbulent channel flow. *International Journal of Heat and Fluid Flow*, 25(4):618 – 624.

Stein, J. A. and Langston, T. (2007). A review of some powerful noise elimination techniques for land processing. *EAGE Technical Program Expanded Abstracts*.

Taylor, G. I. (1938). The spectrum of turbulence. *Proc. R. Soc. Lond*, 164:100–114.

Thomson, D. (1982). Spectrum estimation and harmonic analysis. *Proceedings of the IEEE*, 70:1055–1096.

Thomson, K. D. and Morrison, D. F. (1971). The spacing, position and strength of vortices in the wake of slender cylindrical bodies at large incidence. *Journal of Fluid Mechanics*, 50:751–783.

Tutkun, M., George, W. K., Delville, J., Stanislas, M., Johansson, P. B. V., Foucaut, J. M., and Coudert, S. (2009). Two-point correlations in high reynolds number flat plate turbulent boundary layers. *Journal of Turbulence*, 10:N21+.

Tutty, O. (2008a). Flow along a long thin cylinder. *Journal of Fluid Mechanics*, 602:1–37.

Tutty, R. O. (2008b). Flow along a long thin cylinder. *Journal of Fluid Mechanics*, 602:1–37.

Ulrych, T. J., Sacchi, M. D., and Graul, J. M. (1999). Signal and noise separation: Art and science. *Geophysics*, 64(5):1648–1656.

Wang, Y. (1999). Random noise attenuation using forward-backward linear prediction. *Journal Of Seismic Exploration*, 8(2):133–143.

Wasberg, C., Gjesdal, T., Reif, B. P., and Andreassen, Ø.. (2009). Variational multiscale turbulence modeling in a high order spectral element method. *J. Comput. Phys.*, 228:7333–7356.

Watts, D. R., Deighan, A. J., and Riedel, C. (1999). Attenuation of marine wave swell noise by stacking in the wavelet packet domain. *SEG Technical Program Expanded Abstracts*, 18(1):1220–1223.

Wenz, G. M. (1962). Acoustic Ambient Noise in the Ocean: Spectra and Sources. *Acoustical Society of America Journal*, 34:1936–1950.

Willmarth, W. and Sharma, L. K. (1984). Study of turbulent structure with hot wires smaller than the viscous length. *Journal of Fluid Mechanics*, 142:121–149.

Willmarth, W., Winkel, R., Sharma, L., and Bogar, T. (2006). Axially symmetric turbulent boundary layers on cylinders: mean velocity profiles and wall pressure fluctuations. *Journal of Fluid Mechanics Digital Archive*, 76(01):35–64.

Willmarth, W., Winkel, R. E., Bogar, T., and Sharma, L. (1975). Axially symmetric turbulent boundary layers on cylinders: Mean velocity profiles and wall pressure fluctuations. *NASA STI/Recon Technical Report N*, 76:15426–+.

Willmarth, W., Winkel, R. E., Sharma, L., and Bogar, T. (1976). Axially symmetric turbulent boundary layers on cylinders: Mean velocity profiles and wall pressure fluctuations. *Journal of Fluid Mechanics*, 76:35–64.

Willmarth, W. and Yang, C. S. (1970). Wall-pressure fluctuations beneath turbulent boundary layers on a flat plate and a cylinder. *Journal of Fluid Mechanics*, 41:47–80.

Woods, M. (2006). *Computation of Axial and Near-Axial Flow Over a Long Circular Cylinder*. PhD thesis, University of Adelaide.

Woolford, B., Prince, J., Maynes, D., and Webb, B. W. (2009). Particle image velocimetry characterization of turbulent channel flow with rib patterned superhydrophobic walls. *Physics of Fluids*, 21(8):085106.

Woolford, B., Prince, J., Maynes, D., and Webb, B. W. (2009). Particle image velocimetry characterization of turbulent channel flow with rib patterned superhydrophobic walls. *Physics of Fluids*, 21(8):085106–+.

Yu, Z., Dellinger, J., Gutowski, P., and Garossino, P. (2004). Seismic resolution enhancement in the wavelet-transform domain. *SEG Technical Program Expanded Abstracts*, pages 1933–1936.

Öz Yilmaz (2001). *Seismic data analysis*. Society of Exploration Geophysicists.